N71-18872 to
N71-18875
NASA CR-116808

NATIONAL AERONAUTICS AND SPACE ADMINISTRATION

Space Programs Summary 37-66, Vol. I

Flight Projects

For the Period September 1 to October 31, 1970

JET PROPULSION LABORATORY
CALIFORNIA INSTITUTE OF TECHNOLOGY
PASADENA, CALIFORNIA

November 30, 1970

JET PROPULSION LABORATORY *California Institute of Technology • 4800 Oak Grove Drive, Pasadena, California 91103*

ANNOUNCEMENT

CANCELLATION OF THE SPACE PROGRAMS SUMMARY (SPS)

With the completion of the SPS 37-66 series, the Space Programs Summary (SPS) is cancelled as a periodical publication of the Jet Propulsion Laboratory. The SPS is being replaced by a new publication, the JPL Quarterly Technical Review (QTR).

The QTR will be comprised of brief technical articles describing selected JPL work and a bibliography of recent JPL publications.

Current external recipients of the SPS will automatically receive the new QTR.

Telephone 354-4321 *Twx 213-449-2451*

NATIONAL AERONAUTICS AND SPACE ADMINISTRATION

Space Programs Summary 37-66, Vol. I

Flight Projects

For the Period September 1 to October 31, 1970

JET PROPULSION LABORATORY
CALIFORNIA INSTITUTE OF TECHNOLOGY
PASADENA, CALIFORNIA

November 30, 1970

SPACE PROGRAMS SUMMARY 37-66, VOL. I

Prepared Under Contract No. NAS 7-100
National Aeronautics and Space Administration

Preface

The Space Programs Summary is a multivolume, bimonthly publication that presents a review of technical information resulting from current engineering and scientific work performed, or managed, by the Jet Propulsion Laboratory for the National Aeronautics and Space Administration. The Space Programs Summary is currently composed of four volumes:

Vol. I. *Flight Projects* (Unclassified)

Vol. II. *The Deep Space Network* (Unclassified)

Vol. III. *Supporting Research and Advanced Development* (Unclassified)

Vol. IV. *Flight Projects and Supporting Research and Advanced Development* (Confidential)

Contents

Contents (contd)

I. *Mariner* Mars 1971 Project

A. Project Description

The primary objective of the *Mariner* Mars 1971 Project is to place two spacecraft in orbit around Mars that will be used to perform scientific experiments directed toward achieving a better understanding of the physical characteristics of that planet. Principal among these experiments are measurements of atmospheric and surface parameters at various times and locations to determine the dynamic characteristics of the planet. Approximately 70% of the Martian surface will be observed during a minimum of 90 days of orbital operations.

During Mission A, it is planned to map the topography of a large portion of the Martian surface at a resolution significantly higher than that achievable with earth-based methods or by the *Mariner* Mars 1969 spacecraft. In addition, measurements will be made of the composition, density, pressure, and thermal properties of the planet's atmosphere. Other measurements will be directed toward an understanding of Mars' surface temperatures, composition, and thermal properties (particularly at the polar caps); its apparent lack of internal activity; its mass distribution; and its shape.

During Mission B, data will be sought on time-variable features of the Martian surface associated with the wave of darkening wherein both seasonal and secular changes occur. Also, information on atmospheric structure and gross dynamics will be obtained, as well as information directed toward an understanding of Mars' mass distribution, its shape, and its apparent lack of internal activity.

A capability will exist to redirect goals for either mission to the alternate mission if desired. The two launches are anticipated for May 1971, with arrival at the planet during the following November.

An engineering objective of the project is to demonstrate the ability of the spacecraft to perform orbital operations in an adaptive mode wherein information from one orbital pass is used to develop the operations plan for subsequent orbital passes. Studies indicate a high probability that at least one of the spacecraft will survive the sun occultation period which occurs shortly after the 90-day mission is completed. This makes it possible to conduct an Extended Mission for about a year after orbit insertion. The Extended Mission will probably consist of one or two data taking sequences per week with the capability of recording and playing back about a half-recorder of data (16 TV frames and 11 min of spectrometer data).

One of the *Mariner* Mars 1971 flight spacecraft will be new, and the other will be the spare flight spacecraft of the *Mariner* Mars 1969 Project modified to meet the requirements of the 1971 missions and to enhance mission reliability. The proof test model spacecraft of the *Mariner* Mars 1969 Project will be modified to become the proof test model for the *Mariner* Mars 1971 Project, to be used for preliminary testing and as a simulator in support of flight operations. A major modification for the *Mariner* Mars 1971 mission will be the addition of a rocket motor required to decelerate the spacecraft and place it in orbit around Mars.

Separate scientific instrument subsystems will be required to accomplish the television, infrared radiometer, ultraviolet spectrometer, and infrared spectrometer interferometer experiments given in Table 1. The S-band occultation and celestial mechanics experiments will require no additional equipment on the spacecraft.

Management responsibilities for the overall project, the Spacecraft System, the Mission Operations System, and the Tracking and Data System have been assigned to JPL.

Lewis Research Center has been assigned management responsibility for the Launch Vehicle System. The launch vehicle will be an *Atlas/Centaur* developed by General Dynamics/Convair.

The *Mariner* Mars 1971 missions will be supported by the Air Force Eastern Test Range launch facilities at Cape Kennedy, the tracking and data acquisition facilities of the Deep Space Network, and other NASA facilities.

Table 1. *Mariner* Mars 1971 scientific experiments and principal investigators

Television	
H. Masursky	Team leader
H. Masursky	PI/U.S. Geological Survey
R. Batson	CI/U.S. Geological Survey
W. Borgeson	
M. Carr	
J. F. McCauley	
D. Milton	
R. Wildey	
D. Wilhelms	
J. Lederberg	PI/Stanford University
E. Levinthal	CI/Stanford University
J. B. Pollack	CI/Cornell University
C. Sagan	CI/Cornell University
G. de Vaucouleurs	PI/University of Texas
W. B. Thompson	PI/Bellcomm
G. A. Briggs	CI/Bellcomm
P. L. Chandeysson	CI/Bellcomm
E. N. Shipley	CI/Bellcomm
B. Smith	PI/New Mexico State University
M. E. Davies	CI/Rand Corp.
W. K. Hartmann	CI/Arizona State University
N. H. Horowitz	CI/Caltech
R. B. Leighton	CI/Caltech
C. B. Leovy	CI/University of Washington
T. B. McCord	CI/MIT
B. C. Murray	CI/Caltech
R. P. Sharp	CI/Caltech

Ultraviolet spectrometer	
C. Barth	PI/University of Colorado
C. W. Hord	CI/University of Colorado
J. B. Pearce	CI/University of Colorado

Infrared interferometer spectrometer	
R. A. Hanel	PI/Goddard Space Flight Center
B. J. Conrath	CI/Goddard Space Flight Center
W. A. Hovis	CI/Goddard Space Flight Center
V. Kunde	CI/Goddard Space Flight Center
G. V. Levin	CI/Biospherics
P. D. Lowman	CI/Goddard Space Flight Center
C. Prabhakara	CI/Goddard Space Flight Center
B. Schlachman	CI/Goddard Space Flight Center

Infrared radiometer	
G. Neugebauer	PI/Caltech
S. C. Chase	CI/Santa Barbara Research Center
H. Kieffer	CI/UCLA
E. D. Miner	CI/JPL
G. Munch	CI/Caltech

Celestial mechanics	
J. Lorell	Team leader
J. Lorell	PI/JPL
J. D. Anderson	CI/JPL
W. L. Martin	CI/JPL
W. L. Sjogren	CI/JPL
I. Shapiro	PI/MIT
M. Ash	CI/MIT
W. Smith	CI/MIT

S-band occultation	
A. Kliore	PI/JPL
D. L. Cain	CI/JPL
G. Fjeldbo	CI/JPL
B. L. Seidel	CI/JPL

PI = Principal investigator, who is the proposer for each experiment.

CI = Co-investigator, who assists the proposer on each experiment.

Team leader heads a particular group of PIs and CIs on an experiment where there is more than one PI.

B. Mission and Test Computer System, *Computation and Analysis Section*

The mission and test computer (MTC) system completed the real-time system test support of the *Mariner* Mars 1971 proof-test model (PTM) spacecraft using a data system based on a single Univac 1219 computer. During this test phase the second 1219 computer was used for software development and driving video data to the mission and test video system (MTVS) to produce TV pictures. The MTC hardware system has now added a second data input subsystem, telemetry assemblers, and remote and local serial interface equipment for intercommunication with display equipment, in order to provide for the simultaneous testing of the two flight spacecraft. Dual test support, with a 1219 computer assigned to each spacecraft, began in late September 1970. By mid-October, sufficient programming development was completed to begin using the Univac 1230 MTC computer and the two Univac 1219 computers in the integrated three-computer system configuration described in SPS 37-63, Vol. I, p. 4. In this configuration the plan is for the 1230 computer to frame synchronize and decommutate all of the high-rate data streams (1–16.2 kbits/s telemetry and hardline data and 132.3 kbits/s hardline science data) and forward both the synchronized and the decommutated data to the 1219 computers for tape recording, processing, and formatting for display.

The 1230 computer decommutation programs are being developed in a sequence to provide a science instrument data-handling capability as early as possible in the flight spacecraft test program, since only a part of this data was processed during the PTM spacecraft tests. The development sequence is:

(1) Spectral science format (486 bits/frame) data decommutator.

(2) Infrared interferometer spectrometer (IRIS) science format (4725 9-bit words/frame) decommutator, for extracting IRIS interferogram data from the spectral science format as well as the recorded science format (7938 bits/frame).

(3) Ultraviolet spectrometer (UVS) science format (5400 bits/frame) decommutator, for extracting UVS instrument data from the spectral science format.

(4) UVS science format (4800 bits/frame) decommutator, for extracting UVS instrument data from the recorded science format.

(5) Video science format (972 bits/frame) decommutator.

(6) Recorded science format (7938 bits/frame) data decommutator.

(7) Orbital science format (420 bits/frame) embedded-data decommutators, for extracting the intermingled bits of the 420-bit frame from the recorded science, video science, and the spectral science data formats, simultaneously if necessary.

The 1219 computer real-time system used for PTM support provided only the recorded science decommutator capability listed above. The engineering format (140 bits frame) and orbital science format (real-time science 1) data will continue to be decommutated in real-time by the 1219 computers, as they were during PTM tests.

Magnetic tape records of all the above frame-synchronized and decommutated formats are recorded in real-time, as received from the two spacecraft. Additional records are made on this tape of the decommutated channels of engineering telemetry, orbital science data, spacecraft events and status, and central computer commands. The various intermingled records are later sorted selectively by type and re-recorded on separate types of tapes in order to save only the data required permanently. The IRIS and UVS instrument formatted records (2), (3), and (4), provide the data source for off-line processing, such as Fourier transformation of the IRIS interferogram data on the IBM 360/75 computers. The decommutated engineering and science data records provide the source for efficiently producing nonreal-time data channel tabulations and plots by the 1219 or 1218 computers without requiring decommutation, which is not available currently as a nonreal-time MTC system capability. About 400 channels of data are included in this record. Raw data records of three types are also recorded, primarily to aid in program debugging and data stream analysis. These records contain all low-rate data, all high-rate data, and the output of the data multiplexer in the attitude-control subsystem support equipment. With the exception of the recorded science format, when a data stream cannot be frame synchronized or decommutated because of erroneous PN code, wrong frame length, etc., the raw data is recorded with a suitable header identification, permitting unsynchronized data to be dumped for hand decommutation if necessary.

The 1219 computers accomplish a major portion of the general processing in the MTC system, including low-rate data stream decommutation and all tape recording functions, as well as the standard processing performed on each quantitative-measurement channel. All special processing routines required to assess spacecraft subsystem performance, extract and manipulate data, derive new data channels based on combinations of other channel data, etc., is also accomplished in the 1219s. The total processing requirements on the single 1219 computer used for PTM spacecraft test support required increasing its core memory size from 49k to 65k words by reducing the second 1219 computer to a 32k-word machine. The memory which will become available in the 65k-word 1219 computer by removal of the recorded science format (R7938) decommutator to the 1230 computer will be utilized to accommodate the program for cathode ray tube (CRT) system data display, the real-time plot processor, and additional requested special processors still under development.

The additional core memory modules required to increase the memory size of the second 1219 computer from 32k to 65k words have been obtained on loan from the USAF Space and Missile Systems Organization. This equipment was installed in late September, thus removing the limitations on dual-spacecraft test support capability and the operational inconvenience of supporting testing with different program configurations in the two 1219 computers.

Significant problems were encountered in the PTM test period in obtaining reliable frame synchronization and processing of the real-time 132.3 kbits/s high-rate science hardline data (input to the spacecraft data storage subsystem). These problems were caused mainly by deficiencies in the data interface between science support equipment and the MTC data input subsystem, which were removed by redesign, and by an intermittent failure of the interface between the data assembler and 1219 computer input channel. In addition, the programming system had to be restructured several times to eliminate saturation of the system during peak processing loads. The reliability of high-rate data processing is now satisfactory in the 1219 computer system. Checkout of the operation of decommutation programs 5, 6, and 7 in the previous list still remains to be accomplished in the 1230/1219 computer MTC system environment.

The full complement of 24 30-characters/sec printers required for displaying spacecraft subsystem and science instrument data on the two system test complexes is installed. Eight additional printers of this type (Univac DCT-500) were provided in the SFOF "mini-ops" area, a section of the future *Mariner* Mars 1971 operations area, in order to familiarize members of the spacecraft team with the format and content of the MTC-processed system test data. The 6-channel CRT display controllers (Computer Communications, Inc.) for each 1219 computer were received and are in acceptance. The leased Univac 432-drum memory system was received and is in checkout. A new motor-generator to provide 400-Hz power to the MTC system from the 60-Hz SFOF uninterrupted power system was installed to permit maintenance and repair of the second unit, following which it will become a backup power source until relocation of the prime unit at Air Force Eastern Test Range during prelaunch test. The option to purchase the Univac 1230 MTC computer was exercised at the start of FY 1971.

C. Calibration of the Scan Proof Test Model,

Spacecraft Control Section

1. Introduction

Calibration of the reference and telemetry/monitor potentiometers was performed on the scan electronics proof-test model (PTM). The calibration procedure used is new and has been developed for use on the *Mariner* Mars 1971. The reference potentiometers store the scan platform reference angles in such a way that the stored angle is proportional to the voltage on the reference potentiometer wiper. The telemetry/monitor potentiometer is mechanically coupled to the reference potentiometer and is used to monitor the position of the reference potentiometer and, hence, the stored reference angle. The stored angle may be varied in increments by stepping the reference potentiometer shaft by a drive mechanism. Calibration of the potentiometers was achieved by recording the potentiometer wiper positions as a function of a number of position increments.

2. Description of Angle Storage Subassembly

The scan subsystem contains four reference angle storage subassemblies. Each subassembly contains a stepper-motor/gear-train drive mechanism which drives a set of angle storage potentiometers. Two subassemblies with different step size are used for storing reference angles for each of the clock and cone axes as shown in Fig. 1.

In each axis one subassembly is arranged so that its stored angles can be varied in an increment of 0.25 deg (equivalent platform increment) for each command input pulse, and the other subassembly in an increment of 1 deg for each input pulse. The calibration ranges were from 90 to 305 deg in the clock axis and 90 to 170 deg in the cone axis. The fine resolution (0.25-deg increments) potentiometers were calibrated every 5 deg and the coarse resolution potentiometers (1 deg increments) every 20 deg.

3. Calibration Scheme and Results

The scan servo-control subsystem is designed to align the scan platform pointing direction with the reference angle stored in the angle storage subassembly. The pointing error generated within the subsystem is a sum of the errors contributed by the reference subassembly, the servo electronics, and the scan actuator. The error contributed by the reference subassembly is mainly caused by the uncertainty of the motor step-angle variation, gear backlash, and nonlinearity of the potentiometers. The servo electronics contributes errors due to finite gain and input offset. The actuator contributes errors due to the start voltage of the servo motor, gear stiction, and nonlinearity of the feedback potentiometer.

The calibration scheme illustrated in Fig. 2 provides information on the magnitude and characteristics of the errors contributed by the subassemblies to the subsystem pointing accuracy. Since the calibration of the potentiometers was performed without the actuator subassembly, a simulated feedback potentiometer (ratiometer 2) was inserted. The reference and telemetry/monitor potentiometers were calibrated by recording the potentiometer wiper positions in voltage ratio units as a function of a number of input pulses applied to the reference subassembly. The voltage ratio readings were obtained when the ratiometers 1 and 2 were adjusted for null on the meters M1 and M2.

The calibration of the reference subassembly revealed a typical gear backlash of about 0.02 deg (equivalent platform angle) or less. The error contributed by the motor step angle variation is non-cumulative and was

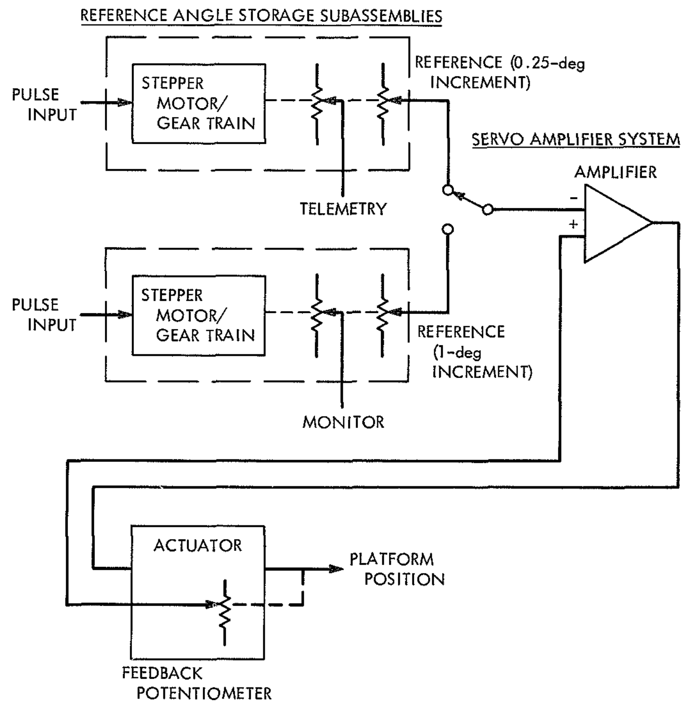

Fig. 1. Block diagram of one-axis scan subsystem showing angle storage subassemblies

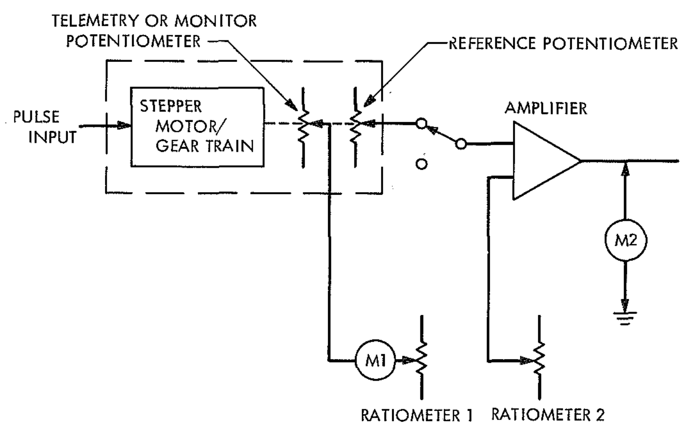

Fig. 2. Calibration scheme for one-angle store subassembly

about ±0.02 deg. The errors contributed from these sources were considered very small. The readout of the ratiometer 2 enables one to correlate the number of command input pulses to the output shaft angle of the actuator. The actuator was calibrated separately for the feedback potentiometer outputs (unloaded) as a function of the shaft angle. Since the ratiometer 2 is calibrated unloaded, its readout value corresponds to the same value on the feedback potentiometer, and hence to the corresponding actuator output shaft angle.

Using the ratiometer 2 and the meter 2, a set of measurements was taken to estimate the magnitude of the combined errors contributed by the servo electronics and the actuator. These error sources have an effect of producing an offset on the null reading of M2. During the subsystem integration test in which the servo loop was closed with the actuator, the error voltage at M2 was measured. When this value was reflected back to the ratiometer 2/M2 calibration data, the combined servo error contributed by the servo electronics, the actuator stiction and the servo-motor start voltage was determined. The magnitude of this error was 0.02 deg, which is well below the specified maximum value of 0.1 deg in an equivalent platform angle.

D. Sizing Results for Attitude-Control Gas Nozzles, *Spacecraft Control Section*

1. Introduction

One of the important activities in building an attitude-control gas system is the proper sizing of the gas nozzles to meet spacecraft control torque requirements. In order to perform this sizing, two aids are used. The first is a nozzle-sizing computer analysis program described in Ref. 1. The second is a thrust measurement stand described in detail in SPS 37-44, Vol. IV, pp. 41–42; SPS 37-50, Vol. III, pp. 112–114; and SPS 37-54, Vol. I, pp. 29–31. The procedure used was similar to the procedure developed for the *Mariner* Mars 1969 program with the following two exceptions (which necessitated additional test work):

(1) As seen from Table 1, the calculated thrust required about the roll axis is more than three times as high for the *Mariner* Mars 1971 spacecraft as for *Mariner* Mars 1969. This is due to the *Mariner* Mars 1971 requirement to counteract a potential 2 in.-lb of midcourse motor-generated swirl torque. Two inch-pounds is outside the range of the thrust stand used during the *Mariner* Mars 1969 mission, and it was necessary to extend the range and recalibrate the stand.

(2) The computer sizing program requires the discharge coefficient of the valve orifice as an input. Figure 1 is a computer-output-based curve of the thrust versus nozzle throat diameter (all other parameters held constant, as in Table 2), for two values of discharge coefficient (C_D = 0.62, 0.35). The curve indicates that the value of the discharge coefficient does not effect the thrust for levels up to 7 mlb. This is because the flow is controlled principally by the nozzle restriction (at the lower throat diameters (<0.020 in.) and not the valve orifice restriction. For the *Mariner* Mars 1969 spacecraft knowledge of the actual orifice discharge coefficient was not necessary, since the highest thrust level required was 5.43 mlb. This knowledge is necessary for *Mariner* Mars 1971, since the thrust level is 16.67 mlb. Thus, vacuum flow rate versus pressure drop tests were run to determine the correct discharge coefficients.

Table 1. Attitude-control thrust requirements

Maneuver	Principal moment of inertia, slug-ft^2	Control acceleration per half system, rad/sec^2	Moment arm, in.	Calculated thrust required for MM '71, lb	Calculated thrust required for MM '69, lb
Pitch	I_{xx} = 332	2.25×10^{-4}	128.5	6.97×10^{-3}	3.13×10^{-3}
Yaw	I_{yy} = 351	2.25×10^{-4}	128.5	7.38×10^{-3}	3.19×10^{-3}
Roll	I_{zz} = 408	a	120.0	16.67×10^{-3}	5.43×10^{-3}

[a]Must overcome a 2.0-in.-lb swirl torque from midcourse motor.

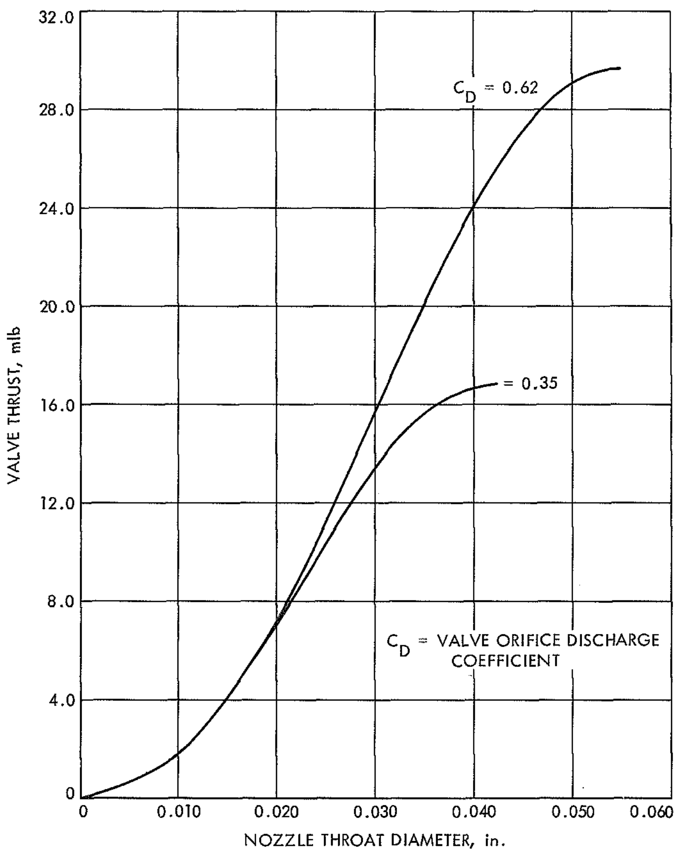

Fig. 1. Thrust versus nozzle throat diameter

Table 2. Initial conditions for nozzle-sizing computer program

Parameter	Value
Valve discharge coefficient	0.35, 0.62
Valve ball travel, in.	0.0068
Ambient temperature, °C	25
Valve ball diameter, in.	0.188
Valve seat diameter, in.	0.132
Nozzle geometric area ratio	50:1
Nozzle exit geometry half-angle, deg.	25
Ratio of specific heats (nitrogen)	1.4
Nitrogen gas constant, ft-lbf/lbm-°R	55.16
Ambient pressure, psi	0
Valve inlet pressure, psi	15.0
Nozzle throat diameter, in.	0.010 to 0.050 (variable)

2. Test Program Summary

A test program was set up to calculate the correct valve orifice discharge coefficient under vacuum conditions for various nozzle throat diameters ranging from 0.020 to 0.050 in. Flow rate and pressure drop were measured across the orifice, and the discharge coefficient was calculated. The results of this test are summarized in Fig. 2. As can be seen, the discharge coefficient varies with throat diameter. This information is then added to the computer sizing program. The results of running the program are shown in Fig. 3. The solid curve shows thrust versus throat diameter for a constant discharge coefficient of 0.62. The dashed curve shows the same results corrected for the varying discharge coefficient.

The test stand and procedure are described in detail in the SPS's in *Subsection 1.* Basically, the test setup is a vertical cantilever beam (also used as the gas feed line) pinned at the top. The valve and manifold are mounted at the bottom and at right angles to the beam. Displacement of the beam caused by the thrusting is measured by a differential transformer pickoff and recorded on a strip chart recorder. Damping was supplied with a mercury bath and paddle. A hanging steel ball is used for calibration. The tests were run in a vacuum. Three changes were made to this test stand for the *Mariner* Mars 1971 program. The first was minor modifications to the calibration fixtures to facilitate the larger calibration range required. The second was the replacement of the pressure gauge used to measure valve inlet pressure with a pressure transducer for faster response. The third was to increase the amount of damping by changing from mercury to Dow Corning DC200 (25,000 cS). The resulting extended calibration curve is shown in Fig. 4. This curve is slightly nonlinear at the high end. Five test

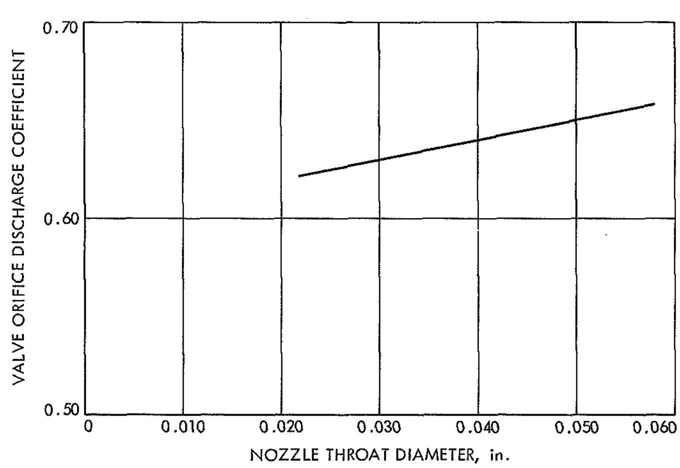

Fig. 2. Valve orifice discharge coefficient versus throat diameter

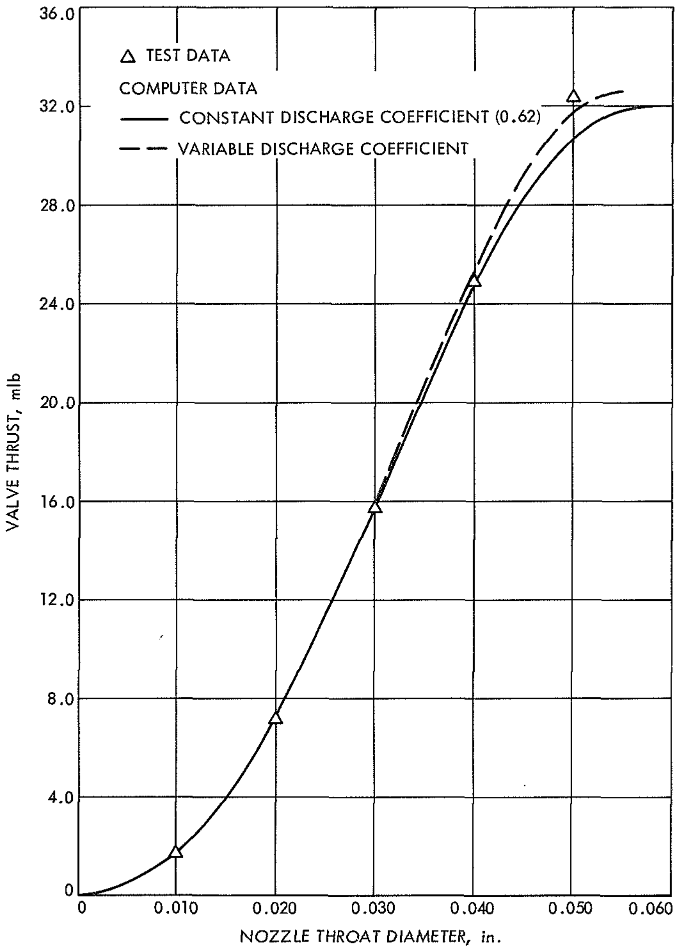

Fig. 3. Valve thrust versus nozzle throat diameter

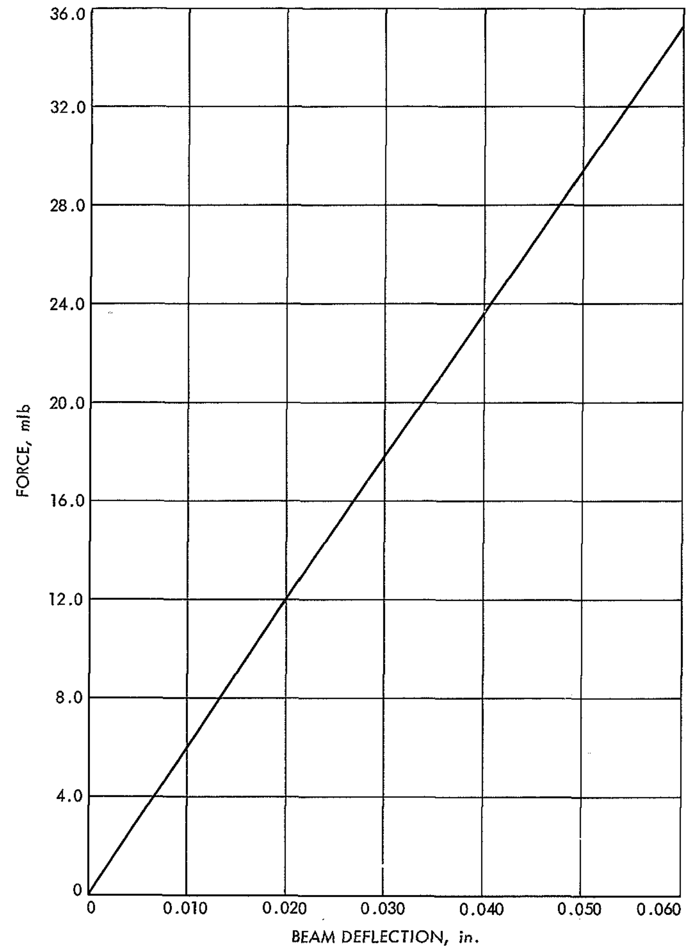

Fig. 4. Thrust stand calibration curve

nozzles were run, and the results are plotted as triangles on Fig. 3.

3. Conclusions

The following conclusions can be drawn from the above activity:

(1) The test range of the thrust stand has been extended from 10 to 32 mlb.

(2) The resulting agreement between test data and the computer program output is within 1% up to throat diameters of 0.40 in.

(3) All information required is available to completely specify the nozzles to be fabricated for the *Mariner* Mars 1971 spacecraft.

Reference

1. Ferrera, J. D., and McKown, P. M., "A Method for Calculating Steady-State Thrust and Flow-Rate Levels for *Mariner IV* Type Attitude Control Nitrogen Gas Jets," Technical Report 32-1353, Jet Propulsion Laboratory, Pasadena, Calif., Dec. 1, 1968.

E. Modeling of a Peripheral Belt Drive Magnetic Tape Transporter, *Spacecraft Data Systems Section*

1. Introduction

Since its rather recent inception, the peripheral belt drive mechanism for moving magnetic tape has continued to gain popularity, particularly in the field of satellite and deep space onboard recorder/reproducer subsystems. The peripheral belt concept offers several unique advantages over other more conventional approaches, including relatively low power consumption, light weight, improved packaging efficiency, and increased reliability. A further advantage is the adaptability of this type of drive to a wide range of tape widths, lengths, and tape elastic characteristics. Perhaps its most significant advantage is the way in which tape tension is developed by the mechanism. The peripheral belt drive develops tape tension as a function of the reel geometry, belts and tape elasticity, tape length, head drag, and the relationship of belt and tape membrane thicknesses. The tape tension is independent of power source, tape speed, and servo design. The tension does not depend on a stable reel torque bias as is the case with drives utilizing Negator-type spring motors or torquer reel motors. As such, the stability of the tension profile is dependent only on the characteristics of elasticity, friction, and geometry.

Because of the many advantages of the peripheral belt drive over some other types, it was selected for use in the *Mariner* Mars 1971 tape transporter. Although the drive concept had proved its feasibility prior to the time of selection for the *Mariner* Mars 1971 mission, it had not been adequately mathematically modeled to the point of a thorough understanding of the mechanism. Several attempts had been made to model the drive, with unacceptable results. Modeling the mechanism required a thorough understanding of elasticity and insight into the limits of a repetitive process.

Early in the developmental stages of the *Mariner* Mars 1971 program, one of the more common problems of low-speed recording developed. Tape stick-slip (random incremental tape velocity) was observed in the transporter. Stick-slip was clearly unacceptable. The reliable performance of the data storage subsystem depended on the ability of the transporter to move tape by the heads at a uniform velocity. It thus became clearly necessary to understand the mechanisms of the tape drive as it relates to stick-slip and that the problem be confronted on several fronts. The thorough understanding of the tape tension, tension variation, and mechanism for developing tape tension was considered imperative, since it became clear that stick-slip occurred at the tape-to-head interface. Toward this end, a rigorous analytical model of the transport drive was developed by the Engineering Mechanics Division at JPL. The quasistatic analysis was used to develop an expression for take-up tension as a function of: (1) pay-out tape tension, (2) deck reel and idler geometry, (3) static force and moment equilibrium, (4) belt and tape elasticity, (5) magnetic head drag, (6) tape length, and (7) the relationships between belt thickness and tape thickness.

2. Analytical Model

Figure 1 illustrates the general configuration of the *Mariner* Mars 1971 transporter tape deck. A tensioned seamless polyester drive belt (peripheral belt) is routed around the perimeter of the assembly simultaneously driving both the pay-out tape reel and the take-up tape reel. The belt transmits its motion into the tape packs via the friction interface between the belt and tape. As such, the stability of tape motion depends on establishing a nonslipping belt to drive/driven elements interface. The belt is driven by a capstan referred to as the "fast" capstan. The connotation comes from a condition where one of the two capstans is required to rotate with a greater peripheral velocity than the other, thus the distinction of fast capstan and slow capstan is applied. The slow capstan is caused to rotate with a lesser peripheral velocity than the fast capstan so that it appears as a load element to the motion of the peripheral belt. The two capstans are coupled by an elastic drive belt. The ratio of capstan velocities is referred to as the capstan differential and is nominally calculated from geometry assuming an infinitely stiff coupling belt. The load presented to the belt by the slow capstan requires that a tension change occur across the capstan. It can be shown by taking moments about the slow capstan that the belt tension approaching the slow capstan will be less than the tension leaving the capstan by an amount equal to the term $2\alpha\Delta T$, where α is the ratio of capstan input pulley diameter to capstan diameter, and ΔT is the tension difference developed in the capstan coupling belt. The increased tension in the belt leaving the capstan results in a reduced cross-sectional area of belt.

In order that continuity of mass flow in the belt be preserved, the velocity of the belt leaving the capstan must be greater than the velocity of the belt approaching the capstan. Thus, a tension and velocity differential is established across the slow capstan such that the velocity of the belt approaching the take-up reel tends to

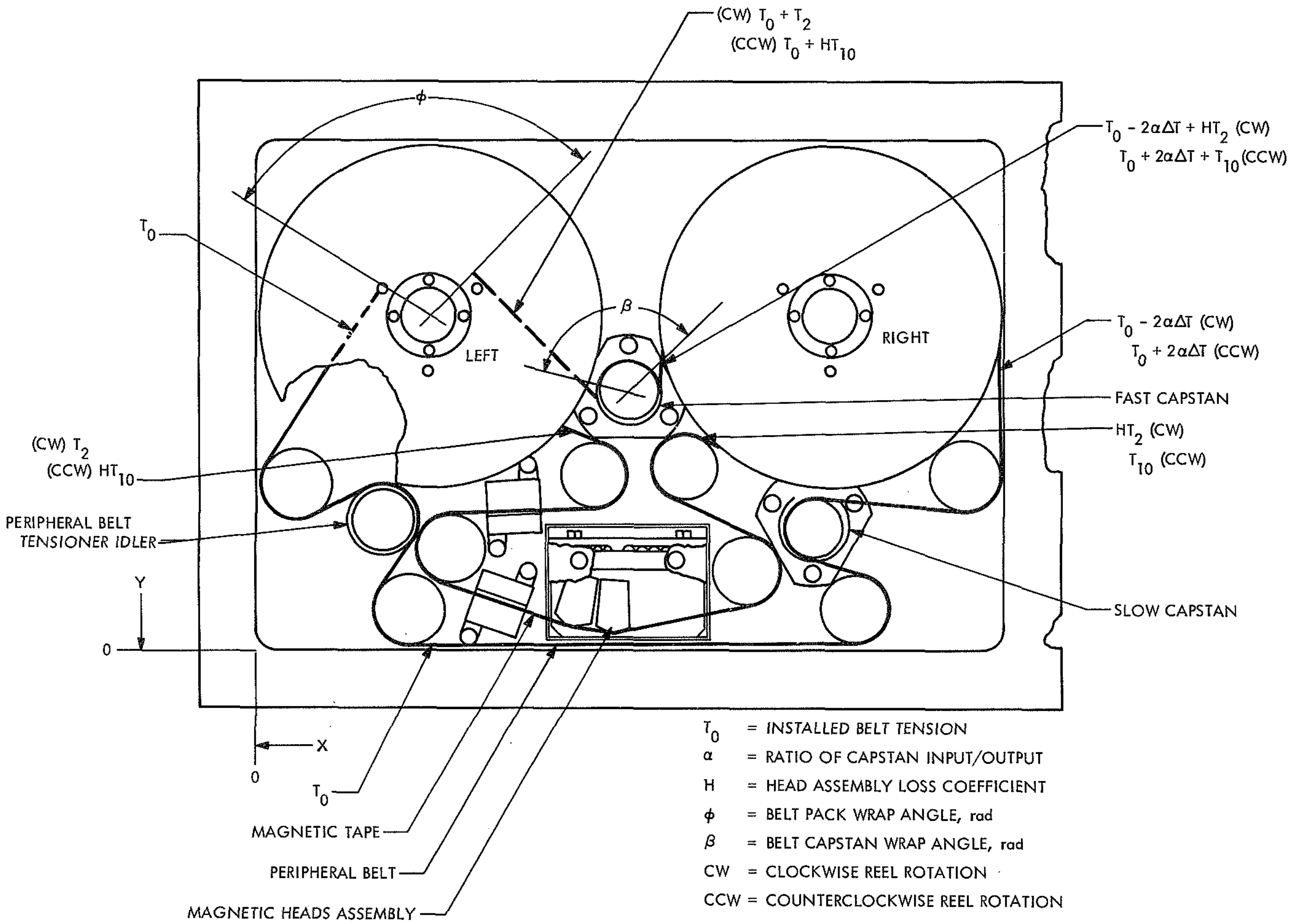

Fig. 1. Transport deck layout (top view)

be greater than the velocity of the belt leaving the pay-out reel. Note that the belt will neither pile up on itself nor fail in tension, since the mass flow is maintained as constant at any point in the path. The expression for tape tension is slightly different, depending on which reel is the take-up reel (tape direction). The difference results from geometrical asymmetry of the tape deck. It is assumed that no slip occurs on the leading edge of the capstans or tape packs with the belt, although some creep of the belt is required if a belt tension change is to occur. An "equilibrium" tape tension exists such that the take-up tension tends toward the pay-out tension (it must be remembered that the present pay-out tension is the previous take-up tension). The deviation from this equilibrium tension at the take-up reel is a constant ($0 < k < 1$) times the deviation at the pay-out reel. The tension does not approach the equilibrium tension as a limit because the tape motion is bidirectional, alternating between the two reels. If the tape motion were unidirectional, the take-up tension would equal the equilibrium tension in the limit. However, there exists an equilibrium tension loop, formed by the two tape direction tension curves, such that if the tension on the pay-out reel is on one branch of the loop, the pay-out reel will transfer to the take-up reel with a tension equal to the other branch of the loop. The general case of an equilibrium loop is shown in Fig. 2a. The loop has been referred to as a "bow tie" profile.

The analysis can be repeated assuming slippage occurs at the slow capstan. A different equilibrium loop will result yielding a lower level of tension characterized by excessive tension spikes just prior to the tape direction reversal. The analysis is carried through by assuming a variable differential and reducing the value of the differential to the point at which slip is impending. The time rate of change in tension is found to be sufficiently small to warrant omission except at the transition from take-up to pay-out, which occurs during a direction reversal. At this time, a tension peak is formed causing the tension to approach the hypothetical equilibrium limit associated with the direction of prior motion.

As a result of the analysis, several changes were implemented in the transporter to: (1) reduce the average tape tension at the heads and reduce the range of tape tension and (2) remove certain instabilities (i.e., capstan slippage) that existed in the tape drive. Figure 2a illustrates a typical tension profile measured prior to the changes. Figure 2b illustrates the improved profile resulting from the analysis. The analytical model has been verified in accuracy by numerous tests of different configurations and represents a very powerful tool for optimization of a particular peripheral belt drive. The most significant parameter in establishing a uniform tape tension over the tape length was found to be the radial distance separating the elastic center of the peripheral belt from the elastic center of the magnetic tape. Reduction of the peripheral belt thickness and modulus of elasticity are the most important parameters to reduce mean take-up tension as well as making it more uniform. The complexity of the expression for tape tension is such that one must be very careful in generalizing the effect of one parameter variation on the tape tension.

The proper design of a peripheral belt drive must take into consideration not only tape tension, but also (1) capstan slippage, (2) belt/tape pack slippage, (3) head drag,

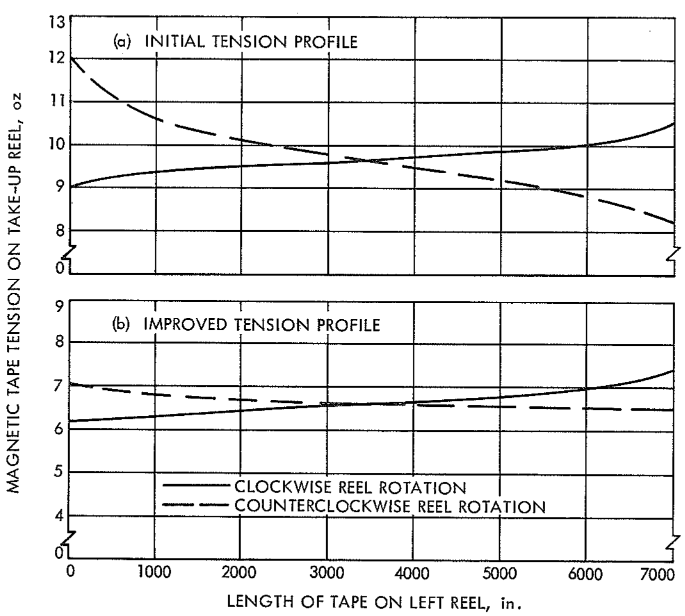

Fig. 2. Magnetic tape tension profiles

(4) membrane stress and fatigue levels, and (5) drive system torque transmissibility. In the final analysis, stability of tape motion and tension can be assured only if proper attention is given to the total design of the drive mechanism. Considering the unique geometric and elastic relationships of the *Mariner* Mars 1971 transporter, some specific statements can be made about ramifications of some single parameter variations. Some of the more interesting are listed in Table 1.

Table 1. Parameter variations

Variation	Effect
Capstan coupling belt stiffness	Changes tape tension. Little effect on tension range
Peripheral belt width	Changes tape tension. Little effect on tension range
Magnetic tape modulus	Changes tension range. No effect on average tape tension
Magnetic tape thickness	Changes both average tension and tension range
Capstan differential	Changes average tension. No effect on range
Peripheral belt thickness	Changes average tension and range.
Head Loss	Changes average tension. Little effect on range

Because of its dependency on elasticity, tape tension is sensitive to temperature changes to the same degree that the membrane elastic modulus is sensitive to temperature changes. In designing a peripheral belt transporter to operate under wide temperature limits, one must consider the possible changes in elastic properties of belts and tape. A properly analyzed drive would express the elastic constants as functions of temperature, as indeed they are. This understanding could lead to a temperature-compensating design which would set the tape tension as a constant and yield the required temperature–elasticity relationships between the various elastic elements. A further approach would be to fabricate the capstans each of materials different in temperature expansion characteristics so that the tendency toward elastic change would be negated by a change in capstan differential.

3. Conclusions

As a result of the analytical modeling, the mechanism inducing tape tension is more clearly understood. Many variables are involved in the development of tape tension. The complexity of the expressions does not allow generalization of parameter variation ramifications, nor can an analysis performed for a particular set of deck geometry be directly applied to a different set of geometry. The complexity of the mechanism requires that the breadboarding be first done analytically and that parameter variations be explored in the same manner. Any commitment to develop a peripheral belt drive for a particular requirement should include the commitment to fully model the transport analytically prior to accepting the design.

F. Propulsion Subsystem, *Liquid Propulsion Section*

1. Introduction

The *Mariner* Mars 1971 spacecraft incorporates an on-board modularized propulsion subsystem to furnish impulse to the spacecraft for trans-Mars trajectory correction, orbit insertion, and orbit trims. The propulsion subsystem operates on liquid propellants: nitrogen tetroxide (N_2O_4) and monomethylhydrazine (MMH). The subsystem is a regulated-pressure constant-thrust system employing: (1) gaseous nitrogen pressurant stored at 3650 psia within two 15-in.-diam titanium vessels, (2) Teflon-bladdered 30-in.-titanium propellant tanks, capable of storing 635 lb of N_2O_4 and 410 lb of MMH, (3) two pressurant check and relief valve assemblies, (4) explosively actuated isolation valves in both the pressurant and liquid circuits, and (5) a 300-lbf-thrust conduction-cooled rocket engine.

2. Effects of Propellant Saturation With Gaseous Nitrogen on Hydraulic Resistance

Rocket engine tests using nitrogen-saturated propellants were conducted early in the engine prequalification test program. These tests verified previous test indications that saturated propellants produce an increase in the oxidizer flow circuit hydraulic resistance resulting in decreased oxidizer flowrate and engine mixture ratio. The magnitude of this mixture ratio decrease was from 5 to 8% for full saturation at propellant tank pressures of 250 psig. The allowable mixture ratio uncertainty for the *Mariner* Mars 1971 propulsion subsystem is $\pm 3\%$. Therefore, it was obvious that propellant saturation would have to be a major consideration in the characterization of the *Mariner* Mars 1971 engine operation.

Two basic approaches were considered to obtain the test data necessary to characterize engine performance with saturated propellants:

(1) Expand the engine prequalification and qualification test programs to obtain the basic performance characterization with additional testing at the subsystem level for verification.

(2) Initiate cold-flow testing of a breadboard system using simulated or flight-like components with verification tests at the engine or subsystem level.

The cold flow test approach was chosen primarily on the basis that cold-flow testing could be conducted with minimum interference to current component test programs. Greater flexibility in terms of configuration and test operation, and reduced cost per test were also decided advantages.

3. Discussion

The simulated oxidizer flow circuit consisted of six thin flat-plate orifices as shown in Fig. 1. The orifices were sized to simulate the pressure losses of the principal subsystem components: propellant standpipe, squib valve package, filter, engine calibration orifice, propellant valve, and injector.

Pressure transducers were used to determine the pressure drop across each orifice. Turbine-type volumetric flowmeters, one upstream and one downstream of the orifices, were used to determine the flowrate.

Propellant saturation was accomplished by bubbling gaseous nitrogen through the propellant for approximately one-half hour while maintaining the proper back-pressure. The propellant then remained undisturbed for one-half hour before a propellant sample was drawn from the tank.

Flow tests using first nonsaturated and then saturated oxidizer were conducted with no measurable change in hydraulic resistance in any of the orifices. The increased speed of the downstream flowmeter during the saturated tests indicated the presence of evolved gas. Orifices 3 and 5 were removed and replaced by a 30-μm flight-type filter and a flight-type propellant valve. The flow tests were then repeated with no change in hydraulic resistance.

A simulated oxidizer injector plate was designed and fabricated to replace orifice 6. The simulated injector contained the same number of orifices, the same nominal orifice size, and the same orifice L/D as the *Mariner* Mars 1971 engine injector. The flow tests were repeated, and an increase in the injector resistance was noted with saturated propellants. Additional testing was conducted with the oxidizer saturated at various pressure levels. The resulting resistance increase with gas saturation is presented in Fig. 2. Several data points from the engine margin limit test program are also shown for comparison. The resistance increase is plotted against the volume of gas out of solution upstream of the injector. Good agreement is shown between the cold-flow data and the engine test data.

The volume of gas out of solution was calculated, based on the injector inlet pressure and Henry's constant for solubility.

$$V_{out} = V_{tank} - K(P_{inj} - P_v)$$

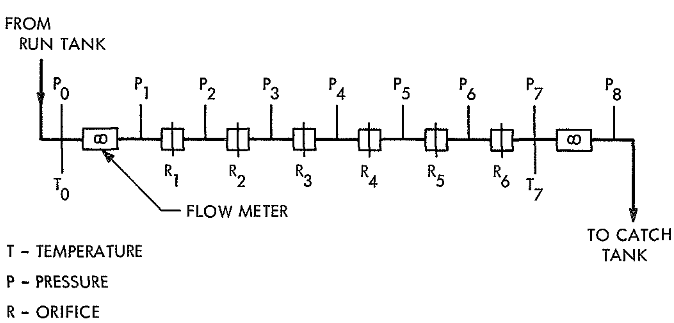

Fig. 1. Flow bench schematic

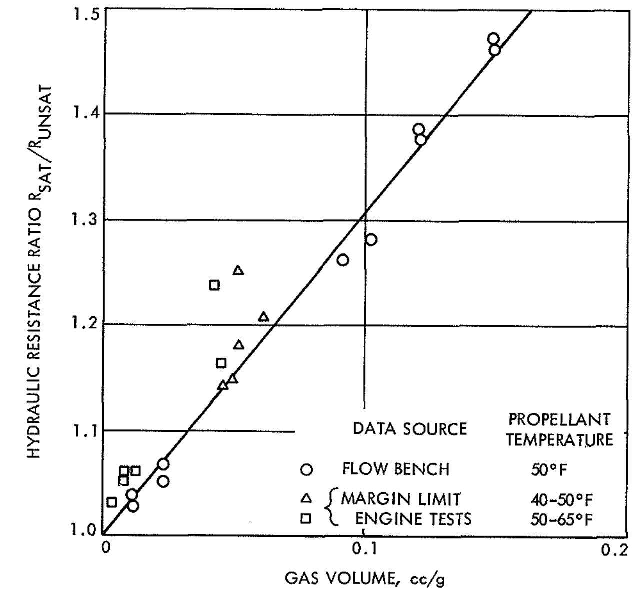

Fig. 2. Injector resistance for nitrogen-saturated oxidizer

where

V_{out} = volume of gas out of solution, standard cc/g

V_{tank} = volume of gas in solution at the propellant tank, standard cc/g

K = Henry's solubility constant – 0.01 scc N_2/psi-g oxidizer

P_{inj} = injector inlet pressure, psia

P_v = vapor pressure of oxidizer

This method and the data plotted in Fig. 2 were used to predict propellant consumptions for the engineering test model and type-approval model test programs. Propellant consumptions were predicted on the oxidizer side for both saturated and unsaturated conditions to within 1%.

Tests were also conducted with saturated fuel (monomethylhydrazine) using an orifice plate simulating the engine fuel injector orifices in a flow bench configuration. These tests revealed the resistance increase for full saturation to be about 1%. This agreed with engine test results, but some system tests have indicated a possible increase in fuel resistance of about 2%. This result is currently being investigated.

4. Conclusions

The following conclusions can be drawn, based on the results of nitrogen-saturated propellant tests conducted in support of the *Mariner* Mars 1971 propulsion subsystem development program:

(1) The volume of nitrogen which remains in solution is directly related to the partial pressure of the nitrogen for both oxidizer (N_2O_4) and fuel (MMH).

(2) The primary increase in resistance due to evolution of dissolved gas occurs in the relatively long orifices ($L/D = 10$) of the rocket engine injector.

(3) The increase in resistance across the injector is proportional to the volume of gas out of solution upstream of the injector orifices as indicated in Fig. 2 for the oxidizer.

(4) The increase in injector resistance in the fuel flow circuit with saturated propellant was about 1% for full (250 psig) saturation.

G. Effect of Solvent on the Biaxial Properties of Liquid Propellant Expulsion Teflon Bladder Bags, *Polymer Research Section*

1. Introduction

Standard laminate Teflon bladder bags employed as liquid propellant expulsion devices for the *Mariner* Mars 1971 spacecraft have been failing due to the formation of tears and cracks near an aluminum seal ring which forms the mouth of the bag. These failures were occurring during flight-acceptance tests in which various solvents were used as referee fuels. From a consideration of the conditions imposed on the bags during the tests, it was recognized that the neck region of the bags are biaxially stressed while at the same time being bathed by the test solvent. A previous report (SPS 37-65, Vol. I, pp. 40–42) has demonstrated that standard laminate is extremely sensitive to solvent, a property which results in a marked reduction in the materials uniaxial stress–strain properties. This report gives the results of a study on the effects of solvent on the biaxial properties of standard laminate materials. Also included are test results obtained on a new candidate material designated "codispersion laminate," as well as a study of the effect of solvents on FEP 120, FEP 9511, and TFE 30, the Teflon components which are used in the construction of the laminate materials.

The effects of these solvents on the biaxial properties of standard and codispersion laminate were as follows:

(1) Standard laminate is sensitive to solvent and fails from solvent-stress cracking at strains less than 6% when biaxially stressed. This characteristic is undoubtedly the prime cause of failure of standard laminate bladder bags when exposed to solvent during flight-acceptance tests, where failure occurred from the formation of cracks and tears in the highly biaxially stressed neck regions of the bladder bags.

(2) Codispersion laminate, on the other hand, offers a significant improvement in resistance to solvent-stress cracking. The poorest case is for Freon-TF exposure, wherein biaxial failure occurs at 28% strain. However, presoaking in Freon-TF prior to biaxial testing results in a significant increase in strain at failure from 28 to 128%.

(3) A study of the solvent sensitivity of FEP 120, FEP 9511, and TFE 30, revealed that only FEP 120 is significantly solvent sensitive. This material, not used in codispersion laminate, is a major component of standard laminate and must, therefore, be labeled as the dominant contributor to the solvent sensitivity of standard laminate. This is further substantiated by the experimental observation that surface crazing which precedes the failure of the standard laminate in solvent occurs in FEP 120.

2. Experimental

a. Biaxial test. The biaxial test consisted of straining a test sample whose width is very large compared to the test length. In this way, as the material is strained by a uniaxial extension along the test length, the large width will prevent the material from necking, thus creating a transverse biaxial stress. In uniaxial testing, where the test width is small compared to the test length, the necking which occurs as yield stress is approached causes the test width to be diminished due to the Poisson effect. In the current test, the material is constrained against transverse necking; and, as a result, a biaxial stress field is imposed on the sample.

The biaxial test specimen is shown in Fig. 1a. The dotted parallel lines are employed during test to allow visual verification that no transverse contraction is occurring, while the two solid lines are grid lines employed for strain determination. They are separated by 0.5 in. and positioned symmetrically around the center point. Crosshead speed on the Instron is 0.2 in./min which allows time to observe the specimen as well as to monitor the grid line separation for strain measurements. One half inch of the top and bottom of the specimen are held by the biaxial Instron grips. Details of the test set-up and immersion bath are shown in Fig. 1b.

The solvents employed were heptane, isopropyl alcohol, and Freon-TF. The latter two solvents were selected because they are employed as the referee fluids in the flight-acceptance testing of the bladder bags, while heptane was included because it has a known effect on Teflon materials.

b. Bladder construction details. Details of construction of the bladder bags are shown in Fig. 2. Standard laminate is a two-ply construction consisting of one ply of FEP 120 and another ply of TFE 30. Codispersion laminate is a three-ply construction consisting of an inner ply of FEP 9511, while the two outer plys are formed from a codispersion of 80% TFE 30 and 20% FEP 9511.

3. Results

a. Biaxial test on standard laminate. A summary of the biaxial stress–strain properties for the standard laminate is shown in Fig. 3. The solid line is the stress–strain curve obtained for three control specimens which were tested in air, showing the positions at which each of the specimens failed. The strain at break ranged from 40 to 108%, and inspection of the failed specimens revealed a correlation between the strain at break and the extent of delamination of the two plys along the fracture line. The sample failing at low strain underwent very extensive delamination, whereas the sample failing at high strain showed no evidence of delamination. This is reasonable, for it is known (Ref. 1) that FEP 120 fails biaxially near 30% strain, and TFE 30 fails near 270% of strain. Hence, if delamination occurs, there is no reinforcement of the weaker FEP 120 by the stronger TFE 30 and a low strain failure will occur.

For the solvent study, samples were tested after initial exposure to solvent and after a two week presoak. Though no effect of aging of the material in solvents was observed, the overall effect of solvent was significant. The solid symbols on the solid line in Fig. 3 locate the positions at which the standard laminate materials failed biaxially. The effect is dramatic, for it was found that standard laminate fails at strain levels less than 6% as a result of solvent exposure. Since these strain levels are easily achieved by the bladder bag when filled with solvent and subjected to flight-acceptance test, the solvent-stress cracking of standard laminate emerges as the prime mechanism of bladder bag failure. This can be seen further by comparing the formation of cracks and tears in the biaxial test samples, as shown in Fig. 4, with the same sequence of events occurring to the bladder bags, shown in Fig. 5.

Figures 4a and 5a show the initial formation of surface crazing, while Figs. 4b and 5b show the resultant formation of a crack. For the biaxial test specimen, this was considered failure and corresponds to the dark symbols on the stress–strain curve in Fig. 3. Figure 4c is a close-up detail of the crack separation in the biaxial sample. Figures 4d, 5c, and 5d detail the subsequent tearing of the material after the crack separation has occurred.

b. Biaxial test in codispersion laminate. Codispersion laminate offers significant improvement in the resistance to solvent–stress cracking. This can be seen in the biaxial stress–strain results for isopropyl alcohol and heptane exposure shown in Fig. 6, and for Freon-TF exposure shown in Fig. 7. Although the displacement of these curves from the control indicates some solvent effect, the strain at break is still high for biaxially applied stresses. Further, the fractures were clean, with no delamination, and with no crazes or cracks occurring on the surface of the materials prior to break.

The only solvent effect of any significance occurred for sample exposure to Freon-TF, where the strain at break was at a surprisingly low 28% (curve I in Fig. 7).

Since this low strain was observed on specimens tested immediately after exposure to Freon-TF, samples were presoaked for periods up to 2 wk and then tested with the result (curve II in Fig. 8a) that the strain at

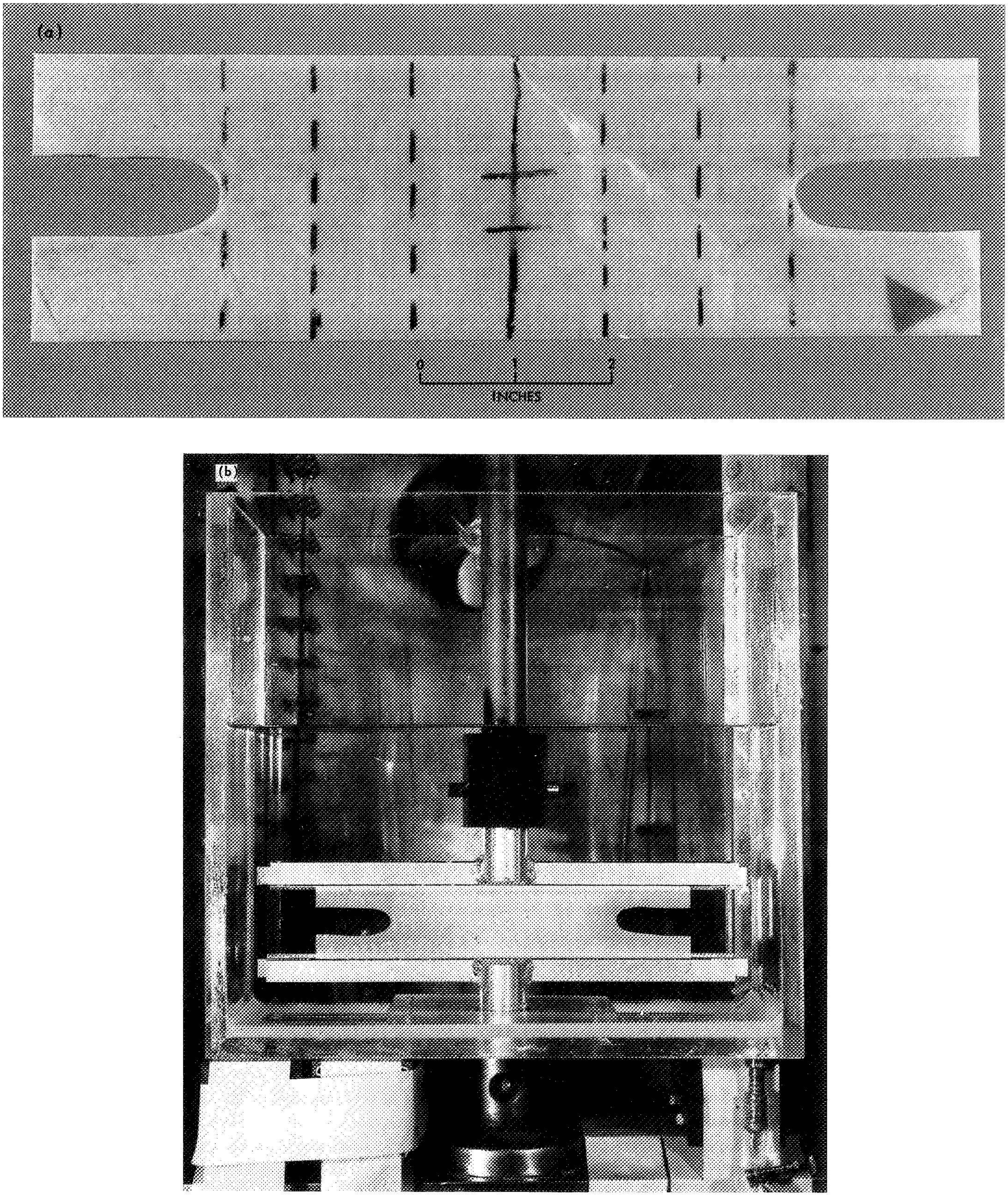

Fig. 1. Biaxial test specimen and test apparatus with immersion bath

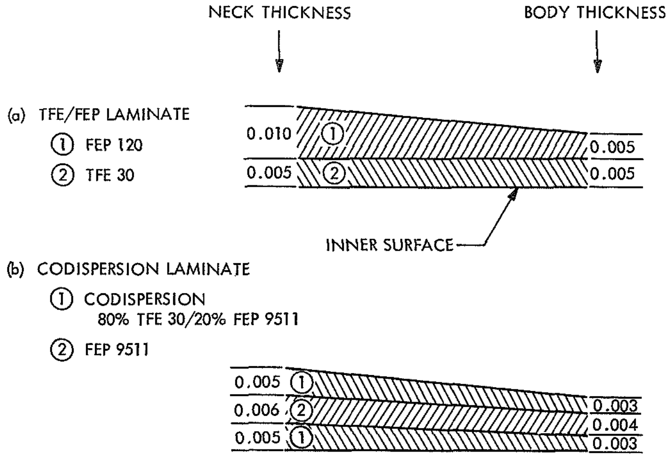

Fig. 2. Bladder construction details

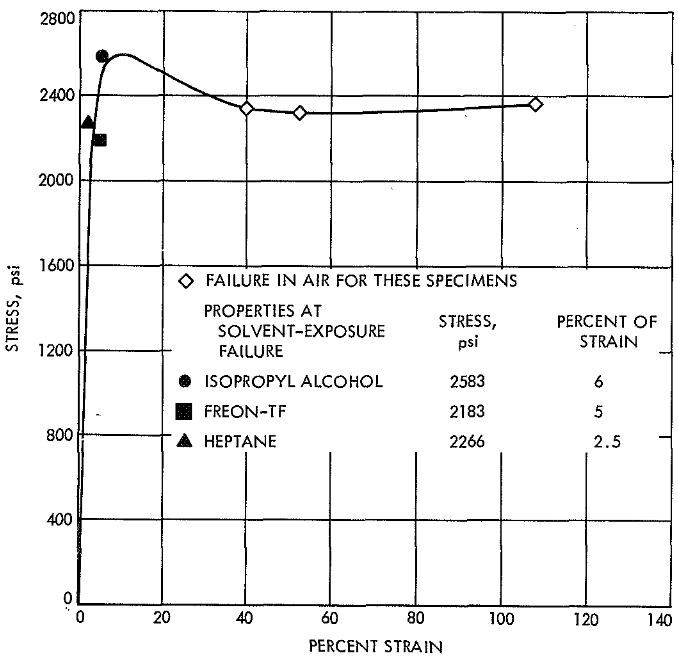

Fig. 3. Biaxial stress–strain properties for standard laminate

break increased to 128%. A speculation on the origin of this effect will be discussed under the section on fracture mechanics. There was no effect from presoaking codispersion laminate in heptane and isopropyl alcohol.

c. Solvent studies of bladder bag components. The effect of solvent on the bladder bag components FEP 120, FEP 9511, and TFE 30 was assessed by measuring the uniaxial stress–strain properties of these materials while they were completely immersed in solvent. The results (Table 1) reveal that FEP 120 is extremely solvent-sensitive, while FEP 9511 and TFE 30 are virtually resistant to any solvent attack. Thus, the solvent sensitivity of standard laminate appears to be related to the FEP 120, a conclusion further supported by the experimental observation that the surface crazing

Table 1. Effect of solvent[a] on bladder bag components FEP 120, FEP 9511, and TFE 30

Component	Percent of Crystallinity	Yield stress, psi	Ultimate stress, psi	Ultimate strain, %
FEP 120	29			
Tested in air		2188	3380	435
Freon-TF		1998	2031	124
Heptane		2077	1854	148
Isopropyl Alcohol		2118	3253	399
FEP 9511	22			
Tested in air		2034	3569	362
Freon-TF		1882	4459	408
Heptane		1965	3566	334
Isopropyl Alcohol		1998	3536	323
TFE 30	45			
Low crystallinity				
Tested in air		1421	4968	590
Freon-TF		1276	4983	639
Heptane		1329	4926	568
Isopropyl Alcohol		1471	5479	548
TFE 30	73			
Middle crystallinity				
Tested in Air		1641	3732	695
Freon-TF		1777	2597	570
Heptane		1835	3306	517
Isopropyl Alcohol		1786	4045	580
TFE 30	83			
High crystallinity				
Tested in air		1937	3686	681
Freon-TF		1870	3120	564
Heptane		1934	3539	515
Isopropyl Alcohol		1973	3641	447

[a]Assessed by measuring the uniaxial stress–strain properties while immersed in solvent. In Fig. 9, a typical stress–strain curve is shown for these materials when tested in air. Solvent exposure does not alter the basic shape of the curve, but can affect the magnitude of the stress and strain at break (ultimate properties), and the yield stress. Solvent attack is identified by a decrease in ultimate strain, while plasticization is identified by a decrease in yield stress.

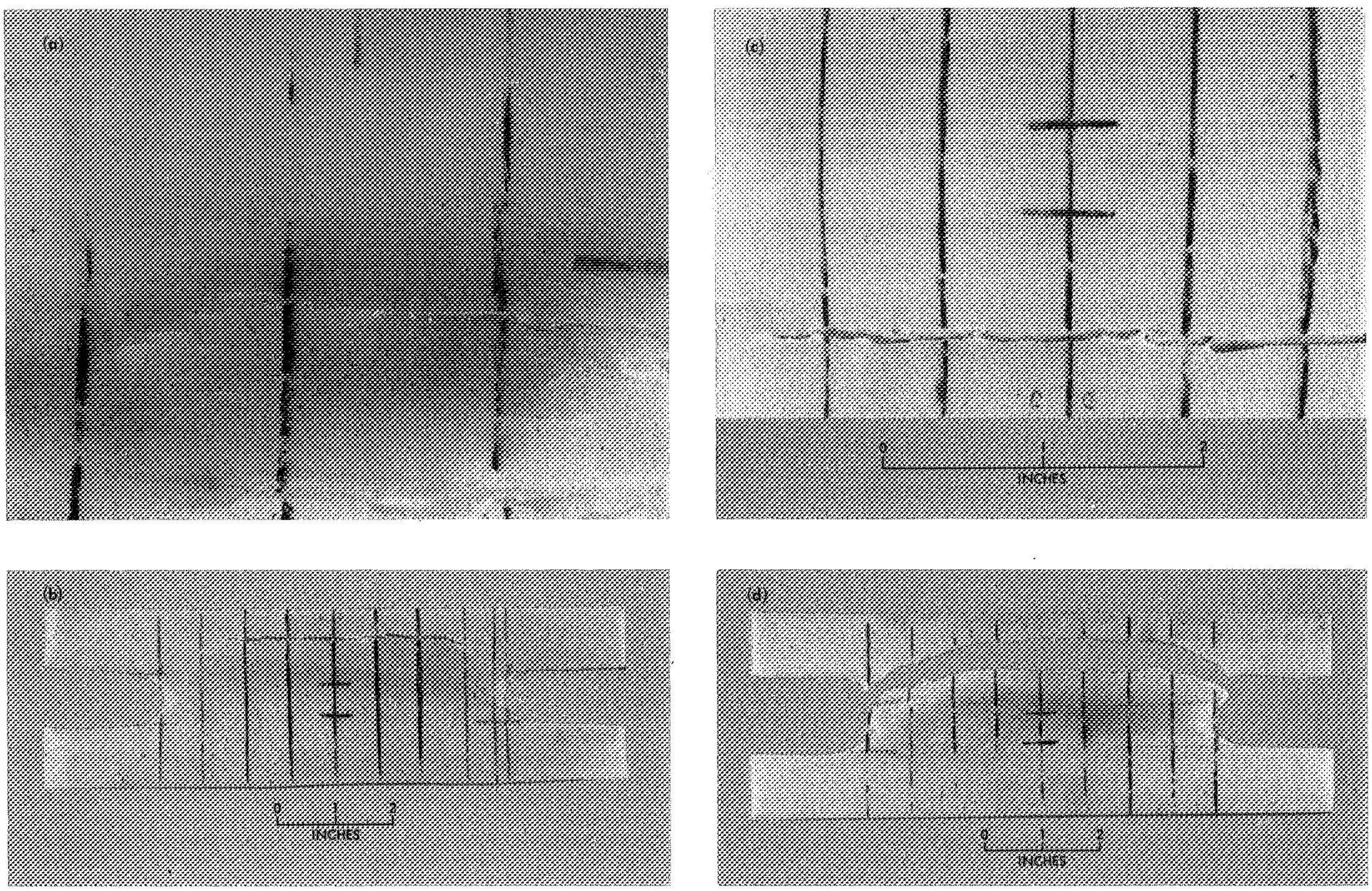

Fig. 4. Failure of standard laminate in solvent: (a) surface crazing in FEP 120 layer for biaxial strains from 1 to 5%, (b) cracks forming from crazes adjacent to Instron grips, (c) close-up detail of crack, (d) resultant tear from crack

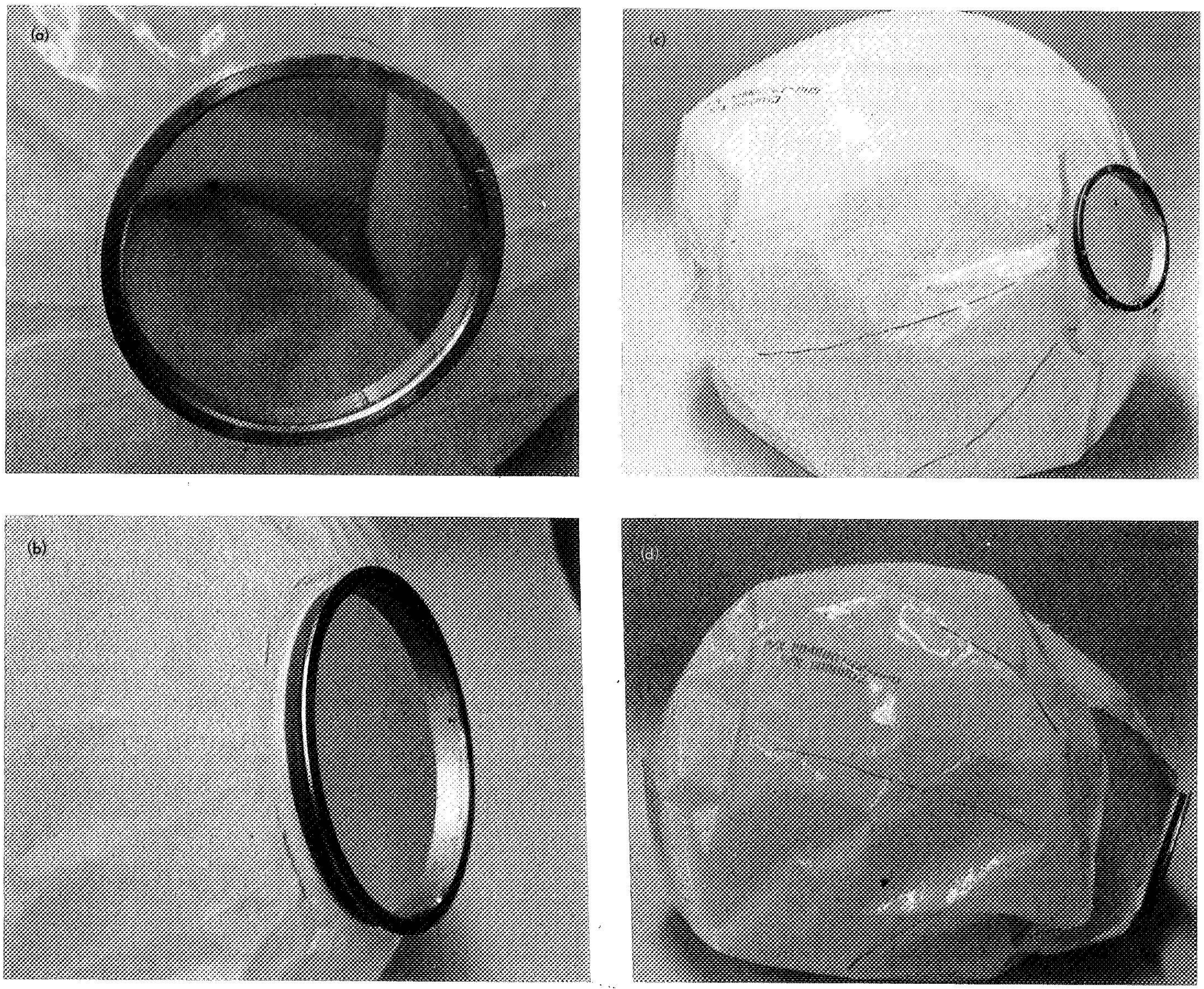

Fig. 5. Failure in neck region of standard laminate bladder bag: (a) crazing from solvent exposure, (b) cracks, (c) tearing resulting from cracks, (d) advanced tearing and total failure

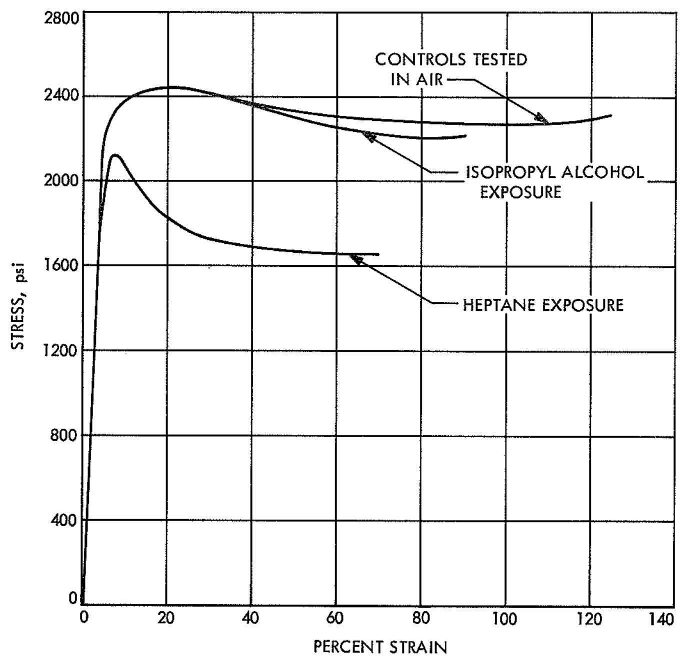

Fig. 6. Biaxial stress–strain properties for codispersion laminate

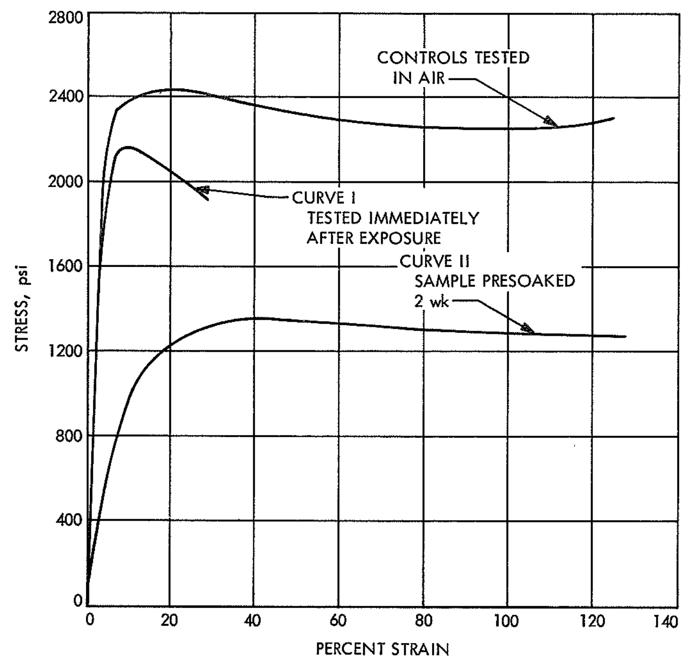

Fig. 7. Biaxial stress–strain properties for codispersion laminate exposed to Freon-TF

of the standard laminate (Fig. 4a) always occurs on the FEP 120 side.

d. Fracture mechanics. The significance of the failure of the biaxial specimens to the failure of standard laminate bladder bags and the low strain failure of Freon-TF exposed codispersion laminate is discussed here.

The fracture line for both standard and codispersion laminate air-tested samples occurred in the central portion of the specimen (Fig. 8a and b), as it also did for the codispersion specimens tested in heptane and isopropyl alcohol (Fig. 8c). However, the fracture line for the codispersion laminate initially exposed to Freon-TF and for all the solvent-exposed standard laminate specimens occurred (Fig. 4b) along a straight line which was parallel to and within 0.25 in. of the Instron grip. For the standard laminate, the fracture separation occurred in a craze which had previously developed adjacent to the grip, while the Freon-TF exposed codispersion laminate specimen developed no crazes or cracks prior to failure and broke cleanly at 28% strain. These observations were repeatedly confirmed.

Thus it must be concluded that for standard laminate, failure in the presence of solvent begins with the development of surface crazes in the FEP 120 layer at very low strains ($<< 6\%$), and those crazes which are immediately adjacent to where the material is mechanically constrained (i.e., Instron grips) develop into the cracks which characterize the failure of standard laminate. These observations from the biaxial testing explain why the crack separations occur in the neck, because it is here where the material, as in the Instron grips, is both biaxially stressed and mechanically constrained by being bonded to the aluminum seal ring. Further, presoaking of standard laminate prior to test does not affect either the low strain at failure or the location of the fracture line.

Presoaking codispersion laminate in Freon-TF, however, results in both a change in the level of strain at failure and the location of the fracture line, which moves up into the central portion of the test specimen. And, there is no crazing in the material to account for the low strain failure. Therefore, the low strain failure of the Freon-TF exposed codispersion laminate must arise from a different mechanism.

It is known that Freon-TF will swell codispersion laminate. Hence, speculatively, initial exposure to Freon-TF could have resulted in swelling of the free central portion of the specimen while that portion in the Instron grips is mechanically prevented from swelling.

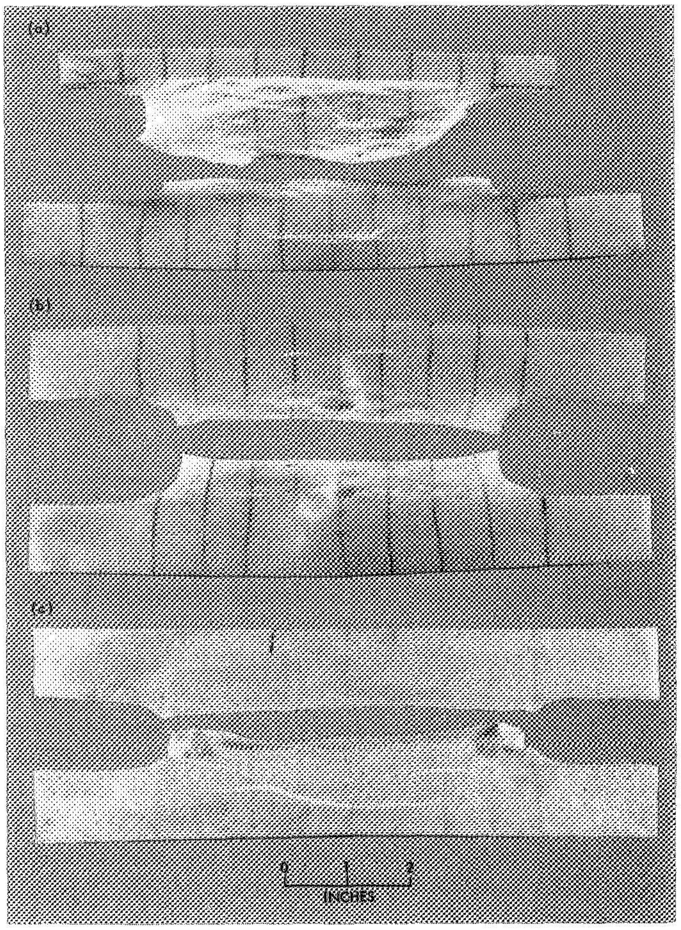

Fig. 8. Fracture lines for: (a) air-tested standard laminate, (b) air-tested codispersion laminate, (d) solvent-tested codispersion laminate

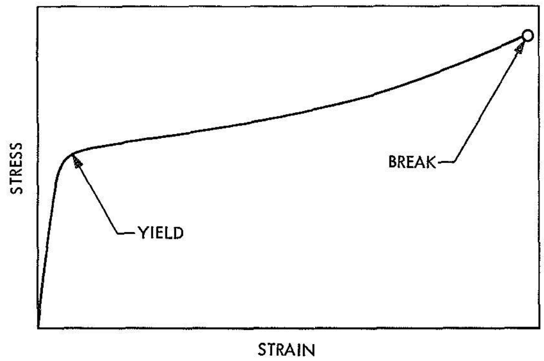

Fig. 9. Stress-strain curve typical of Teflon bladder bag materials

Thus, this may have established a differential stress across the material at the boundary of the grip, a stress sufficient to lead to premature failure near the grip. Presoaking the material prior to test allows the whole specimen to swell, and this acts to prevent the conditions leading to the premature failure.

If this hypothesis has any merit, some attention may have to be given to the flight-acceptance testing of codispersion laminate bladder bags when Freon-TF is employed as a referee fuel.

Reference

1. Krusos, J. N., Higgins, R. G., and W. H. Dukes, *Design Criteria and Quality Control Studies for Teflon Expulsion Bladders*, Report 8460-933012, Bell Aerosystems Company, March 1967.

H. Spacecraft Mass Property Determination,

Advanced Projects Development Section

1. Mass Property Requirements

The spacecraft weight and approximate center-of-mass are required for launch vehicle performance calculations. The weight must also be known to calculate spacecraft ΔV capability. Both center-of-mass and inertias are needed for autopilot stability and performance analyses. Inertias are also required for attitude-control gas consumption estimates. All mass properties are needed for spacecraft/launch vehicle separation analysis.

2. Mass Properties Assignments

All mass properties control, as well as publishing and transmitting mass properties information to interested persons, was handled by the System Design Section in the Project Engineering Division. Examples of control are the establishing of weight allocations, establishing center-of-mass envelopes, and resolving violations (or anticipated violations) of these. The Engineering Mechanics Division determines the mass properties, and maintains the following information:

(1) Current mass properties for components from the subsystems.

(2) A component properties list sufficiently detailed to provide a reasonable input to the mass properties computer program.

(3) A mass properties computer output of current estimates of spacecraft mass properties.

(4) Measurements of spacecraft mass properties.

(5) Periodic reports of spacecraft mass properties to the System Design Section.

3. Analytical Activities

The bookkeeping system selected was an indented list corresponding to the spacecraft drawing tree. This list is referred to as the weight list by drawing tree, or simply the master list.

Each line contains four entries: part number, description, reference designation, and current weight. The reference designation is the designator given the formal equipment and weight list (M71-3-230). The reference designation is included on the master list so that a list by subsystem can be generated. The last entry is the current weight. The value of the current weight is a representative or typical value for the flight part. In contrast to the system for the *Mariner* Mars 1969 spacecraft, no attempt is made to keep track of the actual weights of various serially numbered parts.

The weight list by drawing tree requires two types of information: format information and weights. From this weight list, two other lists were generated. One was the mass properties computer program input; the other was the subsystem or weight list by subsystem, which is generated by sorting on the reference designation entry in the master list. The subsystem list is generated for use by the Systems Design Section for mass property control.

A reference designation of 2000 is used for items that are not delivered to the spacecraft assembly facility as part of a subsystem. This is mainly system level installation fasteners (e.g., screws, cable clamps, etc.).

The mass properties computer program requires as input the weight, center-of-mass location, and local moments and products of inertia for each item on the spacecraft. It computes the weight, center-of-mass location, and inertias for the composite spacecraft. The inputs to the program are taken from the weight list to assure that nothing is left out or counted twice. Also, changes made to update the master list are easily transferred to the computer input list. A list of items corresponding to the drawing tree clearly satisfies the bookkeeping requirement. It also satisfies a convenience of calculation requirement because the drawing tree is organized largely on the basis of assembly sequence. Thus it consists of physically removable assemblies which are, in turn, made up of smaller physically removable assemblies. Usually at some level of detail, a convenient package for the calculation of local mass properties is listed.

At specified intervals, all the estimates were brought up to date and submitted to the computer for calculation of composite spacecraft mass properties. A report was made that consisted of a weight summary, a table of spacecraft mass properties for several configurations, a copy of the weight list by drawing tree, and a copy of the weight list by subsystem. The weight summary was a tabulation of the total separated weight (adapter is not included) of each subsystem and a total spacecraft weight. Changes from the previously reported weight were explained. The table of mass properties lists weight, center of mass, and moments and products of inertia for the spacecraft in each of several standard configurations.

4. Measurement Activities

In the *Mariner* Mars 1969 calculations, weight and center-of-mass were both calculated and measured; the inertias were calculated only. The propulsion subsystem on *Mariner* Mars 1971 is much larger and relocated from the *Mariner* Mars 1969 position. The result was that the x-y axis center-of-mass test fixtures were still suitable, but the z axis center-of-mass fixture was not. Additionally, the *Mariner* Mars 1971 gimballed motor provides more thrust axis control than the *Mariner* Mars 1969 jet vanes. These factors greatly reduced the accuracy requirements on the z center of mass.

Based on these calculations the plan for *Mariner* Mars 1971 mass properties determination was formed. The desired accuracies for final determination of mass properties were established. These are based only on *Mariner* Mars 1969 experience and existing measurement and calculation capabilities. The weight and x-y center-of-mass of the assembled spacecraft are measured on the proof-test model (PTM) and on the flight spacecraft.

The PTM measurements are made both wet and dry (with and without referee fluids simulating the propellants), but those for the flight spacecraft are measured dry only. The dry measurements are to provide the final values for weight, x and y, since the measured values are better than the calculations. The center-of-mass along the z axis will not be experimentally determined. In addition, the actual measurements will show differences between spacecraft, which the calculations do not.

Another reason for the measurements is to build confidence in the calculations. For example, if the measured values of x and y agree within 0.10 in. of the calculated values, and if the measured value is known to 0.05 in., then the calculations of x and y will be accurate to 0.15 in. Since the method of calculating z is the same for calculating x and y, it is reasonable that z is also accurate to 0.15 in. Agreement between calculated values for weight and locations (x and y) also implies correctness of inertias. Measurement of the referee propellant-loaded PTM provided another verification: agreement between the calculated weight and center-of-mass of the wet PTM (starting from the measured dry weight and center-of-mass) with the measured values would demonstrate that the liquids can be analytically added to the dry spacecraft, making the measurement of a fueled spacecraft unnecessary.

The test set-up for measuring spacecraft weight and x-y center of mass is shown in Fig. 1. The assembled

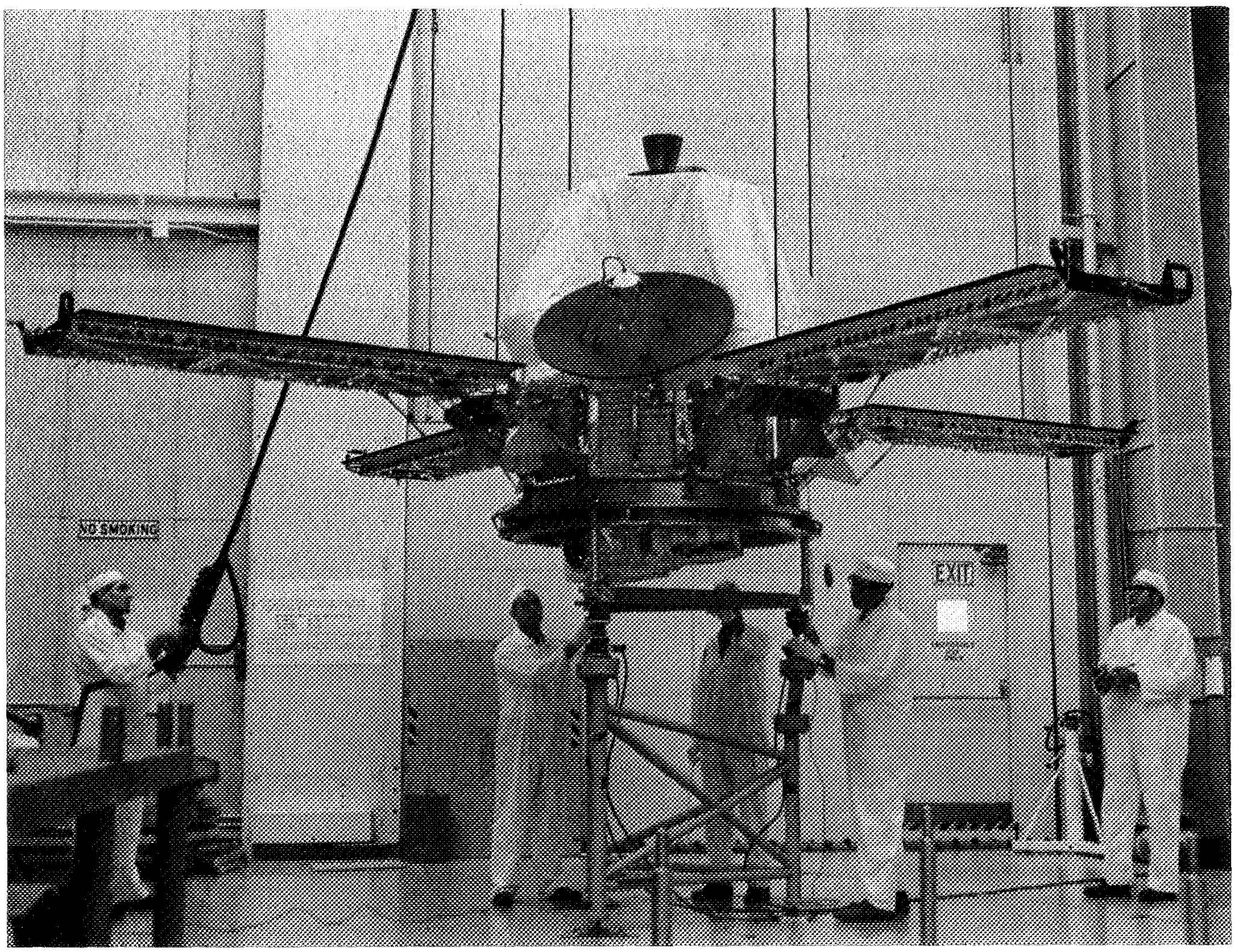

Fig. 1. *Mariner* Mars 1971 weight and center-of-mass test

spacecraft mounted on its support ring is attached to a fixture which adapts to the three-point center-of-mass test stand. Three Baldwin-Lima-Hamilton C3P1 load cells (1000-lb capacity) are used as forced transducers. The load cells are mounted on horizontal bearing plates, so that they are free to move horizontally. They are positioned accurately by the center-of-mass adapter through a cup-and-ball arrangement. The measurements are made in each of the three possible 120-deg-spaced positions. This eliminates errors in center-of-mass should the center-of-mass stand be slightly out-of-level, or should any load cell be slightly in error. The support ring center-of-mass is eliminated from the equations (used to reduce the data) by repeating the sequence of three weighings with the spacecraft rotated 180 deg relative to the adapter. The weighing operations require approximately 4 h.

A simple error analysis indicated that the accuracy of the measurements is approximately ±3 lb in weight and ±0.040 in. in x and y. Because the measurements are made in air, a correction for buoyancy is required: 1.91 lb, of which 1.41 lb is due to propulsion subsystem tankage.

5. Results

A comparison between measured and calculated values is given in Table 1. The dry spacecraft values assume no propellants, pressurants, or attitude-control gas.

Table 1. Measured and calculated values

	Weight, lb	x, in.	y, in.
Dry Spacecraft			
Calculated	1115.3	−0.110	0.220
Measured	1114.4	−0.182	0.068
Difference	0.9	0.072	0.152
Wet Spacecraft			
Calculated	2175.0	1.697	−1.755
Measured	2172.2	1.701	−1.755
Difference	2.8	−0.004	0.000

The desired accuracy requirements for weight W, x and y are:

$$\left|\frac{\Delta W}{W}\right| < 0.0025$$

$$(\Delta x)^2 + (\Delta y)^2 < 0.01 \text{ in.}^2$$

where ΔW, Δx and Δy are the uncertainties in W, x and y. Since the measured values of x and y are within 0.040 in. of the correct values, the above calculated x and y fall slightly outside the specification. While this was a disappointment, no refinement of the calculations was made for two reasons: the better measured values were available, and the calculations were adequate for the remaining properties, whose accuracy requirements were less.

I. Structure and Dynamics Test and Analysis,

Applied Mechanics Section

1. Electronic Analog Simulation

Dynamic test implementation problems encountered during forced vibration testing of the *Mariner* Mars 1971 propulsion module necessitated an evaluation of the capability of the peak select acceleration control system. One phase of this evaluation was done with the aid of an analog computer which simulated the dynamic characteristics of the propulsion module and vibration exciter and the vibration exciter and amplifier electrical characteristics. The dynamic characteristics of the primary propulsion system (PSS) structure were represented by twelve normal modes obtained from digital computer analysis. The dynamics of the vibration exciter, i.e., the armature flexures and trunnions, were obtained experimentally by accomplishing a modal survey of the system supporting a dummy structure of known inertial properties. Electrical characteristics of the vibration exciter and amplifier system were obtained from the manufacturer. The peak select acceleration control unit was connected directly to the analog simulation, as shown in Fig. 1, using the actual sweep oscillator and servo-control system. This configuration of analog simulation of the structure and vibration exciter test and control equipment provided the capability of varying test parameters, such as structural damping, structural shaker frequencies, sweep rate, compressor speeds and others, and evaluating the effects of these parameter changes on the peak select control unit in real-time.

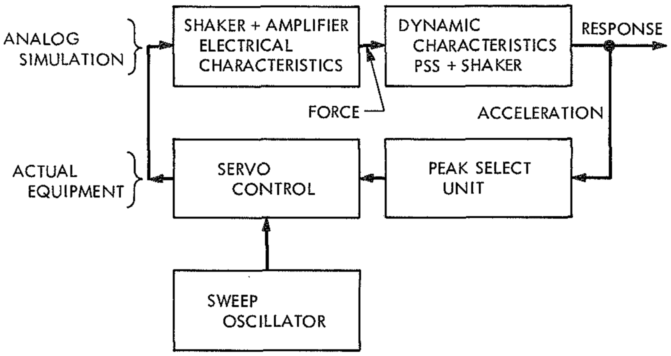

Fig. 1. Block diagram of analog and test equipment

Eight control accelerometers located at the structure-fixture interface and two response control accelerometers located on the two propellant tank hubs as simulated by the analog were used for test control evaluation. Figure 2 is a typical representation of switching between control transducers to maintain a preset amplitude at one or more control points.

Although the exact test conditions of the real test were not completely simulated, the similarity of control switching and slope, i.e., rate of change of correction, were sufficient to evaluate and demonstrate that the control system as used was marginally adequate to satisfy the objectives of the intended test program.

The uniqueness of the evaluation performed was the combination of the real-time analog simulation of the test structure and shaker system with the actual test control system. Many kinds of parametric changes were made using real-time test sweeps without endangering the test structure or shaker system.

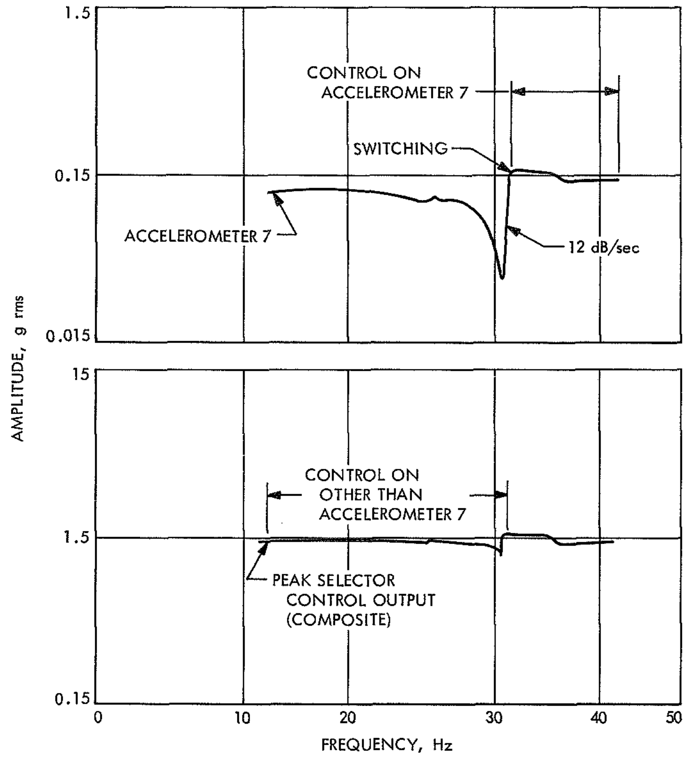

Fig. 2. Comparison of control accelerometer 7 and peak selector output

The ability to make parametric changes to a complicated control system in a timely manner has been demonstrated and should prove to be of value in future flight programs.

J. Codispersion Propellant Expulsion Bladder Evaluation, *Materials Section*

1. Introduction

During early developmental testing of the *Mariner* Mars 1971 propulsion subsystem expulsion bladders a series of failures occurred resulting in substantial changes in both materials, fabrication techniques, and configuration at launch. The bladder is a flexible TFE-FEP Teflon laminate membrane which fits inside a 30-in.-diam titanium propellant tank and is pressurized by nitrogen gas to expel propellants contained within under zero g conditions. It is constructed by spraying Teflon dispersions onto an aluminum mandrel which is leached out chemically after fusion of the laminate layers. The standard laminate bladder was found to be significantly degraded by solvent stress-cracking in Freon TF (used as propellant referee fluid), particularly in a biaxial cyclic stress field. Similar behavior could be predicted for the actual propellant, based upon surface wetting and swelling similarities. Subsequent replacement of the solvent-sensitive FEP Teflon Type T-120 in the laminate with a superior type TE-9511 (higher molecular weight) was a major advancement in reducing solvent sensitivity. Changes in construction of the laminate to a codispersion system were also critical to the success of the bladder redesign (See Fig. 2 in *Subsection G).*

This report summarizes some of the significant test results on the codispersion material derived prior to production of flight bladders of this type.

2. Test Program

Tensile testing of samples from an actual bladder revealed a significant improvement in uniaxial ultimate strength values (Table 1). Testing of samples immersed in actual propellants was accomplished by soaking test samples without load for 165 h in monomethylhydrazine (MMH) or inhibited nitrogen tetroxide (N_2O_4). The samples were removed, wiped dry, and tested within 2 min. Results are shown in Table 2. The N_2O_4 propellant was observed to have a plasticizing effect on Teflon (lower apparent modulus). This is unlikely to affect performance in this application.

Measurement of fluid linear swelling effects on the codispersion material was conducted by optical determination of length change of laminate strips in glass holding fixtures immersed in propellant and referee fluids for various times up to 303 h. This information is important to sizing bladders for fitting tank interior dimensions. The results are presented in Table 3. Both isopropyl alcohol and MMH are shown to have no swelling effect, while N_2O_4 and Freon TF show swelling characteristics at different rates. N_2O_4 swelling stabilizes within 24 h, while Freon TF requires more than 5 days.

Fatigue tests between zero and various tension stresses were performed on codispersion laminate material, revealing that stresses in excess of 3000 psi were necessary to produce failure in air within 1000 cycles. Launching with pressure within the bladders will reduce cyclic stresses to very low levels easily withstood by the codispersion laminate material.

Numerous samples have been studied using thin sections viewed with transmitted polarized light for revealing interlayer characteristics in an effort to understand the behavior of this material in the bladder application. A typical microstructure is shown in Fig. 1. The "balanced" structure obtained is believed to produce lower surface residual stresses in the finished product than standard bladder laminates. Residual stresses result from contraction differences between FEP and TFE Teflon during cooling from the fusion cycles while restrained by the aluminum mandrel. Standard laminates have maximum residual stress on the "outer" FEP surface, while codispersion laminate material appears to confine residual stress from this effect to "interior" interfaces.

Table 1. Bladder material uniaxial ultimate strength values

Type	Yield strength, psi	Ultimate strength, psi	Elongation, %
Codispersion laminate (typical values)	1860	4430	450
Standard laminate (typical values)	1800	3600	425

Table 2. Bladder motor uniaxial ultimate strength values after exposure to propellants

Type	Yield strength, psi	Ultimate strength, psi	Elongation, %
Codispersion laminate in MMH	1830	4800	488
Codispersion laminate in N_2O_4	733	4000	541

Table 3. Fluid linear swelling effects on codispersion bladder material

Liquid	Percent of length change after time lapses				
	14.5 h	42.5 h	62.5 h	138.5 h	303 h
Inhibited N_2O_4	1.57	1.60	1.60	1.60	1.60
Inhibited N_2O_4	1.60	1.60	1.60	1.60	1.60
MMH	0	0	0	0	0
MMH	0	0	0	0	0
Isopropyl alcohol	0	0	0	0	0
Isopropyl alcohol	0	0	0	0	0
Freon 113 (TF)	0.20	0.63	1.22	2.44	2.44
Freon 113 (TF)	0.24	0.83	1.34	2.49	2.49

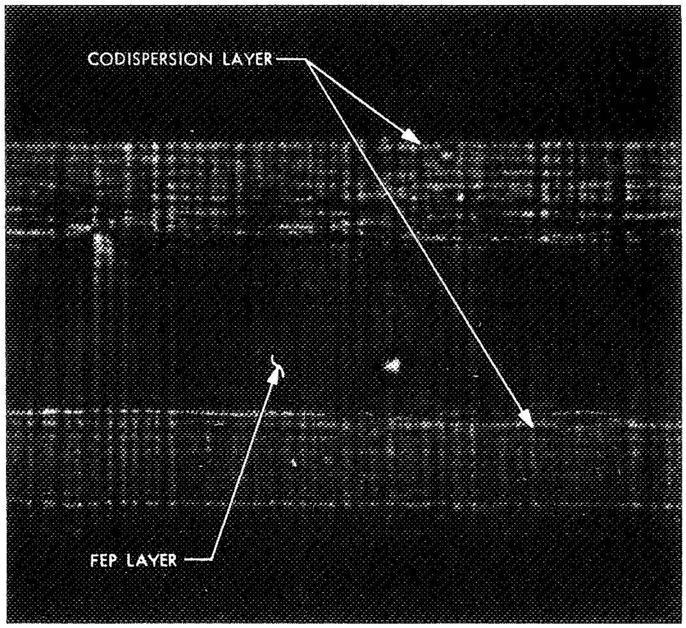

POLARIZED ILLUMINATION
MAGNIFIED 200 X

Fig. 1. Microstructure of new codispersion expulsion bladder material

K. Evaluation of Spacer Rod Material for Narrow-Angle Television Camera, *Materials Section*

1. Introduction

The *Mariner* Mars 1971 narrow-angle television camera employs a spring-loaded spacer system to maintain dimensional requirements between critical optical elements. The spacers are 0.3-in.-diam by 10 in. long, spring-loaded in compression to 6000 psi. The working temperature range is −25 to +35°C (−11 to +95°F). The maximum permissible change in length of the spacer rods is 0.002 in. to maintain the focusing requirements.

To meet the above requirements, a material with a maximum creep rate of 20 μin./in./y when stressed at 6000 psi in compression and a coefficient of expansion of less than $4.0 \times 10^{-7}/°C$ ($2.2 \times 10^{-7}/°F$) in the range of −25 to +35°C (−11 to +95°F) is required. Super Invar was selected because published physical properties data indicated it to have the best promise of meeting the requirements (Refs. 1, 2).

Of concern was the dimensional change associated with a reported (Ref. 2) phase change from face-centered cubic to body-centered cubic at −10°C (+14°F). An increase of nickel content lowers the temperature for the start of this phase change. A Super Invar composition yielding a phase change temperature well below the −25°C (−11°F) working temperature, was considered a requirement to provide a safe margin to avoid such a dimensional change.

2. Material Composition and Verification

Super Invar rod, 0.3-in.-diam, Heat No. J-6055, was procured from Simonds Steel Div. of Wallace-Murray Corp. The material as-received had been annealed at 760°C (1400°F), followed by air cooling. The chemical composition of a heat melt sample, as reported by the manufacturer, is as follows:

C	P	S	Si	Mn	Ni	Cr	Cu	Co	Fe
0.08	0.010	0.005	0.13	0.50	32.38	0.05	0.06	5.11	Balance

Chemical analysis was verified on three separate lengths of rod selected at random.

Metallographic sections were made to determine the grain structure. A typical microstructure is shown in Fig. 1.

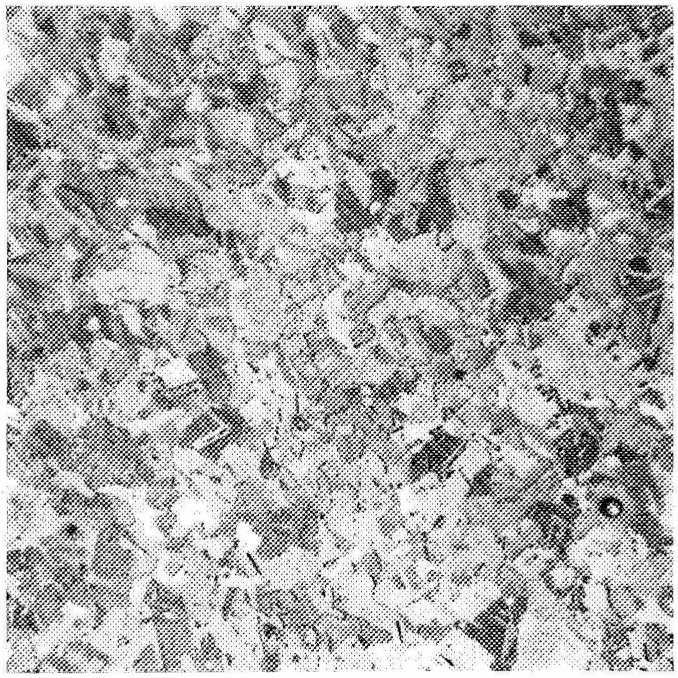

MAGNIFIED 500 X

Fig. 1. Microstructure of Super Invar

3. Test Program

The following tests were made on random samples to verify materials requirements and obtain property data:

Thermal coefficient of expansion (Fig. 2)

Plastic microstrain in compression (Fig. 3)

Compressive microcreep at 6000 psi (Fig. 4)

Tensile yield (0.2% offset) and tensile strength (Table 1)

Knoop microhardness (Table 2)

All specimens were machined and heat-treated according to the following schedule:

(1) 829 to 843°C (1525 to 1550°F) for 1/2 h with H_2O quench.

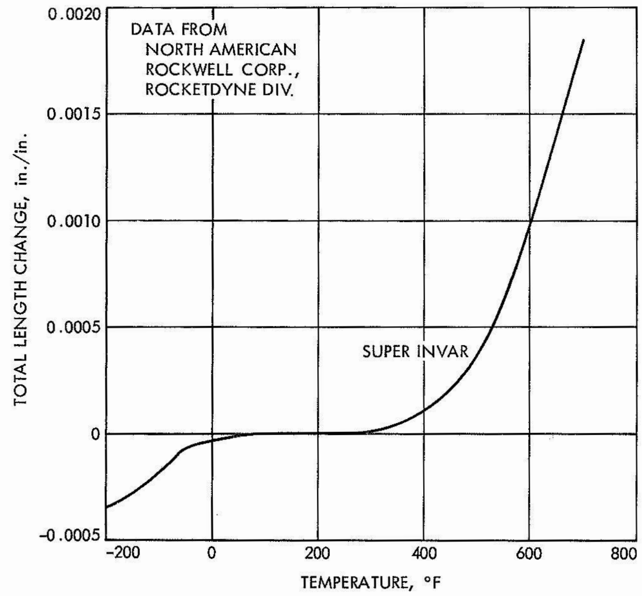

Fig. 2. Thermal expansion properties of Super Invar

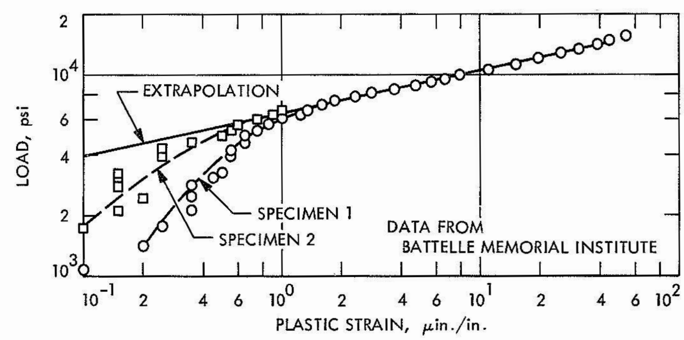

Fig. 3. Compression microstrain data

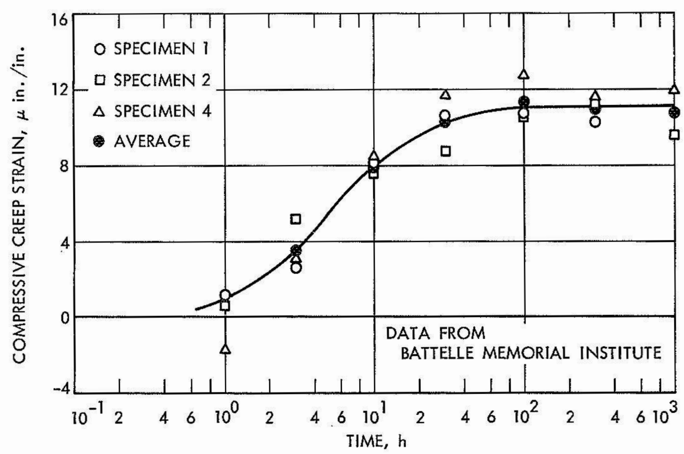

Fig. 4. Compressive microcreep data

(2) Specimens were machined.

(3) 316 ± 5°C (600 ± 10°F) for 1 h and air cooled.

(4) 96 ± 3°C (205 ± 5°F) for 48 h and air cooled.

(5) 189 ± 5°C (375 ± 10°F) for 16 h and air cooled (to simulate application of dry film lubricant to spacer rods).

4. Discussion

A plot of change of length versus temperature (Fig. 2) shows linear expansion in the ranges −45 to +21°C (−50 to +70°F) and +21 to +125°C (+70 to +275°F) with coefficients of expansion of 8.8×10^{-7}/°C (4.9×10^{-7}/°F) and zero, respectively. The change of length over the working temperature range of −25 to +35°C (−11 to +95°F) is 0.000040 in./in., which corresponds to a coefficient of expansion of 6.7×10^{-7}/°C (3.7×10^{-7}/°F). The phase change shown in Fig. 2 at −45°C (−50°F) is well below the working temperature of −25°C (−11°F) and, therefore, is not relevant to the application as a television camera spacer rod.

The microyield strength (stress to produce 10^{-6} plastic strain) was found to be 6000 and 6600 psi for two specimens tested (Fig. 3). The logarithmic plot of stress versus plastic strain is linear for strains above 10^{-6}, but concave downward for lesser strains. Microcreep under compressive stresses of 6000 psi for up to 1000 h showed initial rates of approximately 0.8×10^{-6}/h (Fig. 4). After approximately 30 h and a total strain of approximately 11×10^{-6}, microcreep ceased. The nonlinearity of the logarithmic stress–plastic strain data and the transient behavior of the creep data are believed to be related to the residual stresses contained in the machined surface layers of the specimens.

Tensile yield and ultimate strength data (Table 1) indicate good uniformity of strength properties in the randomly selected specimens. The largest variations in average tensile yield and tensile ultimate values were 5.5 and 4.5%, respectively. The values correlate with data given in Ref. 1.

The Knoop microhardness tests made on randomly selected specimens (Table 2), show good material uniformity throughout the specimen cross sections. The microstructural examinations of the rods showed the uniform fine-grained structure desirable for this material.

All the data indicate that the Super Invar material is satisfactory for the intended application as spacer rods. Microcreep is well within design requirements for the

Table 1. Tensile properties of Super Invar rods

Sample No.	Tensile yield strength (0.2% offset)		Tensile ultimate strength		Elongation at failure		Number of specimens
	Average, ksi	Range, ksi	Average, ksi	Range, ksi	Average percent	Range percent	
1B	55.0	54.6–55.3	80.6	80.1–81.0	40	39–41	3
2B	54.2	53.6–54.6	79.0	78.8–79.1	41	39–42	3
3B	55.4	55.0–56.0	80.1	79.1–80.8	44	41–48	3
4B	54.0	53.9–54.1	80.0	79.6–80.3	44	44–45	3
5B	54.5	53.7–55.2	79.8	79.1–80.3	41	39–42	3
6B	54.3	53.7–55.2	79.4	78.4–80.1	41	41–42	3
7B	53.3	52.9–53.6	79.6	78.6–80.1	41	41–42	3
8B	53.0	52.9–53.2	78.3	78.1–78.4	43	42–44	3
9B	54.3	53.8–55.0	80.2	79.8–80.6	43	41–44	3
10B	52.5	51.8–53.6	77.1	76.1–78.6	40	39–42	3
Average	54.0	51.8–56.0	79.4	76.1–81.0	42	39–48	

Table 2. Knoop microhardness of Super Invar rods[a]

Specimen No.	Distance from edge, in.	Knoop hardness No.
1B	0.001	155.2 (average of two specimens)
	0.002	192.4
	0.003	204.0
	0.004	190.2
	0.005	209.0
	0.006	211.6
	0.007	209.0
	0.008	199.2
	0.009	199.2
	0.150	186.7 (average of five specimens)
8A	0.150	187.7 (average of five specimens)

[a]100-g load, 40 X objective lens.

specific *Mariner* Mars 1971 TV use. Coefficient of expansion is very low (although slightly higher than the optimum requirement) over the entire working temperature range and is actually zero in the range of +21 to +135°C (+70 to +275°F). The phase change at approximately −45°C (−50°F) provides a safe margin well below the working temperature range of the camera.

References

1. *Mechanical and Physical Properties of Invar and Invar-Type Alloys,* Defense Metals Information Center Memorandum 207, Battelle Memorial Institute, August 31, 1965.

2. Scott, H., "Expansion Properties of Low-Expansion Fe-Ni-Co Alloys," *Trans. AIME,* Inst. Metal Div., Vol. 89, pp. 506–537, 1930.

II. *Mariner* Venus—Mercury 1973 Project

A. Project Description

The *Mariner* Venus–Mercury 1973 Project was authorized in December 1969. The primary objective of this first dual-planet mission is to conduct exploratory investigations of the planet Mercury's environment, atmosphere, surface, and body characteristics, and to obtain environmental and atmospheric data on the planet Venus (first priority assigned to Mercury investigations). The secondary objectives are to perform interplanetary experiments enroute to Mercury, and to obtain experience with the gravity-assist mission mode.

A single *Mariner* spacecraft is planned for launch by an *Atlas/Centaur* vehicle from Cape Kennedy in October 1973. The Venus encounter, in February 1974, will provide both an opportunity to obtain scientific data at that planet and the necessary energy, by means of gravity-assist, to reach Mercury some 7 wks later. The spacecraft design is expected to resemble that used in the *Mariner* Mars 1969 mission and that being developed for the *Mariner* Mars 1971 mission, with appropriate modifications defined by the Venus–Mercury mission requirements. The scientific experiments, which include television and other planet-oriented elements together with interplanetary fields-and-particles investigations, were selected by NASA Headquarters during July 1970. These experiments are listed in Table 1, along with the corresponding Principal Investigators and Science Team Leaders. The Deep Space Network and other NASA facilities will be committed to support the mission. It is planned that a System Contractor will be selected in early 1971. The Contractor's effort would encompass the spacecraft detail engineering, system assembly, test and operations, and selected support to other elements of the Project.

Table 1. Experiments and principal investigators

Experiment	Principal Investigator	Affiliation
Celestial Mechanics–Radio Science	H. T. Howard[a]	Stanford University
Charged-Particle Telescope	J. A. Simpson	University of Chicago
Infrared Radiometer	S. C. Chase	Santa Barbara Research Corp.
Magnetic Fields	N. F. Ness	Goddard Space Flight Center
Plasma Science	H. S. Bridge	Massachusetts Institute of Technology
Television Science	B. C. Murray[a]	California Institute of Technology
Ultraviolet Spectroscopy	A. L. Broadfoot	Kitt Peak National Observatory

[a]Science Team Leader.

B. Imaging Experiment, *Space Photography Section*

1. Introduction

The objectives of the imaging experiment are to: map and identify the major physiographic provinces of Mercury on the basis of topographic forms and optical properties of surface materials; determine the similarities and differences between the major surface features of Mercury and those on the earth, the moon, and Mars, with special emphasis on the recognition of endogenic structures; determine the distribution of surface features with reference to the dynamic axes of Mercury and investigate the boundaries with surrounding terrain; and establish correlations with earth-based observations. For the planet Venus close-up photography will produce additional spectral, radio emission, and radio occultation observations.

2. Exploration of Mercury

a. Morphology of local features. Topographic and size distribution of craters will be investigated for age implications and comparisons with slopes and shapes of lunar craters. Search will be made for evidence of nonlunar processes, latitudinal and longitudinal topographic variations, impact features, topographic forms with possible implications of unusual endogenic phenomena, and possible nonlunar and non-Martian features.

b. Cartography and geodesy. In conjunction with earth-based radar data and radio occultation data from the spacecraft, the television data will determine whether or not the planet departs significantly from a spherical shape. Also, the orientation of the spin axis of the planet will be determined with greater precision than currently possible from earth. These results combined with images of the surface features will be used to establish a coordinate system and to produce a map.

c. Photometric properties of local features. Rayed craters and other phenomena showing different albedos and photometric functions from surrounding areas will be searched. Attention will be given to the possibility of an exogenic darkening process and its effect on the optical properties of Mercury, the moon, and the Galilean satellites. The morning terminator will be searched for evidences of transitory frosts and the evening terminator for evidence of fluorescence. Attempts to establish correlations with earth-based radar observations will be made.

d. Regional color differences. Search will be made for regional color differences like those of the lunar maria. Such measurements for Mercury are practically impossible from the earth; a flyby may be able to detect them.

e. Polarization properties of local features. Search will be made to locate any areas of unusually large polarization or those that have albedo-polarization values outside the lunar field.

3. Exploration of Venus

Flyby imagery will attempt to make contributions in the following categories:

a. Clouds. Form and time-dependent properties of the ultraviolet clouds will be investigated. Both vertical structure (from limb and, if possible, cusp observations) and horizontal structure will be considered. It is important to locate the altitude of the ultraviolet markings and to ascertain their relationship to the visible clouds and their lifetimes and velocity relative to the planet. High-resolution overlapping terminator imagery of the main clouds will be investigated as an indicator of their nature and structure. This latter study may have important input to such questions as:

(1) Are the clouds composed of windblown surface particles or atmospheric products?

(2) Are there breaks in the clouds revealing multiple cloud layers?

(3) Are there any cloud manifestations of the infrared emission anomaly near the South Pole or the permanent radar features of the surface?

b. Atmospheric circulation. General characteristics of the atmospheric circulation will be investigated from motion of UV markings, and possibly by inference from large and small scale cloud patterns observable in other spectral regions at higher surface resolution than obtainable from earth.

c. Dark-side optical phenomenon. The possible existence of near ultraviolet and visible airglow emissions (steady or transitory) by imagery of the dark limb in near encounter will be searched.

4. Interplanetary Measurements

Two possibilities are listed here in order that the potentialities of such observations are not ignored in the preliminary design. They would be pursued, if at all, with the camera system designed for Mercury use, but operated in some long-exposure mode. They are:

(1) To search for satellites of Mercury and Venus. (The present earth-based limit for such objects may be subject to improvement because of the difficulties inherent in viewing Venus, and especially Mercury, so close to the direction of the sun).

(2) To search for minor planets near the sun.

5. In-Flight Calibration and Test Observations

In-flight calibration pictures will be obtained during the near-earth, post-Venus, pre-Mercury, and post-Mercury phases of the mission. The objective of these measurements will be to fully characterize the cameras for photometric and colormetric data reduction. In addition, full-disk high-resolution imagery of the earth and moon will be taken for later comparison of similarly acquired pictures of Venus and Mercury. High-resolution imagery of the lunar terminator will be valuable in order to obtain the optimum predicted exposures for the expected large brightness variations near the terminator of Mercury. These pictures will be used for later comparison of crater counts with similar scale and lighting conditions. Therefore, it is highly desirable to launch during the last quarter of lunar phase.

In-flight star photography will be obtained for intensity and geometric system calibrations.

6. Television Subsystem

In support of the visual imaging experiment, JPL will develop the television instrument. This instrument design will be identical to the design developed and used for the *Mariner* Mars 1971 imaging experiment. It consists basically of two separate camera heads, each containing a vidicon image sensor, its attendant electronics, and independent telescopic optical systems with companion shutter and filter mechanisms.

The twin cameras will have identical optics with a field of view of ⅓ by ½ deg with 1500-mm focal lengths. Each camera will be equipped with a filter wheel that can be controlled to provide any one of several filters in the optical path. The wheel can be advanced in several modes, including one step, two steps, or no steps between consecutive pictures by ground command. An automatic mode may be designed for various strategies at Mercury and Venus.

The *Mariner* Mars 1971 television subsystem is a second generation of the camera systems flown on *Mariner VI* and *VII*. The principal changes in subsystem design from the *Mariner VI* and *VII* subsystems are in adapting to the all-digital data storage subsystem for *Mariner* Mars 1971, increased flexibility of shutter control and filter selection to adapt to the orbital mission, and minor modifications of the detailed design to increase the instrument reliability.

b. Instrument description. Both cameras have focal-plane shutters like those used on the *Mariner* Mars 1971 television cameras. After passing through the filter and shutter, the optical image is focused onto a slow-scan vidicon. Vidicon electron beam focus, alignment, and vertical and horizontal deflection are performed magnetically. See Table 1 for some of the significant instrument parameters.

Table 1. Television subsystem functional parameters

Characteristic	Cameras A and B
Focal length	1500 mm
Focal length ratio	f/7 to f/11 (to be determined)
Nominal shutter operation	3 msec to 6 sec
Long-exposure operation	(To be determined)
Angular field of view	0.48 × 0.37 deg
Active vidicon target raster	9.6 × 12.5 mm
Scan lines per frame	700
Frame time	42 sec
Picture elements per line	832
Pixels/frame	582, 400
Bits per picture element	8
Bits/frame	4, 379, 200
Video carrier frequency	28.8 kHz
Video baseband	7.35 kHz
Video sampling frequency	14.7 kHz
Angle subtended by TV line	9 μrad
Nyquist frequency	33 line pairs/mm horizontal 36 line pairs/mm vertical
Overall system resolution (including optics and electronics)	10% Response at 32 lp/mm

The video information is processed by the signal chain which is shown schematically in Fig. 1. It consists of an ac coupled video amplifier containing a fourth-order bandpass filter, a synchronous demodulator, followed by

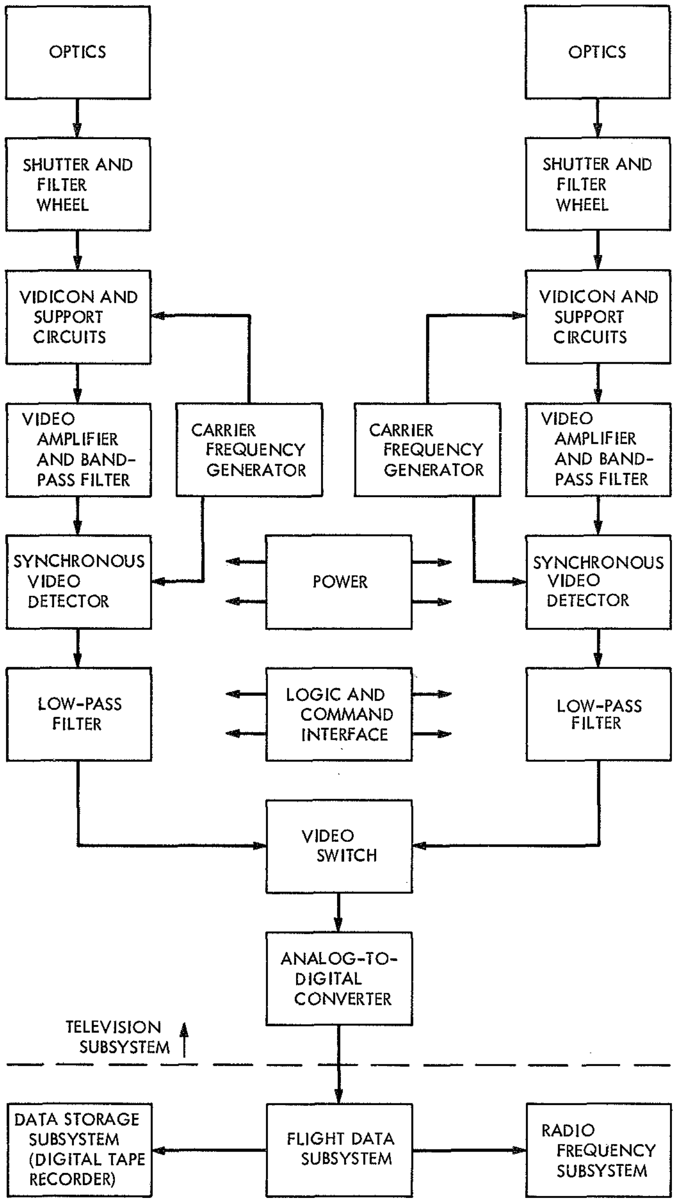

Fig. 1. *Mariner* Venus-Mercury 1973 television subsystem signal flow chart

a fifth-order Butterworth low-pass filter. The video signal from the vidicon is converted to a modulated carrier signal by chopping the vidicon cathode current at the carrier frequency rate. The carrier frequency is 28.8 kHz and is synchronized with the spacecraft power frequency. Some noise rejection is accomplished by phasing the carrier so that the vidicon beam current is off during the switching noise burst generated by the spacecraft primary ac power. The low-pass filter has a bandwidth from dc to 7.35 kHz. The output of this filter is sampled by an 8-bit analog/digital converter at a 14.7-kHz sampling rate which provides a data stream from the TV subsystem of 832 8-bit words for each of the 700 lines comprising one TV frame. The bandpass filter consists of two second-order sections with a bandwidth of 28.8 ± 7.35 kHz.

The first section of the bandpass filter along with the preamplifier and postamplifier are contained in the camera head. Their function is to provide sufficient gain to raise the video signal from a maximum of about 5 nA obtained from the target electrode in the vidicon to a maximum of 5 V at the camera head output. The first section of the bandpass filter provides noise rejection in the camera head by limiting the signal chain bandwidth. The remainder of the video chain is contained within Bay VII of the spacecraft bus. The bus electronics consists of an ac isolation amplifier to provide common mode noise rejection at the input, the second section of the bandpass filter, the synchronous demodulator, low-pass filter, and analog/digital converter.

The digital signal is transmitted to the flight data subsystem (FDS), where it is rate-buffered and formatted. The formatted data is then routed to the digital tape recorder (DTR) in the data storage subsystem (DSS). In addition, it can be routed to the radio subsystem for real-time transmission or to both the DSS for storage and the radio subsystem for simultaneous transmission.

In order to take advantage of the channel capacity available for data transmission at Mercury and Venus, the *Mariner* Venus–Mercury 1973 spacecraft will have the capability of sending back the television data in quasi-real time. The television data will be compressed in the FDS to match the available S-band channel capacity at Mercury encounter.

7. Preliminary Mission Sequence

This preliminary mission sequence is presented below in the chronological order in which it would be carried out. The experimental objectives for each distinct phase are listed for convenience.

a. Observations in the vicinity of the earth–moon system. A limited number of pictures should be taken and read out soon after launch. These early pictures will test the imaging system prior to the critical points in the mission and provide in-flight calibration data on the system. The pictures required during this phase are:

(1) The full disk of the moon for later comparison with pictures of Venus and Mercury.

(2) The full disk of the earth–moon system for similar comparison purposes and for photometric calibration of the system.

(3) A suitable star field for in-flight geometric calibration of the system.

(4) High resolution pictures of the lunar terminator for experience with large brightness gradients.

Ground resolution in these pictures is to be comparable to at least the late far-encounter portion of the Mercury images. The filters will be visible principally; however, checks on the exposure characteristics of the filters will be made.

b. Cruise observations between earth and Venus. The experimental objectives for this phase of the mission are similar to those listed above. Images of the earth and stars will constitute an in-flight calibration of both the television subsystem and the scan platform.

c. Pre-encounter at Venus. There is little chance for successful experiments at far pre-encounter of the mission due to unfavorable viewing of the planet and the necessity for pointing the camera very nearly in the solar direction. At near pre-encounter, the same difficulties still apply, but there may be the possibility of observing airglow on the dark side of the planet. It may also be possible to observe some detail in the twilight cusp. A resolution of 1 to 2 km with a 1000-km field of view is needed. Ultraviolet and visible filters will be used.

d. Encounter at Venus. Many pictures of the terminator should be taken at Venus encounter. These may reveal small-scale structures, both vertical and horizontal, in the visible clouds. Maximum coverage with stereo overlap should be attempted. The resolution will be 1 km or better. A visible filter will be used.

A preliminary detailed sequence at Venus encounter has been designed for mission planning. This sequence takes advantage of the high data rates and full-resolution pictures will be sent back in the real-time mode every 42 sec. A trajectory plot showing the viewing constraints at Venus are illustrated in Fig. 2.

e. Near post-encounter at Venus. A number of pictures of the limb should be taken during this period. These pictures may distinguish UV from visible clouds. These cloud layers may be separated vertically by as much as 40 km. The resolution will be 1 to 2 km; up to 1000-km dimension may be needed. The filters will be ultraviolet, visible, red, and polarizers. The ultraviolet and visible images must overlap in part.

f. Far post-encounter at Venus. A series of pictures of the entire bright disk should be taken during this period. These pictures would be used to study the apparent motion of the ultraviolet cloud layer. The limb and a significant fraction of the disk should be included in these frames as a reference line. The resolution will be better than 250 km at maximum distance. The filters will be ultraviolet, visible, and polarizer.

g. Cruise observations between Venus and Mercury. In addition to a repetition of the in-flight calibration, it may be desirable to attempt a search for undetected satellites of Venus and especially Mercury. Such observations probably would involve long-exposure pictures of the space adjacent to each planet near the plane of the ecliptic.

h. Far pre-encounter at Mercury. Series of pictures beginning with a resolution of 750 km should be taken during this period. These pictures are needed for:

(1) Comparison with earth-based pictures at the same resolution.

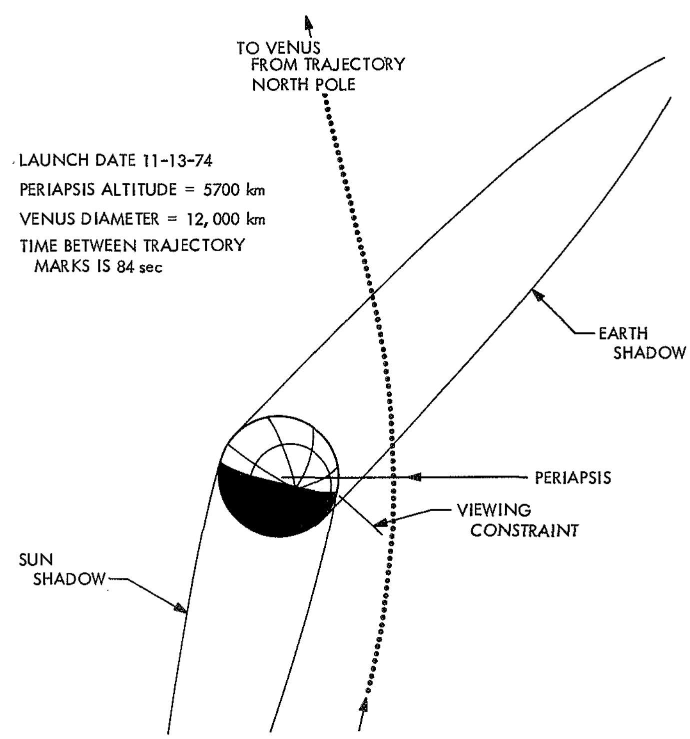

Fig. 2. Viewing constraints of Venus from trajectory North Pole

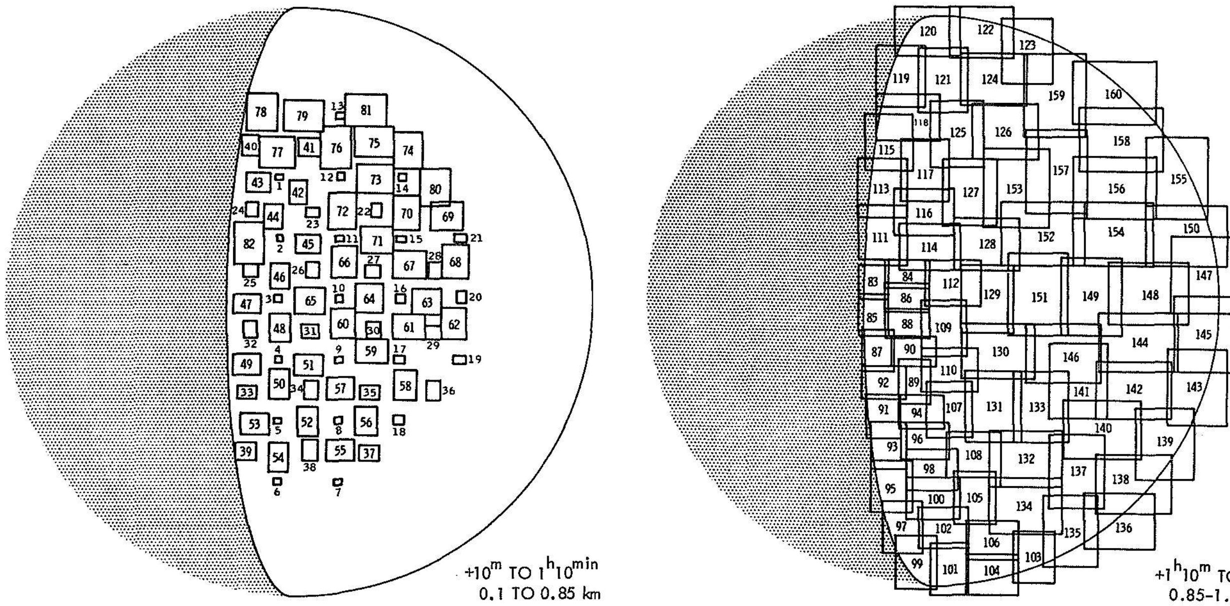

Fig. 3. Typical Mercury sequence (outgoing aspect, one picture every 42 sec)

(2) Determination of spin-axis orientation.

(3) Determination of proper exposure for subsequent pictures.

(4) Coverage of most of the planet's surface area.

The filters will be primarily visible, some red, ultraviolet, and polarizers.

i. Near pre-encounter at Mercury. This is the most important phase of the mission, and the maximum number of pictures should be taken. Maximum coverage at high resolution is needed to reveal small-scale detail on the surface, especially near the terminator. The resolution will be from 10 to 0.1 km; the filters will be primarily visible, some red, ultraviolet, and polarizers.

j. Encounter at Mercury. A preliminary Mercury sequence has been designed for mission planning. This sequence takes advantage of the data compression scheme in the flight data subsystem, which allows complete planet coverage at a surface resolution of 2 to 4 km by mosaicking the pictures. In Fig. 3 the type of coverage possible is illustrated for the data obtained in real-time in this compressed mode on the outgoing trajectory from Mercury. A trajectory plot showing the viewing constraints at Mercury is illustrated in Fig. 4.

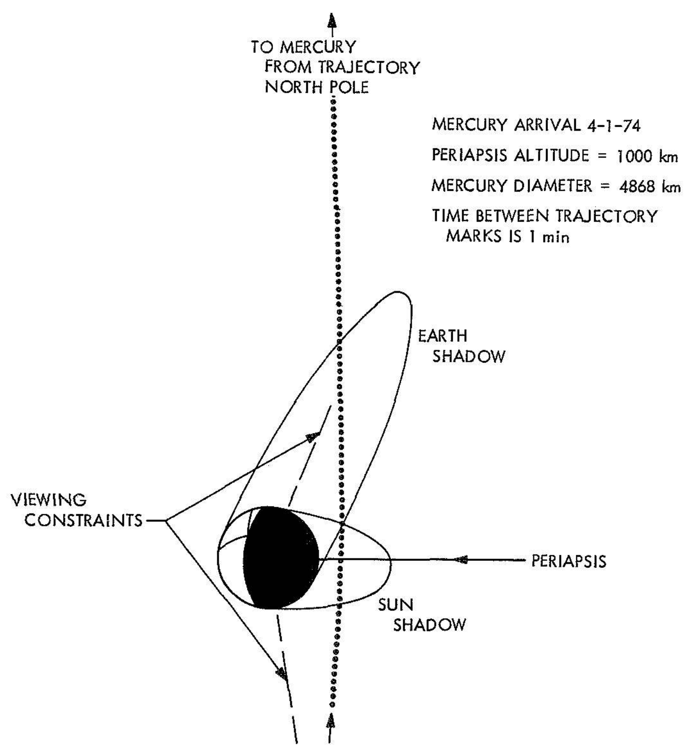

Fig. 4. Viewing constraints of Mercury from trajectory North Pole

k. Near post-encounter at Mercury. The experimental objectives for this part of the mission are identical to those listed for near pre-encounter of Mercury. The only difference is that a new area of the planet will be covered.

l. Far post-encounter at Mercury. The experimental objectives for this part of the mission are identical to those listed for far pre-encounter at Mercury.

m. Post-Mercury cruise observations. The experimental objectives for this part of the mission are similar to those between Venus and Mercury. The geometrical calibration with the star field especially should be repeated. Also, it may be desirable to search for minor planets of the sun at this point, because higher risk spacecraft operations might be possible, such as steering off sun-lock on gyros to provide the extreme cone-angle coverage (for a three-axis stabilized spacecraft).

n. Extended mission. One or two Mercury returns would be extremely beneficial for the imaging experiment by allowing one of the passes to be more nearly optimum for viewing conditions. On a second encounter a polar pass (near the terminator) trajectory would be desirable such that the spacecraft passing distance is no less than 5000 km (in order to obtain photos without smear). On the basis of examining the first set of TV pictures, it is possible that a decision to return to the same point would be made to examine observed features or ambiguities. Furthermore, this return would permit some detailed high-resolution stereo or color pictures to be made on areas suggested by interpretation of the first set of pictures. Any overlap of pictures from two encounters will provide an accurate spin period measurement. The third Mercury encounter could possibly be a polar pass over the opposite pole, i.e., the second Mercury return over the north pole and the third Mercury return over the South Pole.

C. Error Rates for Data Words Time Multiplexed Onto 6-Bit Block-Coded Words, *Spacecraft Telecommunications Systems Section*

1. Introduction

The *Mariner* Mars 1971, *Mariner* Venus–Mercury 1973, and *Viking* (1975) spacecraft communications systems will all have plans to use science data words whose lengths are different from the 6-bit block coded words which will be transmitted over the spacecraft-to-earth communication links received with the multi-mission telemetry system of the DSN. An analysis is presented which shows the error rate for the data words of various word lengths when the error rate for 6-bit coded words is known. No attempt is made to evaluate the gain or loss in information due to quantizing analog data into longer data words having a higher word error rate.

The science words of length M bits are assumed to be serially time multiplexed into 6-bit words. These 6-bit words are mapped into (32,6) biorthogonal coded words and transmitted from the spacecraft to earth. The 6-bit coded words are received, block decoded, and then the science words are decommutated from the received serial bit stream.

2. Mathematical Model

Consider the situation where two or more code words overlap one data word, as in Fig. 1. We define the following events:

α_k = a bit error occurs in at least one of the last k bits of a code word

β_ℓ = a bit error occurs in at least one of the first ℓ bits of a code word

μ = the first overlapping code word is in error

η = the second overlapping code word is in error

γ = a third overlapping code word is in error

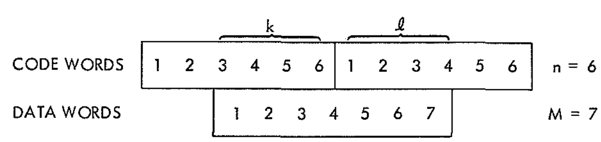

Fig. 1. Case where one 7-bit data word is overlapped by two 6-bit code words

$X(k, \ell)$ = an error occurs in a data word overlapped by k bits of the first code word and ℓ bits of the second.

$X(k, n, \ell)$ = an error occurs in a data word overlapped by k bits of the first code word, an entire n-bit code word, and ℓ bits of the third code word.

Let the probability of an event occurring be denoted by $p(\cdot)$. Then

$$p(x) = p(\alpha_k) + p(\beta_\ell) - p(\alpha_k \cap \beta_\ell) \quad (1)$$

is the probability of error when two code words overlap one data word. Similarly, if three code words n bits long overlap a single data word, then

$$p(x) = p(\alpha_k) + p(\alpha_n) + p(\beta_\ell) - p(\alpha_k \cap \alpha_n) - p(\alpha_k \cap \beta_\ell) - p(\alpha_n \cap \beta_\ell) + p(\alpha_k \cap \alpha_n \cap \beta_\ell) \quad (2)$$

Next, we assume that the presence or absence of an error in one code word is statistically independent from the presence or absence of an error in any other code word. Then

$$p(\alpha_k) = p(\alpha_k|\mu)\, p(\mu) \quad (3)$$

$$p(\beta_\ell) = p(\beta_\ell|\eta)\, p(\eta) \quad (4)$$

$$p(\alpha_k \cap \beta_\ell) = p(\alpha_k)\, p(\beta_\ell) \quad (5)$$

Define ϵ_c as the word error rate of the code words. If ϵ_c is independent of time, then

$$p(\mu) = p(\eta) = \epsilon_c \quad (6)$$

Thus

$$p(x) = \left[p(\alpha_k|\mu) + p(\beta_\ell|\eta)\right] \epsilon_c - \left[p(\alpha_k|\mu)\, p(\beta_\ell|\eta)\right] \epsilon_c^2 \quad (7)$$

when two code words overlap, or

$$p(x) = \left[p(\alpha_k|\mu) + p(\alpha_n|\eta) + p(\beta_\ell|\gamma)\right] \epsilon_c - \left[p(\alpha_k|\mu)\, p(\alpha_n|\eta) + p(\alpha_k|\mu)\, p(\beta_\ell|\gamma) + p(\alpha_n|\eta)\, p(\beta_\ell|\gamma)\right] \epsilon_c^2 + p(\alpha_k|\mu)\, p(\alpha_n|\mu)\, p(\beta_\ell|\gamma)\, \epsilon_c^3 \quad (8)$$

when three code words overlap.

3. Conditional Probabilities

In a (32,6) biorthogonally coded word, up to 7 symbol errors can be made in the code word, and the decoder will still decode the transmitted word. If 8 symbol errors occur, correct detection is uncertain. If 9 to 25 symbol errors are made, the decoder will equally likely map the transmitted word into any of the remaining words in the dictionary except the conjugate of the transmitted word. If more than 25 symbol errors are made, the transmitted word will be mapped into its conjugate. We now make the following approximation: Given that a word error occurs, the transmitted word will equally likely be mapped into any of the remaining words in the dictionary *except* its conjugate.

We are now in a position to construct the conditional probabilities of *Subsection 2*.

Let q_r^n = probability that r successive bits in n bits are all correct, given that the n bit word is in error. Now, there are $2^n/2^r$ words with r specific bits the same in a dictionary of 2^n possible words. The transmitted word can map into $[2^{(n-r)} - 1]$ words having r specific bits the same. There are $(2^n - 2)$ words in the dictionary less the transmitted word and its conjugate. Thus,

$$q_r^n = \frac{2^{(n-r)} - 1}{2^n - 2} \quad (9)$$

For a 6-bit code word,

$$q_r^6 = \frac{\frac{64}{2^r} - 1}{62}$$

Let p_r^n = probability that at least one of r successive bits in n bits is in error, given that the n bit word is in error.

Then

$$p_r^n = 1 - q_r^n \quad (10)$$

Thus

$$p(\alpha_k|\mu) = p_k^n \quad (11)$$

$$p(\beta_\ell|\eta) = p(\beta_\ell|\gamma) = p_\ell^n \quad (12)$$

Table 1 lists p_r^6 for $1 \leq r \leq 6$.

4. Synchronization of Code Words and Data Words

When a data word is mapped onto a code word, there are 6-bit positions of the code word at which the data word may begin. The synchronization chart of Fig. 2 shows these six positions, and labels them A through F. Now a data word M bits long will be mapped in a specific way onto a 6-bit coded word. How the data word is mapped depends on its initial state of synchronization with the code word. For instance, when $M = 2$, there are two unique ways to synchronize. As shown in Fig. 2, either three 2-bit data words are completely contained in one coded word, or 2 data words overlap a coded word, and two are imbedded in the coded word. Figure 2 shows all of the possible sync schemes for mapping M bit data words ($1 \leq M \leq 12$) into 6-bit coded words. The sync cycles are identified by the bit starting positions of the data words.

It should be noted that for those words with more than one unique sync position, that once a serial data stream starts mapping into code words, a sync position will be established and will remain in that sync sequence until the data stream is interrupted, as long as the data word length remains constant. If the data word length of interest changes in the data stream, the mapping of M bit data words onto N bit code words may become asynchronous.

5. Data Word Error Probabilities

Once a synchronization scheme for mapping an M bit data word onto an N-bit coded word is established, the probability of data word error is uniquely determined by the probability of coded word error. Using the notation of *Subsections* 2 and 3, the probability of a data word error can be computed from Eqs. 7, 8, 11, and 12.

As an example, consider the case when $M = 3$. There are three possible sync schemes. The data words either repeat in bit positions ADADAD . . . , BEBEBE . . . , or

Table 1. Conditional probability of an error somewhere in r specific bits given an error in a 6-bit word

r	p^6_r
1	31/62
2	47/62
3	55/62
4	59/62
5	61/62
6	1

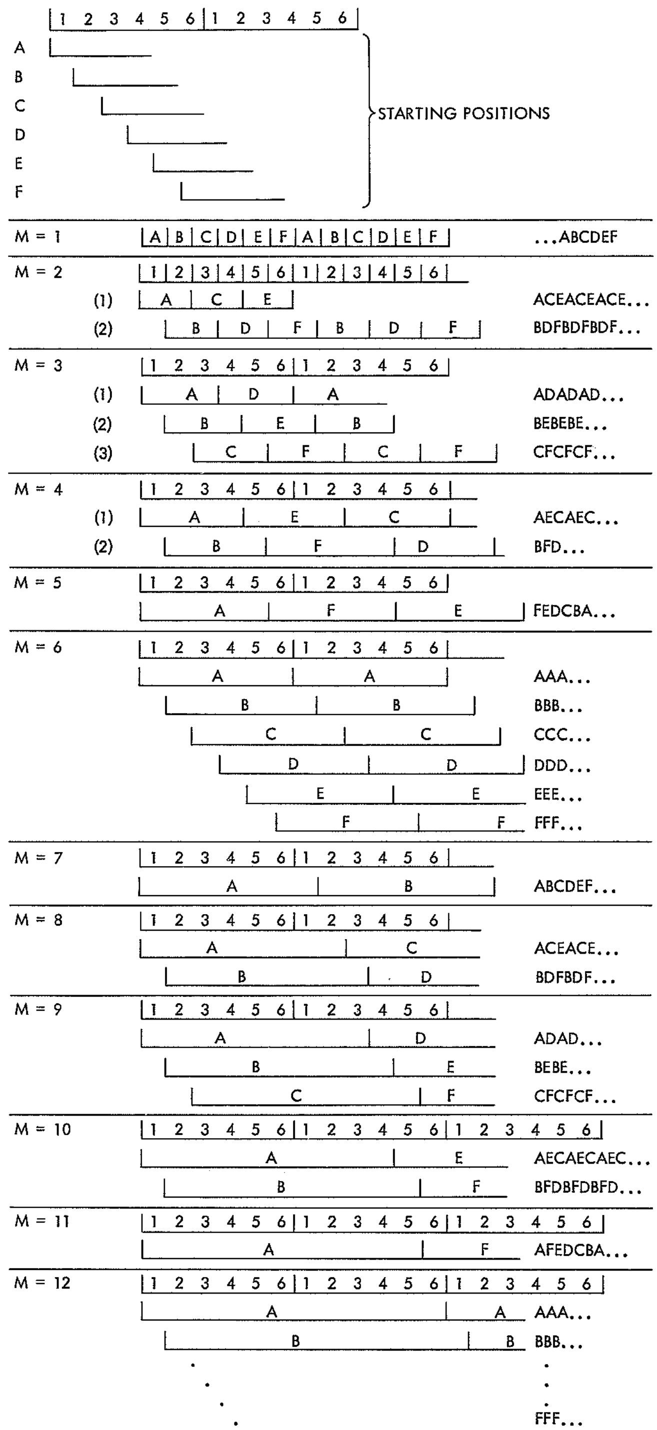

Fig. 2. Synchronization chart

CFCFCF . . . . When the 3-bit data word is in bit position A, its probability of error is given by $p^6_3 \epsilon_c$. When the data word is in bit position D, its probability of error is also $p^6_3 \epsilon_c$. A and D occur equally often, so the probability of error for ADAD . . . is $\epsilon_D = p^6_3 \epsilon_c$.

Table 2. Error probability chart[a]

M	Sync	Error rate, ϵ_D
1	1	$p_1\epsilon_c$
2	1	$p_2\epsilon_c$
	2	$1/3\ p_1\epsilon_c + 2/3\ \{2p_1\epsilon_c - (p_1\epsilon_c)^2\} = 5/3\ p_1\epsilon_c - 2/3\ (p_1\epsilon_c)^2$
3	1	$p_3\epsilon_c$
	2	$1/2\ p_3\epsilon_c + 1/2\ [p_1\epsilon_c + p_2\epsilon_c - p_1p_2\epsilon_c^2]$
	3	Same as sync 2
4	1	$2/3\ p_4\epsilon_c + 1/3\ [2p_2\epsilon_c - (p_2\epsilon)^2]$
	2	$1/3\ p_4\epsilon_c + 2/3\ [p_3\epsilon_c + p_1\epsilon_c - p_3p_1\epsilon_c^2]$
5	1	$1/3\ p_5\epsilon_c + 1/3\ [p_4\epsilon_c + p_1\epsilon_c - p_4p_1\epsilon_c^2] + 1/3\ [p_3\epsilon_c + p_2\epsilon_c - p_3p_2\epsilon_c^2]$
6	1	$p_6\epsilon_c$
	2	$p_5\epsilon_c + p_1\epsilon_c - p_5p_1\epsilon_c^2$
	3	$p_4\epsilon_c + p_2\epsilon_c - p_4p_2\epsilon_c^2$
	4	$2p_3\epsilon_c - (p_3\epsilon_c)^2$
	5	Same as sync 3
	6	Same as sync 2
7	1	$1/3\ [p_6\epsilon_c + p_1\epsilon_c - p_6p_1\epsilon_c^2] + 1/3\ [p_5\epsilon_c + p_2\epsilon_c - p_5p_2\epsilon_c^2] + 1/3\ [p_4\epsilon + p_3\epsilon - p_4p_3\epsilon_c^2]$
8	1	$2/3\ [p_6\epsilon_c + p_2\epsilon_c - p_6p_2\epsilon_c^2] + 1/3\ [2p_3\epsilon_c - (p_3\epsilon_c)^2]$
	2	$1/3\ [2p_4\epsilon_c - (p_4\epsilon_c)^2] + 1/3\ [p_3\epsilon_c + p_5\epsilon_c - p_3p_5\epsilon_c^2]$ $+ 1/3\ [2\ (p_1\epsilon_c) + p_6\epsilon_c - 2p_1p_6\epsilon_c^2 - (p_1\epsilon_c)^2 + (p_1)^2\ p_6\epsilon_c^3]$
9	1	$p_6\epsilon_c + p_3\epsilon_c - p_6p_3\epsilon_c^2$
	2	$1/2\ [p_5\epsilon_c + p_4\epsilon_c - p_5p_4\epsilon_c^2] + 1/2\ [p_2\epsilon_c + p_6\epsilon_c + p_1\epsilon_c - p_2p_6\epsilon_c - p_2p_6\epsilon_c^2 - p_2p_1\epsilon_c + p_1p_2p_6\epsilon_c^3]$
	3	Same as sync 2
10	1	$2/3\ [p_6\epsilon_c + p_4\epsilon_c - p_6p_4\epsilon_c^2] + 1/3\ [2p_2\epsilon_c + p_6\epsilon_c - 2p_2p_6\epsilon_c^2 - (p_2\epsilon_c)^2 + (p_2)^2\ p_6\epsilon_c^3]$
	2	$1/3\ [2p_5\epsilon_c - (p_5\epsilon_c)^2] + 2/3\ [p_3\epsilon_c + p_6\epsilon_c + p_1\epsilon_c - p_3p_6\ \epsilon_c^2 - p_3p_1\epsilon_c^2 - p_6p_1\epsilon_c^2 + p_3p_6p_1\epsilon_c^3]$
11	1	$1/3\ [p_6\epsilon_c + p_5\epsilon_c - p_6p_5\epsilon_c^2] + 1/3\ [(p_4 + p_6 + p_1)\ \epsilon_c$ $- (p_4p_6 + p_4p_1 + p_6p_1)\ \epsilon_c^2 + p_4p_6p_1\epsilon_c^3] + 1/3\ [(p_3 + p_6 + p_2)\ \epsilon_c - (p_3p_6 + p_3p_2 + p_6p_2)\ \epsilon_c^2 + p_3p_6p_2\epsilon_c^3]$
12	1	$2p_6\epsilon_c - (p_6\epsilon_c)^2$
	2	$(p_5 + p_6 + p_1)\ \epsilon_c - (p_5p_6 + p_5p_1 - p_1p_6)\ \epsilon_c^2 + p_5p_6p_1\epsilon_c^3$
	3	$(p_4 + p_6 + p_2)\ \epsilon_c - (p_4p_6 + p_4p_2 + p_6p_2)\ \epsilon_c^2 + p_4p_6p_2\epsilon_c^3$
	4	$(2p_3 + p_6)\ \epsilon_c - [2p_3p_6 + (p_3)^2]\ \epsilon_c^2 + (p_3)^2\ p_6\epsilon_c^3$
	5	Same as sync 3
	6	Same as sync 2

[a]Coded word length m is equal to 6 throughout, so the superscript 6 is implied in the notation p^r.

When the 3-bit data word is in sync position BEBE . . . , the error probability is different from the first case. When the data word starts in position B, the error probability is p_3^6. However, when in position E, the data word overlaps two 6-bit coded words, and the error rate is computed from Eq. (7). Thus, the error probability of a 3-bit data word in bit position E is

$$p_1^6 \epsilon_c + p_2^6 \epsilon_c - p_1^6 p_2^6 \epsilon_c^2$$

Since positions B and E occur equally likely in the sequence BEBEBE . . . , the probability of data word error is given by

$$\epsilon_D = \tfrac{1}{2}\, p_3^6 \epsilon_c + \tfrac{1}{2} \left(p_1^6 \epsilon_c + p_2^6 \epsilon_c - p_1^6 p_2^6 \epsilon_c^2\right)$$

The third sync sequence, CFCF . . . , can be shown to have the same error rate as BEBE . . . . If a synchronization is established, the error rate will be that of one of the three possible schemes. If the data words are asynchronous, the error rate for a given word length is some average of the error rates for the possible sync schemes.

Table 2 is an error probability chart. It shows the data word error rate when the code words are 6 bits long and the data words are M bits long ($1 \leq M \leq 12$) for all possible sync schemes shown on in Fig. 2.

6. Effect on Communication Performance

The results of *Subsection 5* are presented in the graph of Fig. 3. This graph shows the relative word error rate, $\epsilon = \epsilon_D/\epsilon_c$, when the coded word length is 6 bits and the data word length is M bits. This graph shows clearly how for a given M, one sync scheme will yield superior performance over other possible schemes. The graph also shows how much additional signal energy per bit is required to improve the science data word error rate so that it is equal to the 6-bit coded word error rate previously required of the communication channel.

Figure 3 does not illustrate the loss in data accuracy due to quantization error as the word length is reduced. This report is limited to illustrating the relation of word error rates for different word lengths and synchronization points, when the basic system block codes words which are 6 bits long.

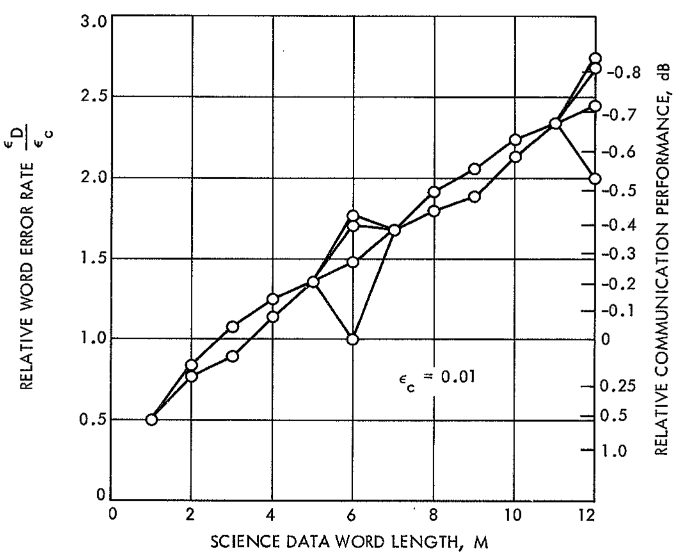

Fig. 3. Science word error rate performance

III. *Viking* Project, Orbiter System and Project Support

A. Project Description and Status

1. Description

The primary objective of the *Viking* Project is to significantly advance the knowledge of the planet Mars by direct measurements in the atmosphere and on the surface and by observations of the planet during approach and from orbit. Particular emphasis will be placed on obtaining information concerning biological, chemical, and environmental factors relevant to the existence of life on the planet at this time, at some time in the past, or the potentials for the development of life at a future date. Two spacecraft, each consisting of an Orbiter System and a Lander System, are planned for launch during the 1975 opportunity. The Orbiter System is being developed by JPL; the Langley Research Center is responsible for the Lander System, which is being developed under contract by the Martin Marietta Corporation. Langley has overall management responsibility for the *Viking* Project.

The orbiter will transport and insert the lander into Mars orbit at the appropriate point for a given range of preselected landing areas. The topography of Mars will be mapped during orbital operations, with special emphasis on mapping proposed landing sites prior to deorbit of the lander and on supporting the lander after it is on the surface of Mars by determining if changes are apparent in the vicinity of the lander. After the lander has landed, the orbiter will relay telemetered data from the lander to earth. Scientific instruments on the orbiter will be used to measure atmospheric and surface parameters at various times and locations to determine the dynamic characteristics of the planet. Both visual and infrared coverage will be possible during the presently planned 140 days of orbital operations.

During entry the lander will measure Mars' upper atmospheric composition and lower atmospheric temperature, pressure, and density. After landing, surface soil analyses will be conducted by an integrated biology instrument to detect evidence of biological growth and/or metabolism and by a gas chromatograph/mass spectrometer to measure the molecular composition with particular emphasis on determining organic compounds. In addition, the landing site and surrounding areas will be mapped visually, and measurements will be made of the planet's atmospheric composition, temperature, pressure, humidity, and wind speed. Seismological, magnetic, and physical properties will be determined.

2. Status

All Action Items assigned to JPL at the *Viking* Project mission trade study review in July 1970 were completed.

Efforts are continuing in related areas of relay antenna capability, the impact of a fixed raster alignment (other than the baseline description), and in processing a configuration change on the orbiter from a 6-panel to a 4-panel arrangement.

Test activity on the gas chromatograph mass spectrometer engineering breadboard continued, after minor problems in wiring and cabling were disclosed and corrected during instrument data subsystem-instrument integration tests. Engineering model design continued, with the establishment of an instrument case configuration. Detail design and layout of components was started.

Detailed reviews were conducted covering the technical divisions' operating plans for the remainder of FY 1971 and the initiation of major hardware procurements in FY 1972. These reviews were conducted to identify required FY 1971 orbiter activities and the resources associated with their support.

B. Relay Link Multipath Simulation, *Spacecraft Communications Systems Section*

1. Introduction

The *Viking* relay link will operate at various times during the mission and provides the capability for lander-to-orbiter (uplink) and orbiter-to-lander (downlink) communications via a UHF channel. The uplink will be supported by a telemetry transmitter in the lander and a telemetry receiver/detector in the orbiter. Data will be transmitted through the uplink at 4.0 or 16.0 kilobits/s and is binary Manchester-coded frequency-shift-keyed. The recovered data stream may be recorded in the orbiter and, in the case of 4.0-kilobits/s data, relayed real-time to earth. The downlink will be supported by an amplitude-modulated transmitter in the orbiter and a receiver/tone detector in the lander. The orbiter may address a particular lander by means of a unique tone modulated on the downlink signal. The lander will respond with an uplink modulated with real-time data. When the orbiter has acquired the data stream, it initiates transmission of an enable tone. The lander then responds with playback of stored data. Playback will continue for a specified period of time and until the enable tone is lost, then ceases. A more comprehensive description of link operation and equipment may be found in SPS 37-63, Vol. I, pp. 54–61.

Previous flight projects have not used relay links, and design of this link represents a first effort in many areas. Accordingly, little experience is available on which to base predictions of performance. In order to ensure integrity of design, and to evaluate link parameters, a simulation program has been undertaken to duplicate link signals at various mission phases and measure actual equipment responses.

2. Background

The *Viking* relay link encounters degradation from signals reflected at the surface of the planet. Previous flyby programs have not had to account for these reflections because of the range between probe and planet and because of the highly directive antennas on the spacecraft. With *Viking*, the lander separates and descends through the Mars atmosphere to the surface, encountering communication ranges from zero to several thousand kilometers. Furthermore, both the orbiter and lander possess broad-beam antennas. Hence, appreciable power may be reflected from the surface with the possibility of interference with the direct signal. Such effects are termed "multipath."

During the entry and descent phases, the reflected signal has nearly random phase and rate of change of phase due to the large relative velocities and large illumination area on the surface. The doppler shift of the reflected signal may be quite different from the direct signal because of lander and orbiter motions relative to the surface. This phenomenon can cause confusion in the orbiter as to whether a received symbol is a "mark" or a "space," since mark/space identity is keyed to the signal frequency. Multipath fading during entry may be rapid with peaks and nulls occurring in an interval shorter than a single bit time. Therefore, the received signal could be fairly constant when averaged for a period of several bit times. Changes in the average received signal level may be caused mainly by geometry variations rather than by phased addition and cancellation with the reflected signal. In summation, entry multipath may be characterized by interference to individual bits on a random basis, and signal levels are likely to be determined by the geometry of the link. These effects are generally of a lesser magnitude than the effects present in the post-landed phase due to the increased length of the reflected signal path relative to the direct signal path during descent and entry.

After landing, the phase of the reflected signal is more predictable because the lander is fixed relative to the surface. This gives rise to a time-stationary spatial distribution of power which is a function of the lander antenna height and aspect angle (and hence the elevation angle of the orbiter). In the post-landed phase, the orbiter receives varying signal levels caused by phased addition and cancellation such that a typical periapsis pass may produce communication margin[1] as shown in Fig. 1. The envelope of these multipath variations is shown in Fig. 2.

The power reflected from the surface is a function of surface reflection coefficient, lander antenna pattern, and elevation angle. The spatial frequency of the variations is a function of antenna height and elevation angle. As the orbiter traverses the sky, it encounters the peaks and nulls of the spatial distribution, transforming them to a time distribution of signal strength. Computation of the reflection coefficient is done by classical methods for circularly polarized waves. The horizontal and vertical reflection coefficient components are computed and combined by means of the following equations:

$$|R_H| = \frac{\cos\theta_i - \sqrt{\epsilon_r - \sin^2\theta_i}}{\cos\theta_i + \sqrt{\epsilon_r - \sin^2\theta_i}} = \text{horizontal reflection coefficient}$$

$$|R_V| = \frac{\epsilon_r\cos\theta_i - \sqrt{\epsilon_r - \sin^2\theta_i}}{\epsilon_r\cos\theta_i + \sqrt{\epsilon_r - \sin^2\theta_i}} = \text{vertical reflection coefficient}$$

θ_i = angle of incidence

ϵ_r = relative permittivity of Mars surface

[1]Communication margin is defined in specification ID-3703101, *Viking* Orbiter System to Lander System Interface Requirement Document, par. 3.3.10, Langley Research Center, *Viking* '75 Project. It is essentially a measure of the received signal level relative to that level which produces a bit error rate of 0.003 in the detected data stream.

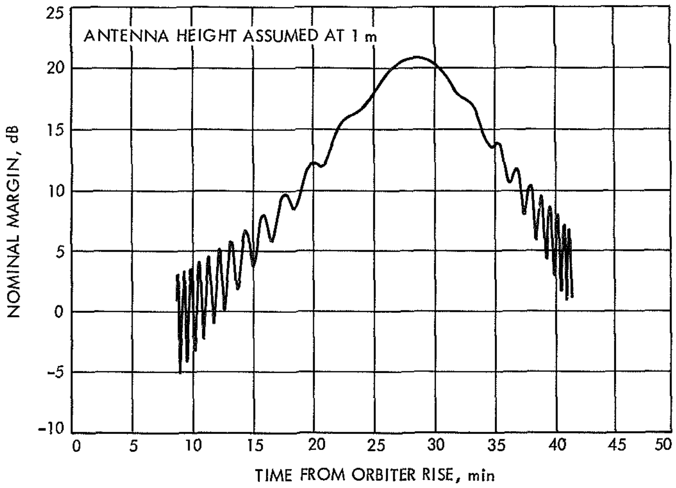

Fig. 1. Relay link performance margin versus time

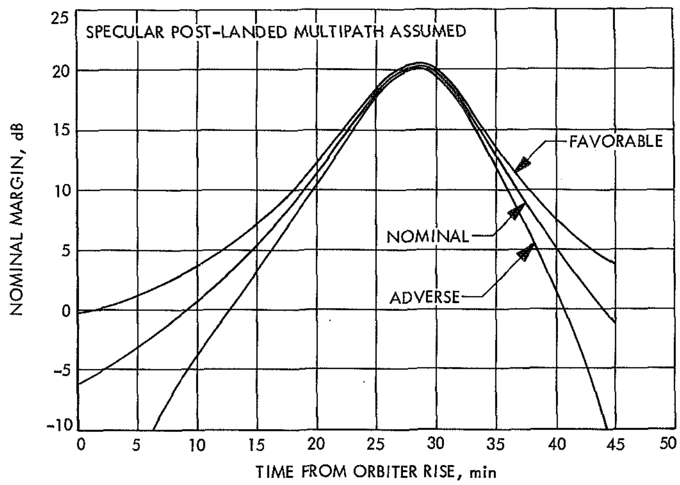

Fig. 2. Relay link performance margin versus time showing post-landed multipath envelope

$$|R_T| = \sqrt{\frac{|R_H|^2 + |R_V|^2}{2}} = \text{total reflection coefficient}$$

Assuming a relative permittivity of 3.0 for the surface of Mars (Refs. 1 and 2) the reflection coefficient can be plotted versus incidence angle as in Fig. 3.

The spatial distribution of power is computed by vectorally combining the electric fields of the direct and reflected waves with the proper amplitude and phase relationships. Assuming the free space lander antenna pattern is as shown in Fig. 4, and an antenna height of

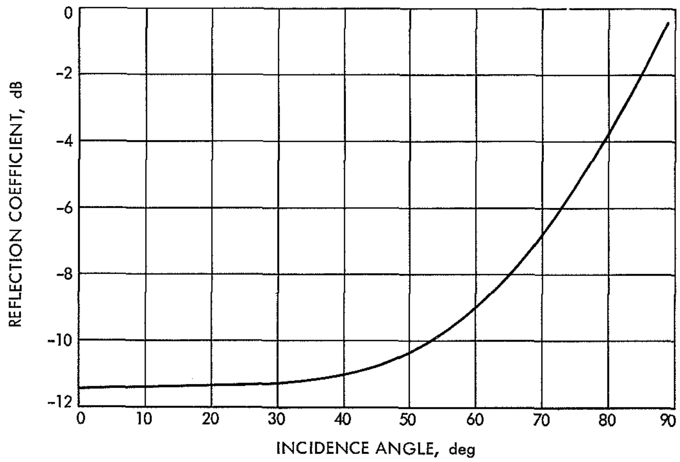

Fig. 3. Reflection coefficient $|R_T|$ as a function of incidence angle

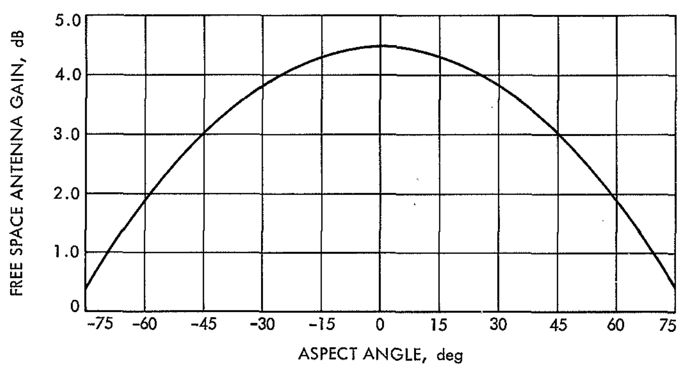

Fig. 4. Estimated lander free space antenna pattern

1 m, the spatial multipath variations (relative to the direct wave distribution) can be computed by the below equation:[2]

$$M_L = \frac{\text{received power including multipath effect}}{\text{received power without multipath effect}}$$

$$M_L = 1 + \frac{|R_T|^2 \cdot g(\pi - \theta_i)}{g(\theta_i)} - 2 \cdot |R_T| \times \sqrt{\frac{g(\pi - \theta_i)}{g(\theta_i)}} \cos\left(\frac{4\pi h}{\lambda \cos \theta_i}\right)$$

$g(\theta_i)$ = lander antenna power gain with an aspect angle of θ_i

$|R_T|$ = surface reflection coefficient at an incidence angle of θ_i

h = lander antenna height, m

λ = lander transmission wavelength, m

θ_i = incidence angle = aspect angle of lander antenna

The effective transmitting pattern (including multipath) then appears as in Fig. 5. Considering a synchronous orbit, with typical orbit parameters for *Viking*, yields the signal strength variations encountered by the orbiter as displayed in Figs. 1 and 2. The frequency of these variations is termed the "multipath lobing frequency" and is plotted versus time in Fig. 6. This figure

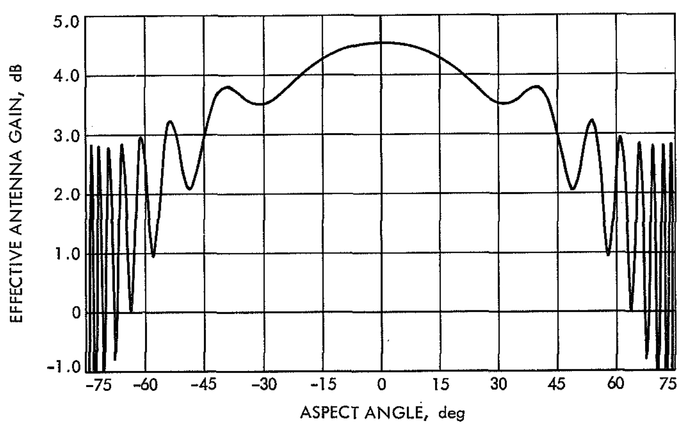

Fig. 5. Effective lander post-landed antenna pattern

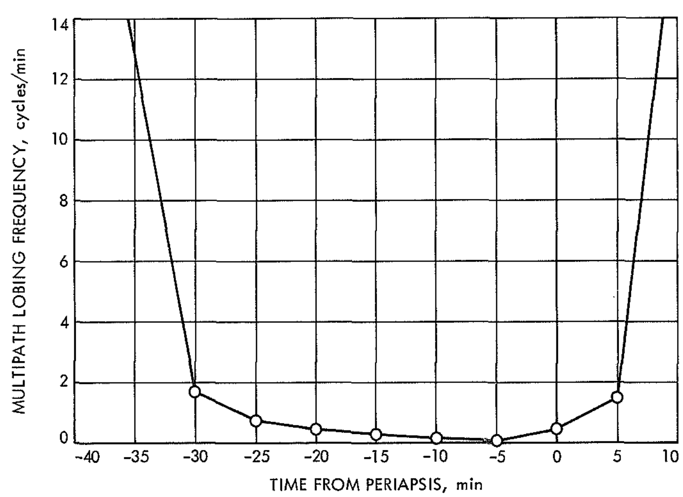

Fig. 6. Multipath lobing frequency versus time for a typical *Viking* orbit

[2]The derivation of M_L has been outlined in *Viking Relay Link Post-Landed Multipath Losses*, by G. E. Wood, Jan. 21, 1970; a correction was incorporated in the same document and issued on Feb. 4, 1970, (JPL internal publication).

essentially shows the time domain frequency of the "wiggles" in performance shown in the margin curves.

All the above presumes a specular reflecting surface on the planet. Such an assumption is valid if the surface in the local vicinity of the lander does not possess objects (rocks, rifts, rills) with rms variations greater than 1/16 wavelength from the mean surface. This means the analysis would be valid for baseball-size objects strewn randomly about the surface of the planet. Larger variations in the surface tend to smooth over the multipath effects but the envelope curves of Fig. 2 remain valid.

3. Objectives

The objectives in performing multipath simulation are threefold. Specifically the simulation effort should:

(1) Verify link performance using the multipath model described above.

(2) Provide operational norms of the functional breadboard equipment with comparisons to theoretical performance.

(3) Aid in developing a viable beacon strategy, including lock detector statistics and threshold calibrations.

4. Test Configuration

The test configuration will include equipment to simulate both the direct and reflected signals. The connection of the equipment will be as shown in Fig. 7. All equipment, other than the relay radio subsystem (RRS) and relay telemetry subsystem (RTS) breadboards, is contained within the Applied Communications Development Laboratory at JPL. All operations during testing are controlled by an XDS 930 computer. The binary data source is a pseudorandom sequence generator. Output status variables from the test are multiplexed and fed back to the computer for formatting. The detected data stream is also returned for comparison with the original data and detection of bit errors. Testing with this configuration will proceed through early 1971.

In Fig. 7 the data source modulates two FM transmitters producing the direct and reflected FSK uplink signals. Individual doppler frequency offsets can be added to the signals by combining a voltage offset to the data stream prior to modulation. Relative amplitude of the two signals can be set by multiplying the two signals independently with computer-generated functions. Finally, the signals are added together, combined with noise to establish the desired values of S/N_0, and translated to 30 MHz. This 30-MHz signal is fed directly into the IF stages of the orbiter RRS breadboard. The relative time delay of the two signal paths is established by the computer prior to modulation and can be set from 0 to 8 bit times with a resolution of 1/64 bit.

Software for test discipline via the XDS 930 computer is developed in three phases. Magnetic tapes containing trajectory parameters and link variables are prepared by the Martin-Marietta Corp. and JPL. An intermediate program at JPL converts these tapes to new tapes by abridging, scaling and formatting. The intermediate tapes are processed in the Applied Communications Development Laboratory, and a final tape is written for use with the XDS 930 computer and test fixture. Contents of the final tape are blocks of data spaced equally

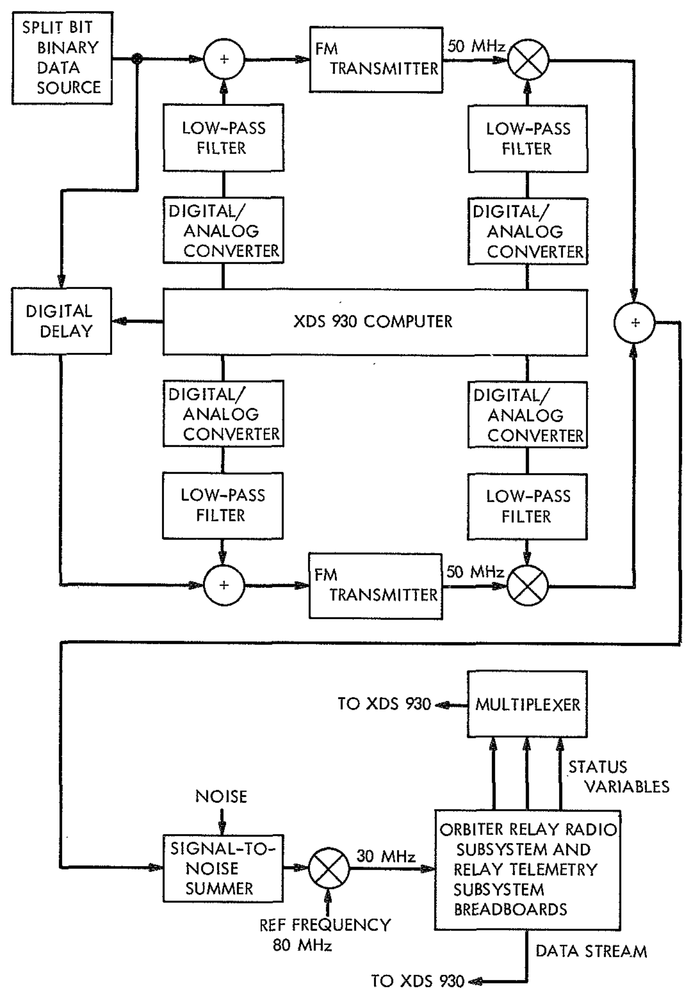

Fig. 7. Test configuration for *Viking* relay link multipath simulation with substitute lander equipment

in time. Each block contains the five parameters necessary for a link simulation point, namely:

(1) Relative strength of the direct signal.

(2) Relative strength of the reflected signal.

(3) Direct signal doppler shift.

(4) Reflected signal doppler shift.

(5) Time delay of the reflected signal.

The data blocks are spaced equally in time (generally 0.5 to 1.0 sec between blocks) and are used by the computer to construct a real-time simulated multipath environment.

References

1. NASA LRC-VPO M75-125-0, *Mars Engineering Model*, Langley Research Center, *Viking* 75 Project Office, Hampton, Va., March 13, 1970.
2. NASA SP-8020, "Mars Surface Models (1968)," *NASA Space Vehicle Design Criteria (Environment)*, May 1969.

C. Sun Occultation Logic and Sun Sensor Null Detector, *Spacecraft Control Section*

1. Introduction

During the orbit of Mars by the *Viking* orbiter the Sun will periodically be occulted. The circuit design for automatic sensing of occultation and the associated logic is presented here (see SPS 37-64, Vol. I, pp. 31–34).

2. Discussion

The *Viking* spacecraft will be put under inertial control in three axes, by either a central computer and sequencer sun occultation signal (CCSOC) or an automatic sun occultation signal (ASOC). A direct command, DC-24, will determine which signal has control. The ASOC signal is generated when there is a coincidental absence of sun gate and sun-sensor error voltage. The null detector output indicates null for offset angles less than 2 deg. A sun-gate signal is present at offset angles less than about 5 deg. CCSOC does not require the loss of sun gate to place the spacecraft under inertial control. This gives more flexibility to this command, allowing its use in possible failure modes.

When possible, the gyros are allowed to warm up before the inertial mode is initiated; however, the resultant error is minimal when there is no warm-up. There is no delay in going to inertial as a result of ASOC, whereas CCSOC inertial has a delay.

One ambiguity is that ASOC could be issued when the spacecraft is 180 deg from the normal sun orientation. This occurrence is prevented during the initial sun acquisition, by making one of the conditions for ASOC enable the receipt of the command that turns on the Canopus tracker. The Canopus tracker is turned on after sun acquisition. This, also, effectively takes care of the situation prior to shroud ejection. The probability of an erroneous ASOC signal at other times in the mission is extremely small. If it does occur, the inertial mode can be countermanded by a direct command.

Figure 1 shows the sun sensor null detector circuit. The output of this circuit is "anded" with the sun gate (null · S.G.) to form ASOC. The first amplifier serves as an absolute value amplifier through the use of steering diodes. The external roll-off capacitor provides some noise immunity. The output is 3 dB down at 1.6 Hz. The second amplifier is a level detector. The positive feedback adds hysteresis, which further reduces the possibility of chatter.

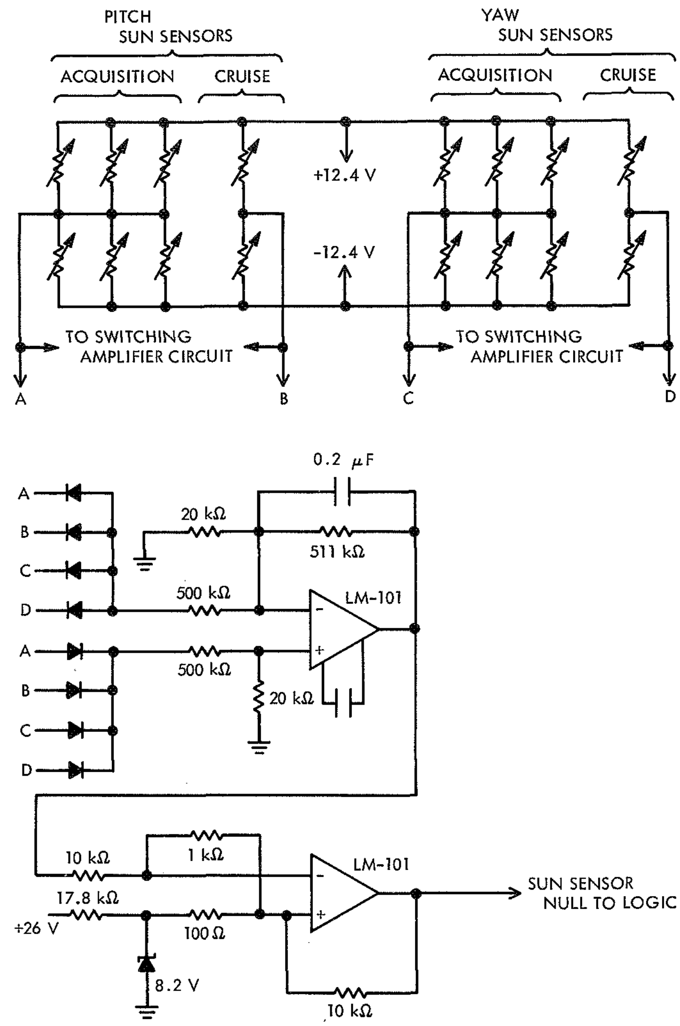

Fig. 1. Sun sensor null detector circuit

D. Articulation Control Subsystem, *Spacecraft Control Section*

1. Introduction

An articulation control subsystem has been proposed for the *Viking* spacecraft. Similar subsystems, whose prime function is the articulation of bodies on spacecraft are combined into a single subsystem. This report describes the design of a stepper motor control system that offers an excellent opportunity for a substantial hardware savings by multiplexing or time-sharing a major portion of the circuitry among the various functions in the subsystems. This is possible without any degradation of accuracy or performance. Two similar designs are being evaluated, the only difference is the error-correction technique. One employs an error-actuated constant rate mechanization, while the second corrects continuously, using a rate proportional to the error amplitude. A discussion of the systems functional elements and the results of an error analysis are contained herein.

2. Description

Figure 1 is a functional diagram of the constant-rate multiplexed stepper motor control system. It shows the analog feedback signals multiplexed into a single high-input impedance, unity gain buffer amplifier and the digital output of the up-down counter shared among the driver circuits. A serial input command, containing signal selection and output position information, is decoded. This updates the binary register and enables the appropriate multiplexer switches. Corrective action is initiated by the presence of an error at the system summing junction. If the error is greater than the threshold of the error detector, the detector will energize the clock, and depending on the polarity of the error, issue a count-up or count-down signal to the counter. Since the counter flip-flops actuate the motor drivers, the feedback signal is corrected at the rate of one step per clock pulse until the error signal is reduced to a level below the threshold of the error detector. When this occurs the error detector inhibits the clock and the system is inoperative.

Figure 2 is a diagram of the 10-bit digital-to-analog converter (D/AC) and error detector. The D/AC uses a deposited thick-film resistor network on a 1-in.^{2} substrate. The network contains a 12-bit 20-kΩ R-2R ladder and three application resistors and exhibits a maximum output voltage ratio error of ±122 ppm (±0.012%) over the temperature range of −55°C to +125°C. The use of this network virtually eliminates the ladder and summing resistors as sources of error.

The D/AC switches, which alternately switch $+V_{ref}$ or $-V_{ref}$ to the ladder network, use transistors, operated in the inverted mode. In this mode they exhibit offset voltages ≤ 0.8 mV and saturation resistances of ≤ 8 Ω. While the percentage change of these parameters with temperature is equal to a normal connected transistor, the absolute change is much smaller due to the low initial values. Since high-speed operation is not required, the errors due to these temperature associated drifts were further minimized by raising the impedance level of the ladder to $R = 20$ kΩ.

The error detector consists of two integrated circuit comparators with positive and negative thresholds set by resistor dividers. Whenever the error signal is less than the thresholds, the outputs of both comparators are at ground, driving the clock inhibit signal true. If the error exceeds these limits, corrective action is initiated.

Normally in a D/AC the reference voltages are generated from tightly regulated low-drift precision supplies. However, in this design, the feedback potentiometer will be excited by the same supplies as the ladder, causing their output voltages to track on a volt/volt basis. This allows the requirements of the reference supplies to be very loose. In fact, open-loop unregulated supplies will be used.

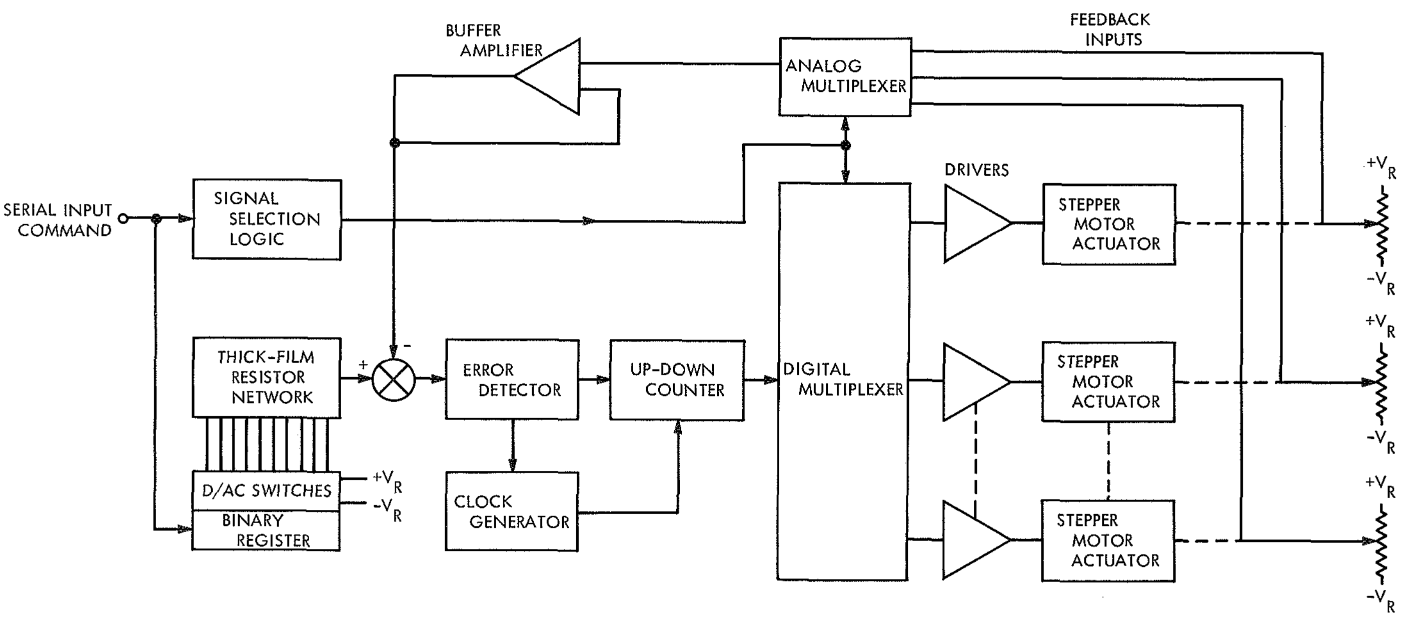

Fig. 1. Multiplexed stepper motor control system

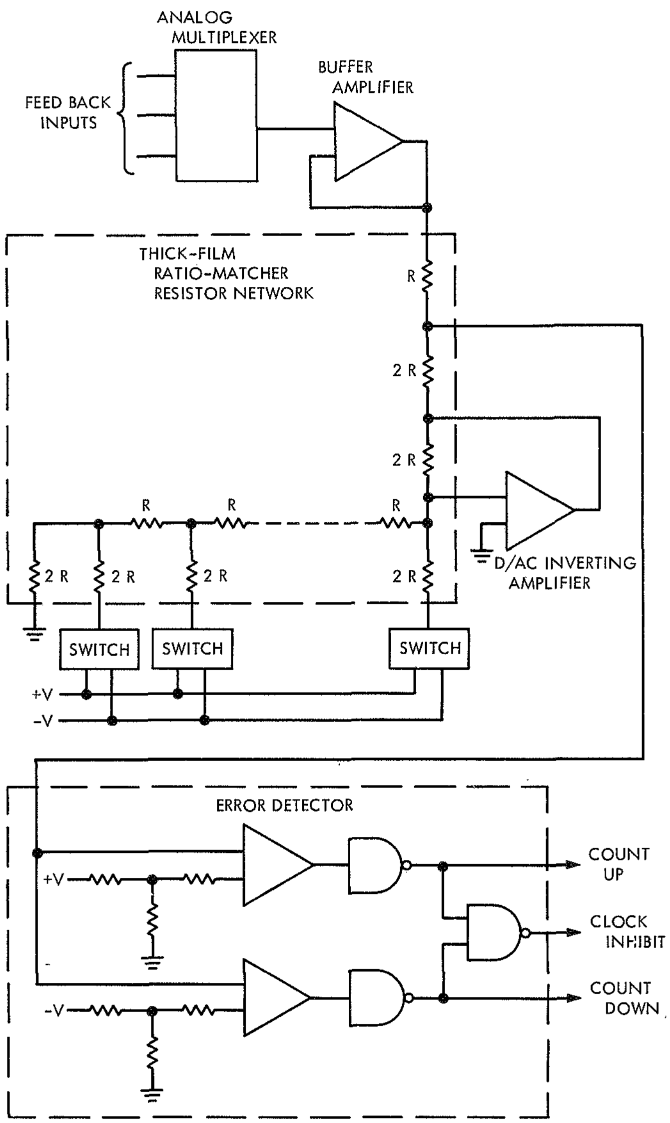

Fig. 2. 10-Bit D/AC and error detection

This equipment requires an initial adjustment, as all precision equipment does. During assembly, the threshold setting resistors will be selected to null the initial offsets with a resolution of ± 0.5 mV. This adjustment effectively reduces these errors to a negligible amount.

The logic portion of the system, which includes the 2-bit up-down counter, the 10-bit serial-to-parallel converter, and the clock generator, has not been finalized. However, the requirements for these functions are not severe, and no difficulties are anticipated.

Figure 3 is a functional diagram of the continuous error correction technique that is also being considered. It consists of an integrator, positive and negative level detectors, and a pair of reset switches. If an error current exists, the integrator output voltage will be a ramp, its direction depending on the polarity of the error current and its rate on the magnitude. When the output voltage reaches the threshold established by a resistor divider, the comparator changes state turning the reset switch (Q_1 or Q_2) on. The switch saturates, drives the noninverting input to ground and supplies reset current to the integrator summing junction. When the integrator output, which is being driven toward ground, reaches zero, the comparator again changes state, turning the reset switch off. The cycle then repeats itself. The output waveforms of Q_4 or Q_5 will be a pulse, its width equal to the reset time and its frequency dependent on

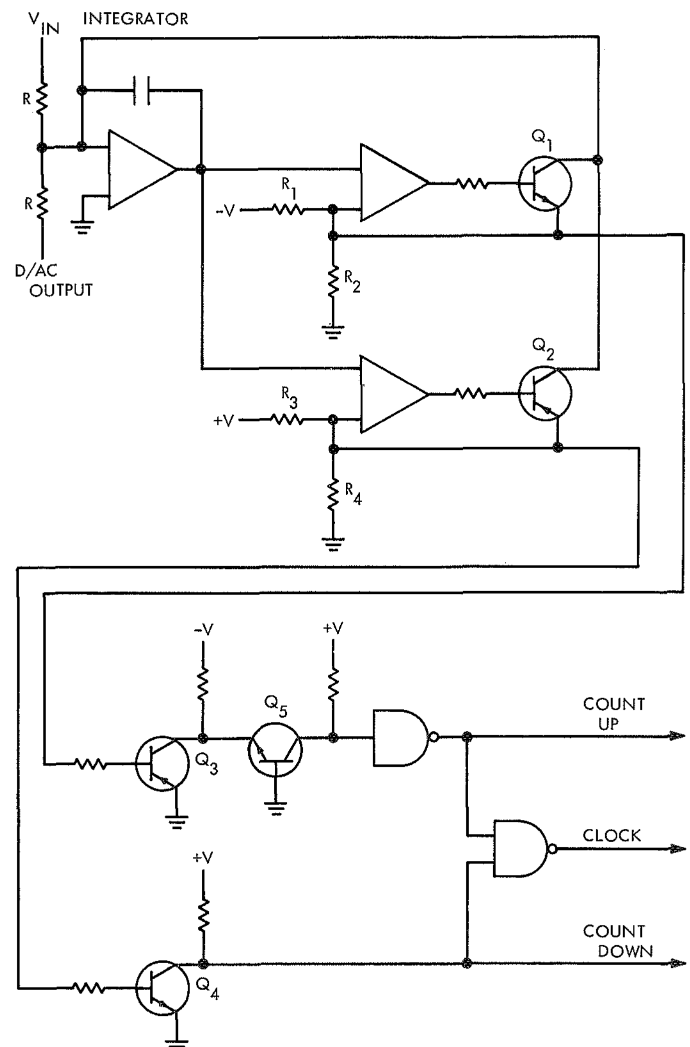

Fig. 3. Continuous error detector

the magnitude of the error signal. This signal is supplied to the counter and the motor switches and is used as a system clock. The pulse width can be varied by adjusting the impedance level of resistor combination R_1, R_2 and R_3, R_4 and thereby eliminating the need for a pulse-shaping one-shot multivibrator.

The choice between the two techniques is one of fast response, with a $\pm 0.02\%$ deadband, for the error-actuated system versus a very fine null with no deadband, but sluggish response about null for the continuous system. Both will be evaluated further.

The results of an error analysis, excluding the error contribution of the feedback potentiometer, indicates that the $\pm 3\text{-}\sigma$ error is ± 3.66 mV or $\pm 0.030\%$ full scale as compared to the worst case error of ± 6.29 mV or $\pm 0.052\%$ full scale. In the error-actuated system these numbers represent the accuracy of the null about the deadband, while for the continuous system it represents the accuracy about the command position. For either technique the accuracy is very satisfactory.

E. Separation Interfaces, *Advanced Projects Development Section*

1. Introduction

The two orbiter separation interfaces discussed in this section are the spacecraft/*Centaur* adapter and the orbiter/lander adapter interfaces. Each separation interface consists of four dual-squib release-nut mechanisms that provide the structural load path across the four interface hardpoints and four caged stroke spring assemblies that provide the separation force.

2. Release Nut Separation

The release nut mechanism (Fig. 1) consists of three threaded nut segments, separator and locking pistons, base flange, and outer casing. The three nut segments mate with a high-strength ½-20 UNF bolt allowing the assembly to be torqued to a specified preload. When the squibs are fired (Fig. 2), the separator and locking pistons are driven away from the squibs. The locking piston geometry is such that the nut segments can then be displaced radially away from the bolt by the separator piston. This reduces the preload to zero and allows the bolt to be withdrawn from the release-nut mechanism. A guide hole in the base flange that is integral with the outer casing keeps the bolt from engaging the nut segments as the bolt is withdrawn.

The structural analyses conducted to date have indicated that the required preload for each release nut at

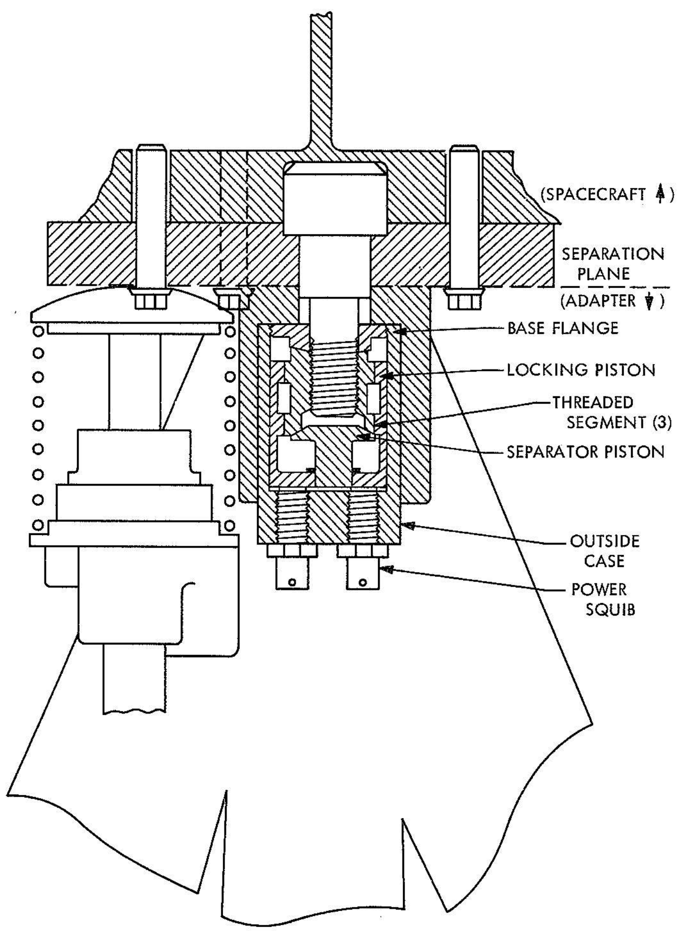

Fig. 1. Spacecraft contour adapter interface

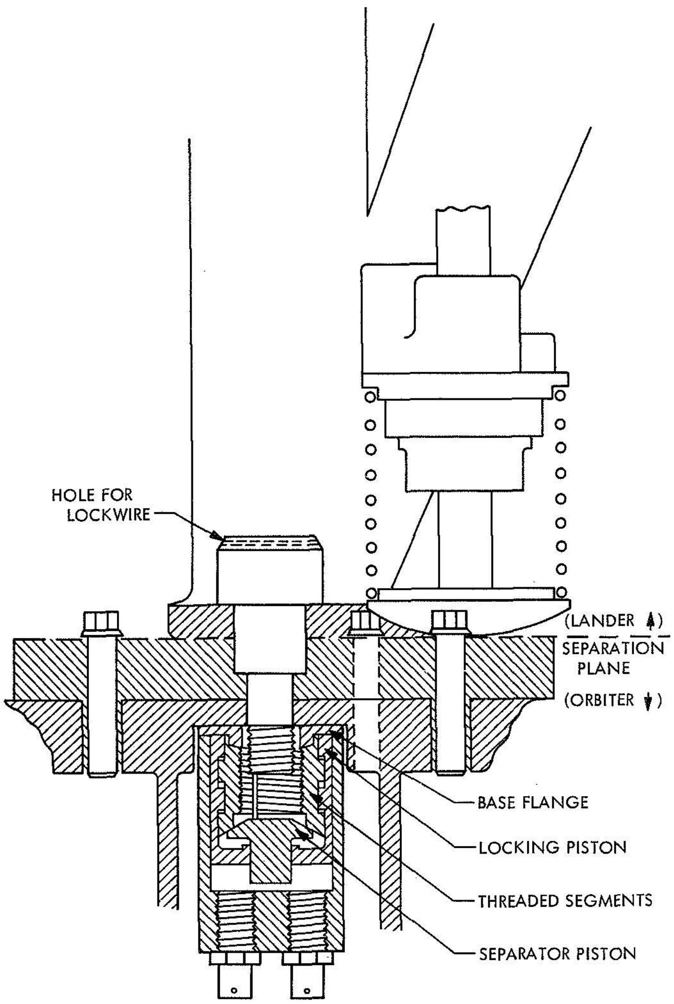

Fig. 2. Orbiter/lander adapter interface

either interface is 15,000 lb (tension/compression). Shear loads are carried by the bolt and transfer plate (as explained in *Subsections 4* and *5*) and do not directly bear on the release nut.

3. Separation Springs

Four caged stroke (preloadable) helical spring assemblies provide the separation force for either interface. The caged stroke design used on *Mariner* missions will be modified to accommodate the *Viking* preload requirements. Preloadable spring assemblies are used to reduce the relative rotation during separation between the separating bodies, caused by free spring system errors, principal axis misalignment, and tolerance errors.

The springs for the spacecraft/*Centaur* adapter interface must separate a spacecraft that is partially nestled inside the *Centaur* adapter and extends 5 ft below the separation plane. Spring sizing or separation rate for this interface is determined along with other factors by the *Centaur* residual rate, initial configuration clearance between the spacecraft and *Centaur* adapter and propellant off-loading. Preliminary dynamic separation analyses have indicated the spacecraft/*Centaur* adapter separation rate to be about 2.0 ft/sec.

The orbiter/lander adapter interface separation rate is determined by the design requirement that the spring system be capable of separating the lander and adapter (if the lander does not separate) or separating just the lander adapter. In addition, the separation rate is limited by the acceleration and force loading the lander adapter and capsule can withstand. The current separation rate ranges from 1 to 2.5 ft/sec.

4. Spacecraft/*Centaur* Interface

The release nut mechanism is integrated into the spacecraft/*Centaur* adapter interface by using a transfer plate (Fig. 2). The transfer plate allows the release nut and bolt along with the caged stroke spring assembly to be preloaded prior to mating of the spacecraft with the adapter. The transfer plate is bolted to the spacecraft bus after preloading and remains with the spacecraft when separation occurs. The release nut and spring assembly remain with the adapter after separation. With the release nut on adapter side of the interface, the squib current is supplied by the *Centaur*; thus squib current transfers across the separation interface are avoided.

5. Orbiter/Lander Interface

A similar configuration to the Fig. 1 assembly is used for the orbiter/lander adapter interface except that the release nut is on the orbiter side of the interface (Fig. 2). The mating bolt and the caged stroke spring assembly are installed on the adapter side and will remain with the adapter after separation. Actuation of the release nut at this interface is achieved by power sources aboard the orbiter. This avoids transferring squib current across the interface (from the orbiter to adapter).

F. A Programmable Formater for Engineering Telemetry, *Spacecraft Measurements Section*

1. Introduction

Previous *Mariner* spacecraft have used engineering data commutators which produced fixed data formats. These data formats were fixed in both length and content (SPS 37-55, Vol. II, p. 63). This experience has indicated a well-founded need for a random access commutator which could be controlled by a reprogrammable sequencer. This type of system could potentially maximize the bandwidth usage for different mission phases, perform diagnostics on one or more subsystems in the case of isolated failures, and program around certain types of failures in the data system itself.

There is a need for efficient usage of data space in the *Viking* mission due, in part, to the large number of different engineering measurements. To efficiently use the data link, various subsets of the total telemetry measurement list should be programmed into the format at the time they are of interest. The design which follows provides a vehicle by which this may be efficiently accomplished. This design is concerned only with a portion of the total logic used to form the engineering data format. The inputs to this logic are bit sync, word sync, coded commands (to change memory contents), mode change levels, and micro-timing used for memory operation. The output of this logic is an 8-bit digital word used to select the channel which is to be sampled for the next engineering data word. The 8-bit word defines one of 256 possible channels. These channels fall into two classes, viz, those which are analog engineering inputs and those which are digital engineering inputs. When an analog input is defined, the actions which result are a switching of the analog voltage into the analog/digital converter (A/DC) input, a 7-bit conversion to digital, a dumping of the resultant 7 bits into an output shift register, and shifting of each bit serially into the data stream. When a digital input is defined, the actions which result are: shifting of the data word into the flight data subsystem (FDS) (if required), dumping of the bits into an output shift register, and shifting of each bit serially into the data stream. In the design for *Viking*, approximately 210 of the inputs are analog and approximately 46 are digital.

2. Format Structure

The format word structure is seen in Fig. 1. For a given programmed format, 148 data sources (from the total of 256) may be seen within the structure. Words 100 and 101 are constrained to be fixed digital data sources, viz., a PN sync sequence and an index word which indicates which subcommutated words are in positions 106, 107, 126, and 127.

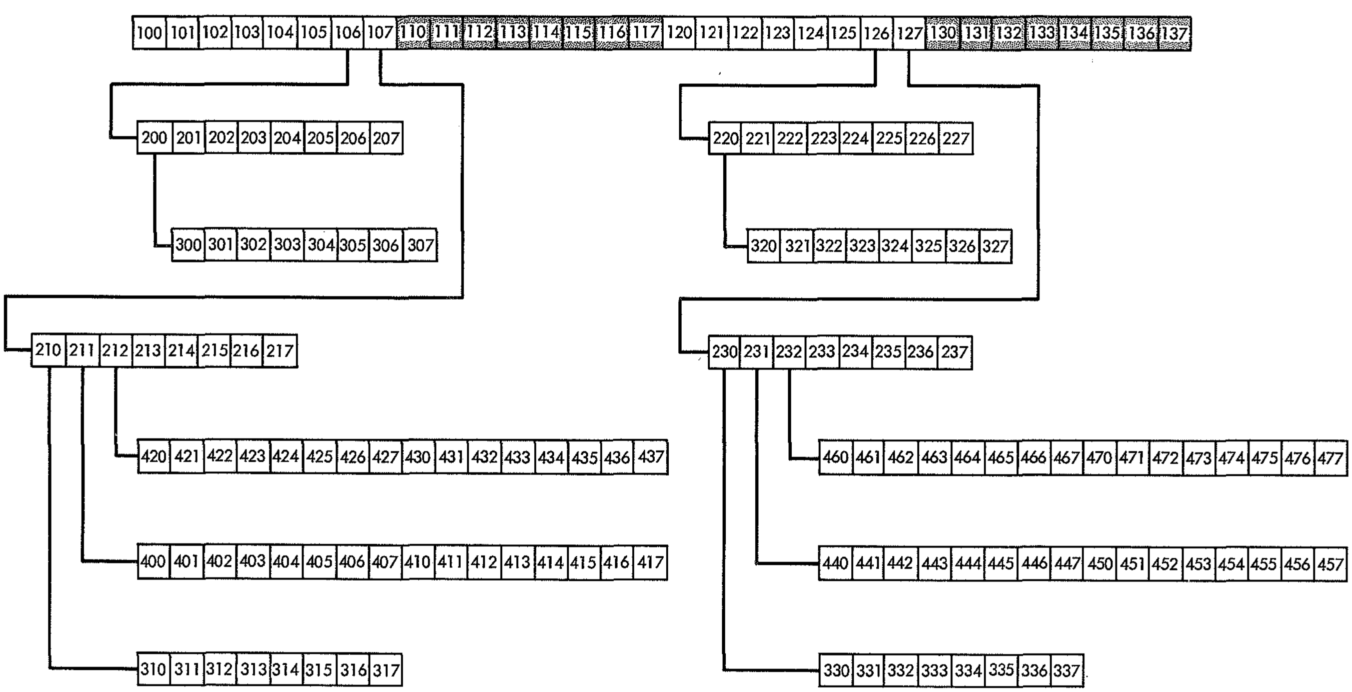

Fig. 1. Flight data subsystem engineering data format structure

A major frame (4096 words) consists of 128 minor frames (32 words). In a major frame each 400-deck position is sampled once; each 300-deck position is sampled twice; each 200-deck position is sampled 16 times; and each 100-deck position is sampled 128 times. Summarizing this in table form, over a major frame time we have:

400 deck–64 positions × 1 word/position	=	64 words
300 deck–32 positions × 2 word/position	=	64 words
200 deck–24 positions × 16 word/position	=	384 words
100 deck–28 positions × 128 word/position	=	3584 words
Total: 148 positions		4096 words

The controller for sampling within this structure is the 4096 counter (Fig. 2). A list of 148 8-bit words is stored in memory--each word representing an engineering channel for one of the 148 format positions. The 4096 counter is incremented once each format word time. The indirect address logic converts each of these counts to a memory location having a one-to-one correspondence with one of the 148 possible format positions. An 8-bit word is read out of the memory location and defines one of the 256 possible channels. The memory contents are programmed prior to launch, defining a specific subset of the 256 channels to be sampled. However, if desired, the memory may be reprogrammed via coded commands. These coded commands are entered into the memory through the "other data/memory interfaces" seen on the block diagram (Fig. 2).

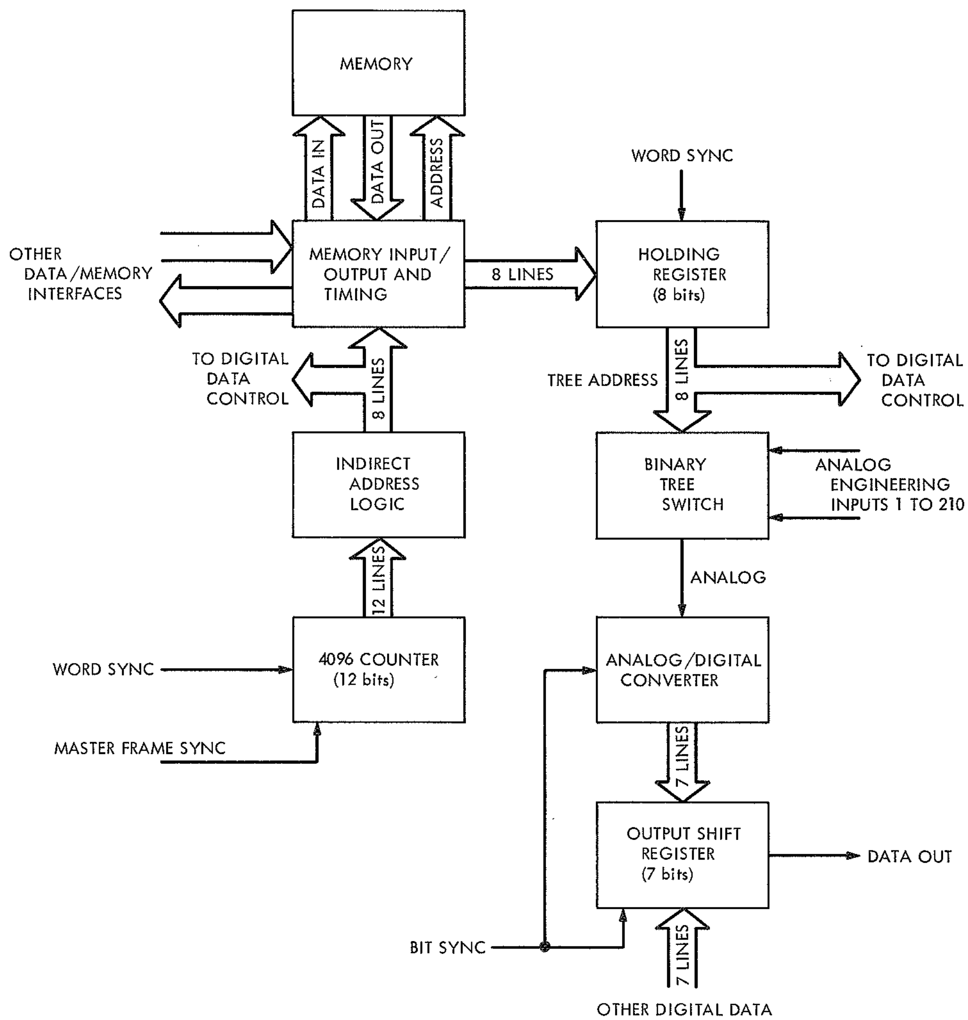

Fig. 2. Programmable format control block diagram

3. Additional System Options

Figure 3 is a block diagram of the basic system (Fig. 2) with three additional features. These are hardwired redundancy, additional memory areas, and block reprogramming.

If the "hardwired generator" (Fig. 3) output is selected by the mode control (instead of selecting the memory output), a format is generated which has the word structure in Fig. 1; however, the channel sampled at any given word in the structure is fixed. If this were used exclusively (because of memory failure), only 148 of the 256 channels would ever be sampled. A command to the FDS from the computer command subsystem (CCS) chooses either the programmable mode (memory used) or the hardwired mode.

Three additional memory areas are used in the FDS design to store three additional full-format definitions. In use the FDS have with launch, cruise, maneuver, and encounter formats stored in four separate sections of the memory. Switching from one format to another involves only a single command to the FDS. During cruise, the launch format area will be reprogrammed with a second encounter format via coded commands.

In order to facilitate diagnostics on single subsystems in the event of suspected failures, extra memory locations have been used to store the measurement channel addresses required. Utilizing a 5-bit command word (a, b, c, d, e), 8-word blocks may be called into the 110's positions or the 130's positions (shaded in Fig. 1). The

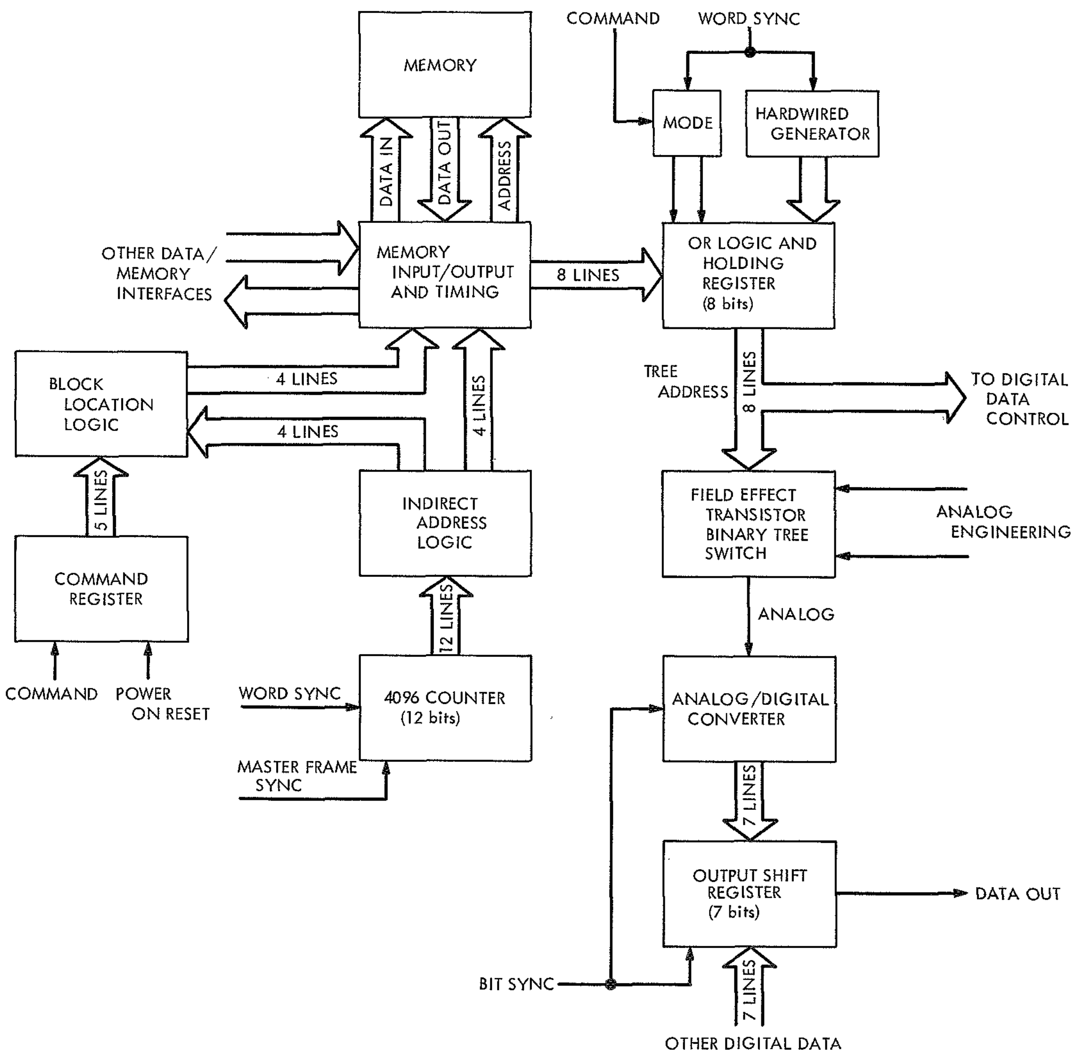

Fig. 3. Flight data subsystem engineering data format control block diagram

action resulting from any given 5-bit command is shown in Table 1. Figure 4 is a representation of word storage locations in the memory showing the extra locations used for channel addresses for subsystem diagnostics (N through Z).

4. Summary

In summary, it is seen that the full system allows three different levels of format reprogramming. The smallest reprogramming change is that of a single word in the format structure. An intermediate-size reprogramming change is that of a block of 8 words in the format structure. The largest-size reprogramming change is that of changing the complete format by moving to a different section of memory to obtain control words.

The logic for the engineering data portion of the FDS has been designed, built, and tested. The design utilized Texas Instruments 54L logic. The memory is an Electronic Memories, Inc., 8-kilobit off-the-shelf core memory. A Digital Equipment Corp. PDP-7 computer was programmed to supply coded commands to the logic through an interface rack. The computer receives the format control words and checks to see that they are correct, based on the previous coded commands which have been sent to the memory. The hardwired mode, the memory section to be used, and the 5-bit command word (a, b, c, d, e) are selectable by switches on the front panel. In the FDS these options will be controlled with coded commands. Complete checks of all logic functions have been run at room temperature and have verified the functional and logic design. In the future, checks will be run to determine the temperature and voltage margins of the hardware.

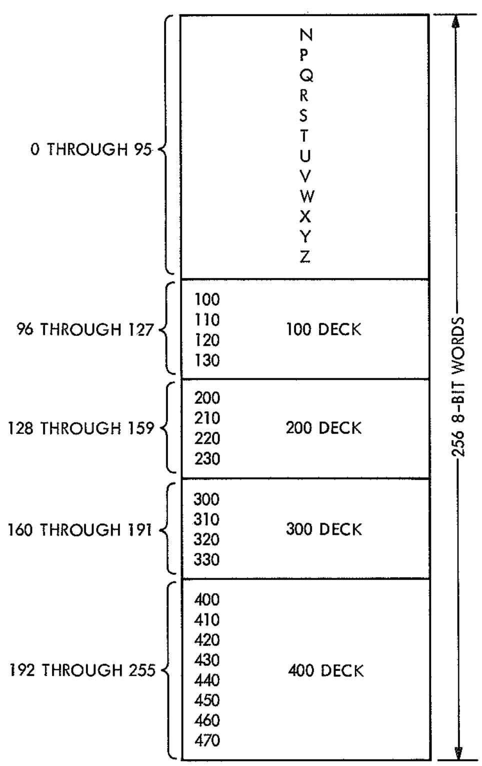

Fig. 4. Locations in segment of memory for engineering channel addresses

Table 1. Five-bit control word command sequence

Value of word in control word holding register: b	c	d	e		Substitute into 110	Substitute into 130
0	0	0	0		N	Q
0	0	0	1		P	R
0	0	1	0		S	U
0	0	1	1		T	V
0	1	0	0		W	Y
0	1	0	1		X	Z
0	1	1	0		100	120
0	1	1	1	Power-on-reset ←to this state	110	130
1	0	0	0		200	220
1	0	0	1		210	230
1	0	1	0		300	320
1	0	1	1		310	330
1	1	0	0		400	420
1	1	0	1		410	430
1	1	1	0		440	460
1	1	1	1		450	470

Control word holding register

a	b	c	d	e

If a = 0, do only second column substitution.

If a = 1, do second and third column substitutions.

When substitution is made, bits E, F, G, and J of the memory address are altered:

b is substituted for E

c is substituted for F

d is substituted for G

e is substituted for J

Bits H, K, L, and M of the memory address remain the same.

Subject Index

Subject Index

NASA — JPL — Coml., L.A., Calif.

N 71-18872

TECHNICAL REPORT STANDARD TITLE PAGE

1. Report No. 37-66, Vol. I	2. Government Accession No.	3. Recipient's Catalog No.
4. Title and Subtitle SPACE PROGRAMS SUMMARY, VOL. I FLIGHT PROJECTS		5. Report Date November 30, 1970
		6. Performing Organization Code
7. Author(s) JPL Staff		8. Performing Organization Report No.
9. Performing Organization Name and Address JET PROPULSION LABORATORY California Institute of Technology 4800 Oak Grove Drive Pasadena, California 91103		10. Work Unit No.
		11. Contract or Grant No. NAS 7-100
		13. Type of Report and Period Covered Space Programs Summary Sept. 1 to Oct. 31, 1970
12. Sponsoring Agency Name and Address NATIONAL AERONAUTICS AND SPACE ADMINISTRATION Washington, D.C. 20546		14. Sponsoring Agency Code

15. Supplementary Notes

16. Abstract

The Space Programs Summary is a multivolume, bimonthly publication that presents a review of technical information resulting from current engineering and scientific work performed, or managed, by the Jet Propulsion Laboratory for the National Aeronautics and Space Administration. The Space Programs Summary is currently composed of four volumes:

Vol. I. Flight Projects (Unclassified)
Vol. II. The Deep Space Network (Unclassified)
Vol. III. Supporting Research and Advanced Development (Unclassified)
Vol. IV. Flight Projects and Supporting Research and Advanced Development (Contents Confidential)

17. Key Words (Selected by Author(s)) Not applicable for this type of report	18. Distribution Statement Unclassified -- Unlimited

19. Security Classif. (of this report) Unclassified	20. Security Classif. (of this page) Unclassified	21. No. of Pages 58	22. Price

HOW TO FILL OUT THE TECHNICAL REPORT STANDARD TITLE PAGE

Make items 1, 4, 5, 9, 12, and 13 agree with the corresponding information on the report cover. Use all capital letters for title (item 4). Leave items 2, 6, and 14 blank. Complete the remaining items as follows:

3. Recipient's Catalog No. Reserved for use by report recipients.

7. Author(s). Include corresponding information from the report cover. In addition, list the affiliation of an author if it differs from that of the performing organization.

8. Performing Organization Report No. Insert if performing organization wishes to assign this number.

10. Work Unit No. Use the agency-wide code (for example, 923-50-10-06-72), which uniquely identifies the work unit under which the work was authorized. Non-NASA performing organizations will leave this blank.

11. Insert the number of the contract or grant under which the report was prepared.

15. Supplementary Notes. Enter information not included elsewhere but useful, such as: Prepared in cooperation with... Translation of (or by)... Presented at conference of... To be published in...

16. Abstract. Include a brief (not to exceed 200 words) factual summary of the most significant information contained in the report. If possible, the abstract of a classified report should be unclassified. If the report contains a significant bibliography or literature survey, mention it here.

17. Key Words. Insert terms or short phrases selected by the author that identify the principal subjects covered in the report, and that are sufficiently specific and precise to be used for cataloging.

18. Distribution Statement. Enter one of the authorized statements used to denote releasability to the public or a limitation on dissemination for reasons other than security of defense information. Authorized statements are "Unclassified—Unlimited," "U.S. Government and Contractors only," "U.S. Government Agencies only," and "NASA and NASA Contractors only."

19. Security Classification (of report). NOTE: Reports carrying a security classification will require additional markings giving security and downgrading information as specified by the Security Requirements Checklist and the DoD Industrial Security Manual (DoD 5220.22-M).

20. Security Classification (of this page). NOTE: Because this page may be used in preparing announcements, bibliographies, and data banks, it should be unclassified if possible. If a classification is required, indicate separately the classification of the title and the abstract by following these items with either "(U)" for unclassified, or "(C)" or "(S)" as applicable for classified items.

21. No. of Pages. Insert the number of pages.

22. Price. Insert the price set by the Clearinghouse for Federal Scientific and Technical Information or the Government Printing Office, if known.